1-1-2012

Fast Neuronal Imaging using Objective Coupled Planar Illumination Microscopy

Diwakar Turaga
Washington University in St. Louis

Recommended Citation

Turaga, Diwakar, "Fast Neuronal Imaging using Objective Coupled Planar Illumination Microscopy" (2012). *All Theses and Dissertations (ETDs)*. 652.
https://openscholarship.wustl.edu/etd/652

WASHINGTON UNIVERSITY IN ST. LOUIS

Division of Biology and Biomedical Sciences

Neurosciences

Dissertation Examination Committee:
Timothy E. Holy, Chair
Dennis L. Barbour
Bruce A. Carlson
Joseph P. Culver
Daniel Kerschensteiner
Paul H. Taghert

Fast Neuronal Imaging using Objective Coupled Planar Illumination Microscopy

by

Diwakar Turaga

A dissertation presented to the
Graduate School of Arts and Sciences
of Washington University in
partial fulfillment for the degree
of Doctor of Philosophy

May 2012

Saint Louis, Missouri

ABSTRACT OF THE DISSERTATION

Fast Neuronal Imaging using Objective Coupled Planar Illumination Microscopy

by

Diwakar Turaga

Doctor of Philosophy in Biology and Biomedical Sciences

Neurosciences

Washington University in St. Louis, 2012

Associate Professor Timothy E. Holy, Chairperson

Complex computations performed by the brain are produced by activities of neuronal populations. There is a large diversity in the functions of each individual neuron, and neuronal activities occur in the time scale of milliseconds. In order to gain a fundamental understanding of the neuronal populations, one has to measure activity of each neuron at high temporal resolution, while investigating enough neurons to encapsulate the neuronal diversity.

Traditional neurotechniques such as electrophysiology and optical imaging are constrained by the number of neurons whose activities can be simultaneously measured or the speed of measuring such activities. We have developed a novel light-sheet based technique called Objective Coupled Planar Illumination (OCPI) microscopy which is capable of measuring simultaneous activities of thousands of neurons at high speeds. In this thesis I pursue the following two aims:

- *Improve OCPI microscopy by enhancing the spatial resolution deeper in tissue.*

  Tissue inhomogeneity and refractive index mismatch at the surface of the tissue lead to optical aberrations. We have compensated for such aberrations by (1) miniaturizing the OCPI illumination optics, so as to enable more vertical imaging of the tissue, (2) correcting for the angular defocus caused by the refrac-

tion at the immersion fluid/tissue interface, and (3) applying adaptive optics to correct for higher order optical aberrations. The improvement in the depth at which one can image tissue will enable the measurement of activities of neuronal populations in cortical areas.

- *Measure the diversity in the expression pattern of VSNs responsive to sulfated steroids.*

  Nodari *et al.* have identified sulfated steroids as a novel family of ligands which activate vomeronasal sensory neurons (VSNs). Due to the experimental constraints, it has not been possible to obtain a comprehensive understanding of the number, location and functional characterstics of the sulfated steroid responsive VSNs. Applying OCPI microscopy and calcium imaging to simultaneously image thousands of VSNs, we show that the sulfated steroid responsive neurons (1) have unique ligand preferences, (2) are predominantly present in the apical regions of the VNO, and (3) that the choice of expression of a receptor type is not purely stochastic.

Acknowledgements

Funding was provided by the the G. Harold and Leila Y. Mathers Foundation, McKnight Technological Innovations in Neuroscience Award and the National Institutes of Health (NINDS/NIAAA).

I would like to thank Tim Holy for mentorship, and the Holy lab members for lively discussions and comments. I would also like to thank my parents and my brother for all their support.

Contents

List of Figures

Chapter 1

Introduction to Neuronal Imaging using Fluorescence Microscopy

The human brain is complex — complex in its organization (Fig. 1.1) and complex in its functions. The fundamental unit leading to such complexity is the *neuron*. The neuron has the ability to fire action potentials; these action potentials — when fired with specific patterns and by specific neurons — lead to the basic computations performed by the brain. To understand these basic computations one needs efficient methods to measure activities of neurons.

1.1 Methods to measure neural activity

The functioning of the brain has been partly deciphered due to our the ability to measure activities of neurons. The measurement of such activities has been possible due to the development of several different experimental techniques.

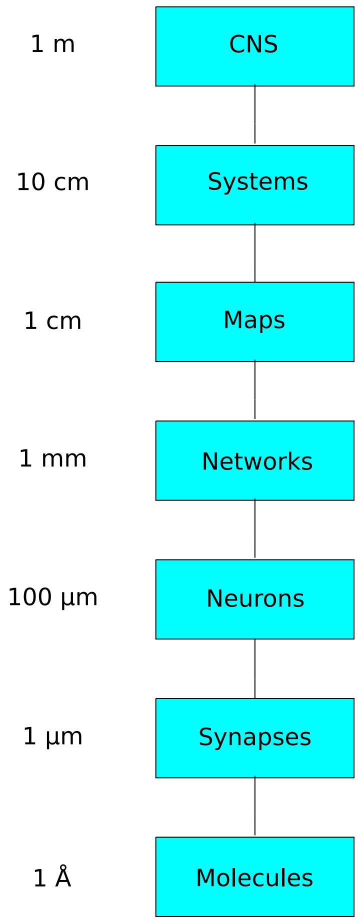

Figure 1.1: Structural levels of organization in the nervous system. The spatial scale varies widely across different levels of organization. Adapted from [1]

1.1.1 Electrophysiology

Neuronal activity is produced by the movement of charged molecules across the cellular membrane. This movement of charges can be directly measured by methods such as (1) Intracellular recording, in which an electrode gains access to the intracellular compartment and can directly measure trans-membrane voltages; (2) Extracellular recordings, which sample the much smaller changes in voltage due to currents flowing in the extracellular space but which are capable of recording action potentials; (3) Local field potentials, a variant of extracellular recording focusing on lower frequency signals and thought to represent activities of neuronal populations.

Electrophysiology at the cellular level has allowed for high resolution temporal recording of activities of individual neurons. Such single neuron recordings have led to major breakthroughs in neuroscience. For example, Hubel and Weisel used single neuron electrophysiological recordings to discover receptive fields in primary visual cortex of a cat [2].

Even so, cellular electrophysiological techniques are primarily constrained by the limited number of neurons which can be simultaneously recorded [3]. These numbers roughly depend on the number of individual electrodes used and spike sorting efficiency[1]. Typical electrodes and spike sorting algorithms allow for measuring activities from only tens of neurons simultaneously[2].

1.1.2 fMRI

Activities of large regions of cortex can be measured non-invasively using functional magnetic resonance imaging (fMRI) [5]. In fMRI, the main contrast mechanism lies in the differential blood oxygenation level during neuronal activity. When a region of

---

[1] Each electrode can record activities from multiple neurons (based on their proximity to the electrode). The challenge then is to separate activities, typically based on their waveform (assuming that different neurons have different signature waveforms). This process is called spike sorting.

[2] There are studies which employ 512 electrodes and obtain simultaneous recordings from hundreds of neurons [4], but such studies are rare.

the brain is activated there is an increase in blood flow to that region; but there is an even greater increase in the blood oxygen level. This net increase in blood oxygen level (BOLD signal) can be detected using fMRI[3]. fMRI's greatest strength lies in its non-invasiveness, allowing for experiments on humans. However, fMRI is limited by its temporal (∼1 Hz) and spatial resolutions (∼1 mm); the low resolutions do not permit cellular level analyses of neuronal circuits [6].

1.1.3 Fluorescence imaging

High temporal and spatial resolutions of neuronal activities can be obtained using fluorescence imaging [7]. Fluorescence imaging to measure neuronal activity has been possible due to two factors: (1) Fast fluorescence imaging techniques, and (2) Calcium and voltage sensitive molecules. In the next section I will expand on these two issues.

1.2 Light microscopy in neuroscience

A cubic millimeter of cerebral cortex has tens of thousands of neurons. Much has been learned about the neurons by looking at them. For example, looking at Golgi stained neural tissue, Santiago Ramoni y Cajal described intricate neural circuits. Such research by "looking at neurons" requires two major components: 1) a method to label the objects of interest, and 2) a method to image these objects. These two components have undergone dramatic improvements since the days of Cajal. A major advancement came through the implementation of fluorescence imaging.

---

[3] This is an oversimplification of the BOLD signal; please read [5] for greater detail.

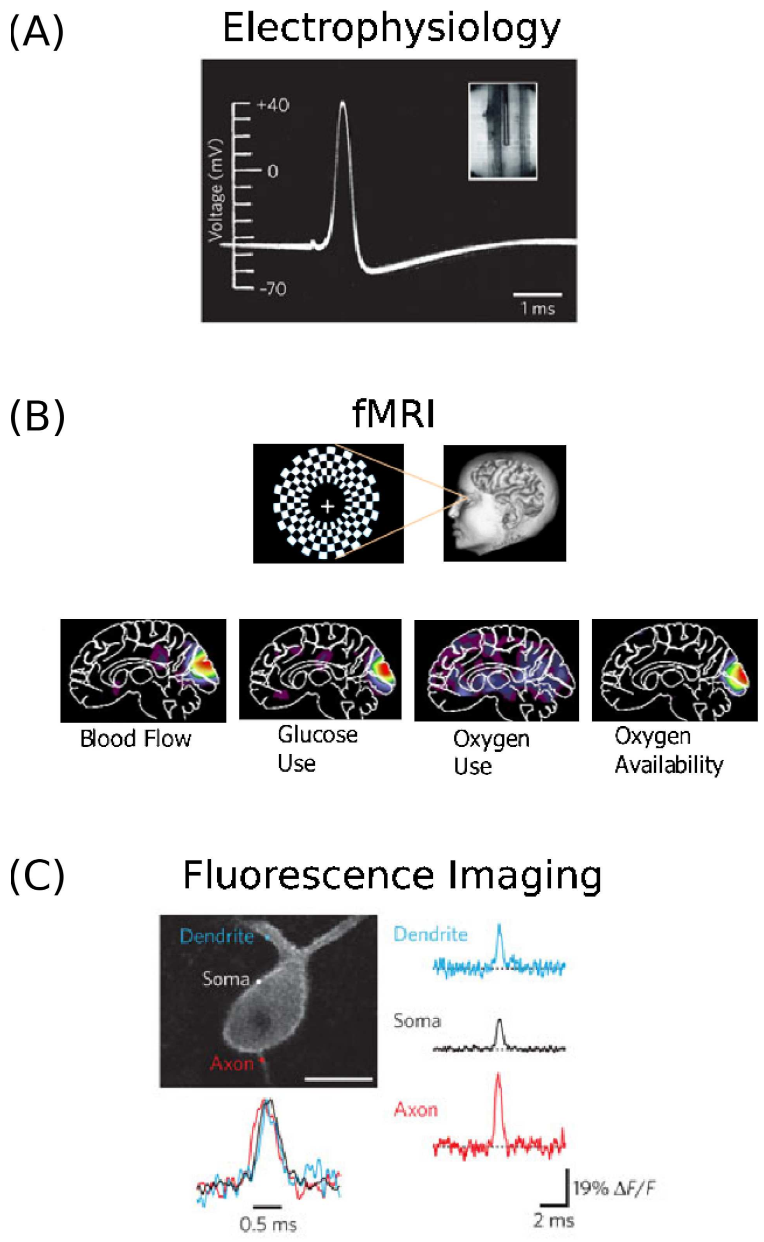

Figure 1.2: Some of the commonly used methods to study neuronal activity: **(A)** Electrophysiology (from [8]), **(B)** fMRI (from [9]), and **(C)** fluorescence imaging (from [8])

1.2.1 Fluorescence

Fluorescence is an optical phenomenon where an electron absorbs a photon of a certain wavelength and then emits another photon of a longer wavelength[4]. This excitation/emission cycle is depicted in Fig. 1.3. An electron of a fluorescent molecule absorbs light of a certain wavelength and moves to an excited (high-energy) state. This excited state is unstable and the energy has to be released. Some of the energy is lost as heat and the rest is released as another photon. This photon tends to be of lower energy (longer wavelength)[5].

Most fluorophors are conjugated hydrocarbons. These fluorescent molecules are typically attached to other compounds — such as lipids, proteins and antibodies — to allow for visualizing objects of interest. Such visualization is performed using fluorescence microscopy.

1.2.2 Fluorescence microscopy

In fluorescence microscopy light of a specific wavelength[6] is used to excite a specimen containing fluorescent molecules. Fluorescent molecules absorb this light and emit photons of a longer wavelength. The illumination light is separated from the fluorescent light using a spectral filter. The fluorescent light is collected to obtain images of the specimen. The typically used fluorescence microscopy techniques are described below:

Epifluorescence microscopy In epifluorescence microscopy both excitation and detection are from above ('epi') the sample (Fig. 1.4a). The excitation light enters through the objective and illuminates the entire field of view (FOV) of the sample; the

---

[4] This is the most common form of fluorescence. But in some cases where the photon flux is high enough, an electron can absorb two photons, and then emit a photon of wavelength roughly half of the excitation wavelength — this is called the two-photon effect.

[5] Lower energy photon has a longer wavelength. This can be seen from the following: $E = hc/\lambda$, where E is energy, h is Planck's constant, c is speed of light in vacuum, and λ is wavelength of light.

[6] The wavelength of excitation depends on the fluorescence properties of molecule of interest.

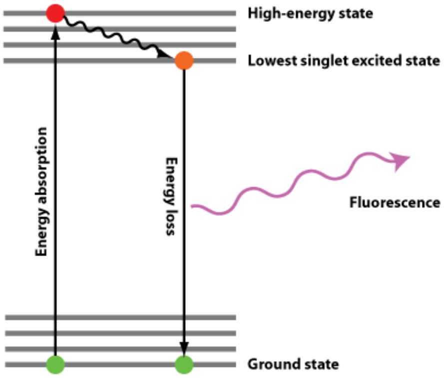

Figure 1.3: Jablonski diagram: An electron absorbs a photon of a certain wavelength and then emits another photon of longer wavelength before reaching the ground state (from www.scienceinyoureyes.com).

same objective collects the light which is given out by the sample. The light given out by the sample consists mostly of reflected light; this light is rejected using an optical filter of the appropriate wavelength. The photons produced through fluorescence are not filtered[7] and can be imaged onto a camera.

Epifluorescence microscopy is limited by the thickness of the sample that can be imaged. In thick samples both the in-focus and out-of-focus regions of the sample are illuminated, leading to low contrast images. This low contrast imaging has been traditionally overcome by physically sectioning the sample into thin slices, such that all of the slice is in-focus[8]. But if all of the sample is not in-focus, optical sectioning methods such as confocal, multi-photon and light-sheet microscopic techniques can be used to obtain high contrast images.

Confocal microscopy Confocal microscopy allows for elimination of out-of-focus light using a confocal pinhole. A confocal pinhole is a pinhole located at a point conjugated with the illumination point[9]. Only the photons originating from the in-focus regions of the sample pass through the pinhole; the photons originating from out-of-focus regions of the sample are rejected. This rejection of out-of-focus rays allows for high contrast imaging of the spot (see Fig. 1.4b) [10]. The illumination point can be scanned across the sample to allow for two-dimensional (2D) and three-dimensional (3D) imaging. This "optically sectioning" technique allows for imaging as much as $\sim$100 μm deep into tissue before scattering [10] reduces the contrast.

---

[7] These photons have a longer wavelength, and thus are not filtered.

[8] The thickness of the slice should ideally be equal to the depth of focus of the objective.

[9] Rays from the illumination point enter an objective and are typically infinity focused. One can converge the rays back to a diffraction-limited point using another lens. This new point of focus is then said to be "conjugated" with the illumination point.

[10] Scattering is a stochastic process where a photon undergoes changes in direction as it passes through regions of refractive index inhomogeneity. See [11] for a detailed review of the effect of scattering on imaging biological tissues.

Two-photon microscopy The "two-photon effect" occurs when an electron absorbs two photons and emits a single photon; the emitted photon's wavelength is roughly half of the excitation's wavelength. The two-photon effect occurs only at high photon flux, thus is typically restricted to the illumination point. The use of the two-photon effect in microscopy was first demonstrated by Denk and colleagues [12]. They combined the idea of the two-photon effect with a laser scanner to produce the first two-photon microscope. The two-photon microscope traditionally uses a femtosecond laser[11] to illuminate the sample; the wavelength of illumination is typically in the infra-red (IR) region of the optical spectrum.

The two-photon effect allows for inherent optical sectioning; only regions in-focus have enough photon density to allow for the two-photon excitation. Thus all the emitted fluorescent photons can be collected[12]. The second advantage of two-photon microscopy is that it uses IR wavelength excitation. IR excitation has inherently lower scattering than visible light, thus allowing for deeper penetration into the tissue [11]. The two advantages of two-photon microscopy permits high contrast imaging as deep as 500μm into neuronal tissue — allowing for imaging as deep as layers 5 in a mouse cortex [13].

1.2.3 Fluorescent Probes for Neuroscience

Green Fluorescent Protein A major milestone in neuronal labeling was the discovery of Green Fluorescent Protein (GFP). GFP, as the name suggests, is a protein

---

[11] The two photon effect requires a high photon flux. Such high photon flux is not obtainable using continuous wave (CW) laser due to the large power requirements. A femtosecond laser, as used in two-photon microscopes, produces brief pulses (∼100 femtosecond) of high photon intensity at ∼100 MHz repetition rates. Such a laser requires overall lower power than CW lasers, but produces bursts of high enough power to produce two-photon effect in the sample. Ti:Saphire laser is used popularly in two-photon microscopy.

[12] This turns out to be a very important factor in imaging. In typical single photon imaging, the location of the emitted light has to be accurately measured to allow for high resolution imaging. But under two-photon imaging, even if the photon appears to be coming from a different section of the tissue (possibly due to aberrations present in the system), we are certain about the location of the illumination point. Thus all the photons can be collected without the need for any imaging optics.

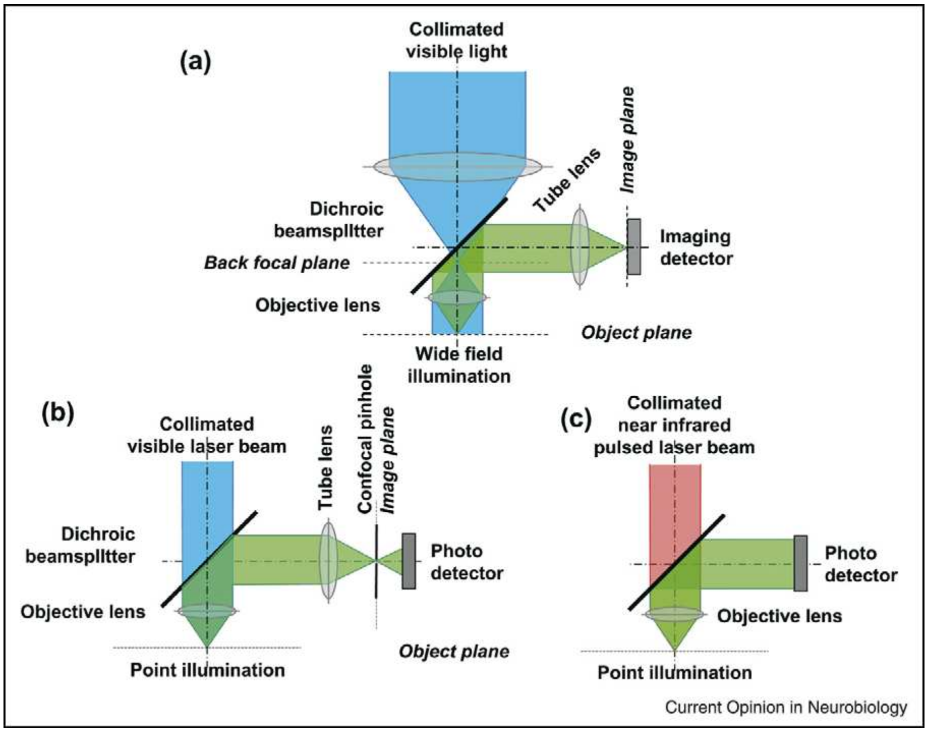

Figure 1.4: Optical layout of traditional fluorescence microscopic techniques: **(a)** Epifluorescence microscopy, **(b)** confocal microscopy, and **(c)** multi-photon microscopy (from [14]).

molecule which can undergo fluorescence. This fluorescence occurs when you shine 488 nm[13] light at the protein, leading to emission at 520-530 nm. These longer wavelength photons can be detected (using fluorescence microscopy techniques) allowing for precise localization of the GFP molecule[14]. The GFP molecule allows for the use of molecular biology techniques to selectively tag proteins of interest and watch them. Watching the proteins has subsequently become prettier when chemists produced different colored fluorescent proteins. The huge assortment of colors of the fluorescent proteins is shown in Fig. 1.5.

Calcium sensitive molecules A subsequent major advance came through the introduction of calcium sensitive molecules. Calcium sensitive molecules were first introduced by Roger Tsien and colleagues. They designed a molecule called BAPTA (1,2-bis(o-aminophenoxy)ethane-N,N,N',N'-tetraacetic acid) which undergoes a structural change upon binding to calcium [15]. This property of calcium induced structural change was combined with synthetic fluorescent dyes to produce molecules which undergo changes in fluorescence upon binding to calcium. The production of such calcium sensitive dyes (Oregon Green BAPTA, Calcium Green, etc) has allowed for imaging activity of neurons (Fig. 1.6a). These organic indicators are however contrained by the lack of neuronal specificity due to their non-specific loading procedure[15]

Recently, a calmodulin domain (a calcium sensitive protein) was attached to GFP and circularly permuted to produce a novel calcium sensitive fluorescent protein called GCaMP [16] (Fig. 1.6). GCaMP can be attached to specific proteins — allowing for expression of the fluorescent calcium sensor in only the neurons of interest. Currently GCaMP2, a second generation GCaMP, is popular in studies of activity of neuronal populations [17].

---

[13] 488 nm is the typical laser line used to excite GFP. But the excitation spectrum is broader.

[14] Within the resolution limit of the microscope. The resolution of a microscope depends primarily on the numerical aperture (NA) of the objective and the wavelength of light.

[15] The dyes are typically bulk loaded, leading to all the cells surrounding the injection site taking up the dye.

Green Fluorescent Protein

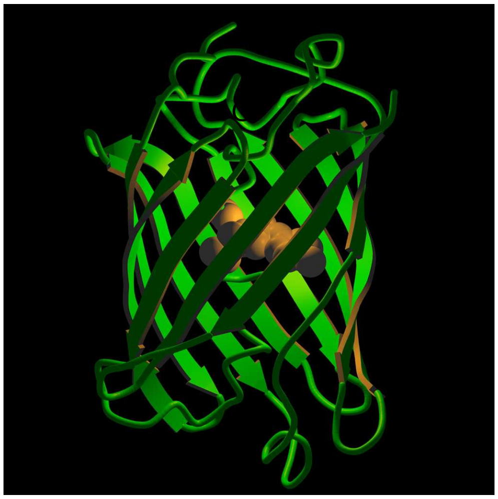

Agar Plate of Fluorescent Bacteria Colonies

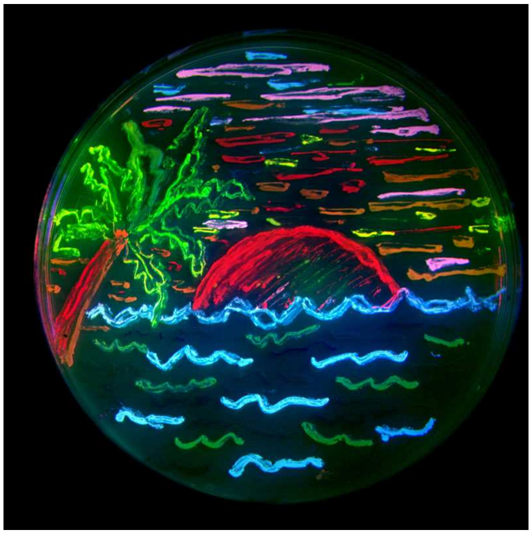

Figure 1.5: **(top)** Structure of GFP. **(bottom)** Various available fluorescent proteins plated on an agar plate. (from http://www.tsienlab.ucsd.edu/Images.htm)

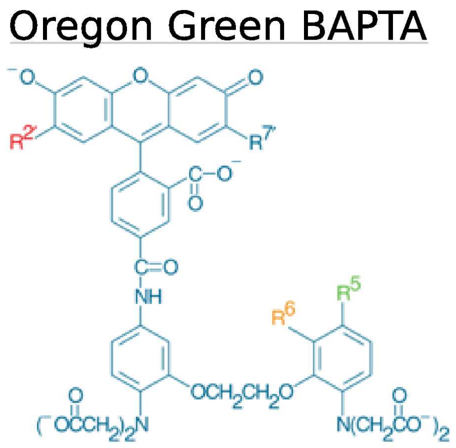

Indicator	$K_d(Ca^{2+})$	$R^{2'}$	$R^{7'}$	R^5	R^6
Calcium Green-1	0.19 µM	Cl	Cl	H	H
Calcium Green-5N	14 µM	Cl	Cl	NO_2	H
Oregon Green 488 BAPTA-1	0.17 µM	F	F	H	H
Oregon Green 488 BAPTA-6F	3 µM	F	F	H	F
Oregon Green 488 BAPTA-5N	20 µM	F	F	NO_2	H

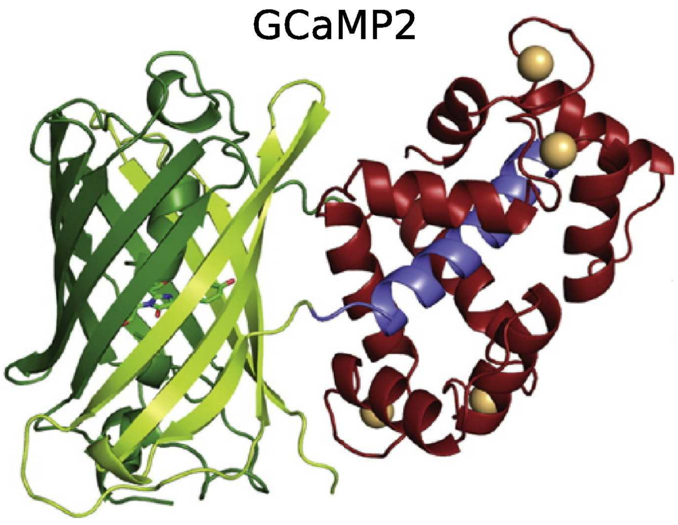

Figure 1.6: Commonly used calcium indicators: **(top)** Organic indicators, of which Oregon Green BAPTA-1 is the most commonly used indicator (from http://www.invitrogen.com). **(bottom)** Calcium sensitive fluorescent protein GCaMP2: crystal structure (from [18]).

1.2.4 Imaging fast calcium signals

Fundamental limitation on speed of fluorescence imaging In a typical optical imaging system, greater signal-to-noise ratio (SNR) can be achieved by collecting more photons. In fluorescence microscopy, more photons, to a certain extent, can be produced by simply illuminating the sample with higher excitation power. But at high enough excitation power, all the electrons in a fluorophore are saturated; increasing the laser power will not help in increasing number of excited electrons. The excited electrons emit photons to reach the ground state. The time required for the cycling between excited/emitted state of an electron — at high excitation power — turns out to be the ultimate rate limiting step in fluorescence imaging (Fig. 1.3) [19, 20]. This rate limiting step is in the order of nanoseconds per electron — a seemingly small number. But this small number has to be combined with the experimental considerations such as SNR required, amount of dye labeling, photon collection efficiency — leading to an estimate of pixel dwell time of 1 μsec[16] to achieve adequate SNR imaging.

High speed imaging techniques Calcium imaging in thick neuronal tissues is currently performed using laser scanning microscopes (LSM). LSM, such as two-photon microscopes and confocal microscopes, typically image one pixel at a time, leading to the $\sim$1 μsec per pixel limitation on their speed. This speed permits imaging a 1 Mpixel image in 1 sec, and a 60 slice volume in 1 minute — which is slow for measuring neuronal activity at cellular level. Higher frame rates have been achieved using LSM by imaging smaller number of pixels [21–25].

One can compensate for the $\sim$1 μsec per pixel limitation by imaging multiple

---

[16] Pixel dwell time is the amount of time spent collecting photons for a single pixel. $\sim$1 μsec per pixel is the minimum pixel dwell time for a SNR of 100. One can go much faster, but at the cost of obtaining noisier images. In quantitative imaging, such as calcium imaging, one requires high SNR images. See supplementary information in [20] for quantitative explanation of the fundamental speed limitation of fluorescence imaging.

pixels simultaneously. For example, in two-photon microscopy, multiple simultaneous imaging spots have been achieved using beam splitting or beam shaping optics [26–29]. Multiple simultaneous imaging spots when combined with fast imaging (using CCD or CMOS cameras) has indeed led to imaging at faster pixel rates. But these faster pixel rates come with the price of needing higher laser powers and obtaining images with lower contrast[17].

1.3 Scope of the thesis

Light sheet microscopy allows for another form of parallelization of pixel acquisition and allows for high speed imaging of neurons at high SNR over large fields of view. In this thesis I will describe an implementation of light sheet microscopy — called OCPI microscopy — to image the activities of large populations of neurons at high speed, using the vomeronasal organ (social odor detecting epithelium) as the experimental system.

---

[17] The lower contrast comes about due to the use of a camera as the photon detector. In a typical point scanning two-photon microscopy, all the photons are known to be emitted from the same point. Thus all the photons can be collected. But in multi-focal multi-photon microscopy, one loses this advantage. One needs to image the photons onto the CCD, thus leading to some ambiguity in exact emission position due to scattering/aberration effects. This in effect leads to lower SNR imaging in such multiplexed imaging systems.

Chapter 2

Light Sheet based Fluorescence Microscopy

2.1 Basics of Light Sheet based Fluorescence Microscopy

The idea of using a light sheet to illuminate samples dates back to Siedentopf and Zsigmondy in 1903 [30]. The idea has been rediscovered by multiple research groups independently during the last few years [20,31–35] (see [36] for an exhaustive review).

Typical microscopes are uniaxial – i.e. the excitation axis and emission axis go through the same objective [19]. Light sheet fluorescence microscope (LSFM[1]) separates the excitation axis from the detection axis. In LSFM, the excitation typically comes through a low numerical aperture[2] (NA) cylindrical lens which converts a collimated beam[3] into a sheet of light. The light sheet is placed at the focal plane of

---

[1] Not to be confused with LSM, which stands for laser scanning microscope: confocal or two-photon microscope.

[2] Numerical Aperture (NA) is an essential property of an optical lens. It is a measure of the amount of light that can be collected by a lens from a single point source. NA $= nSin\theta$ where n is the refractive index of the immersion medium ($n = 1$ in air and $n = 1.33$ in water) and θ is the half-angle of the maximum cone of light that can enter the lens.

[3] A collimated beam is another way of describing a beam in which all the rays are travelling in

objective lens. The tissue sample is then positioned in this overlapping volume. Such an arrangement allows for inherent optical sectioning by illuminating only the region of the sample which is in-focus (Fig. 2.1).

The variations in the implementation of LSFM depends on the size of the sample being imaged. While imaging small samples (ex. zebrafish embryo) one can place the entire sample in-between the cylindrical lens and the objective. This allows for an arrangement where the entire optical axis is parallel to the optical table (Fig. 2.2B,E); 3D images of the sample are obtained by rotating the small sample on a rotatable mount. When the samples are bigger (eg. mouse cortex) but the tissue is transparent, one can convert an upright microscope into a LSFM (Fig. 2.2D) by illuminating the sample from the side. But in the case where the sample is large and not transparent (typical in live neuronal tissue imaging), one can couple the light sheet to the objective and tilt the entire setup by 45 degrees (Fig. 2.2C and Fig. 2.3); this tilted arrangement minimizes the extent scattering and aberrations effect the light sheet and emitted light. The objective can then be placed on a piezo-electric positioner, such that by moving the objective one can achieve fast 3D scanning of the sample. We call this optical setup Objective-Coupled Planar Illumination (OCPI) microscopy.

2.2 Light sheet characterstics

Understanding the limitation on light sheet thickness The light sheet is typically made by passing collimated light through a cylindrical lens. In the first generation OCPI microscope [20] light is carried via a fiber optic and collimated using an aspheric lens. This collimated gaussian beam[4] is then passed through a cylindrical lens. The specifications of the optical elements (NA of the aspheric lens

---

the same direction.

[4] A gaussian beam, as the name suggests, has intensity profile which is gaussian. The intensity is given by $I = I_0(z) \cdot e^{-2r^2/w(z)^2}$, where I, I_0 = intensity (W/m^2); r = radial coordinate (m); $w(z)$ = spot size (m); w_0 = beam waist (m) or spot size at $z = 0$; z = longitudinal coordinate (m).

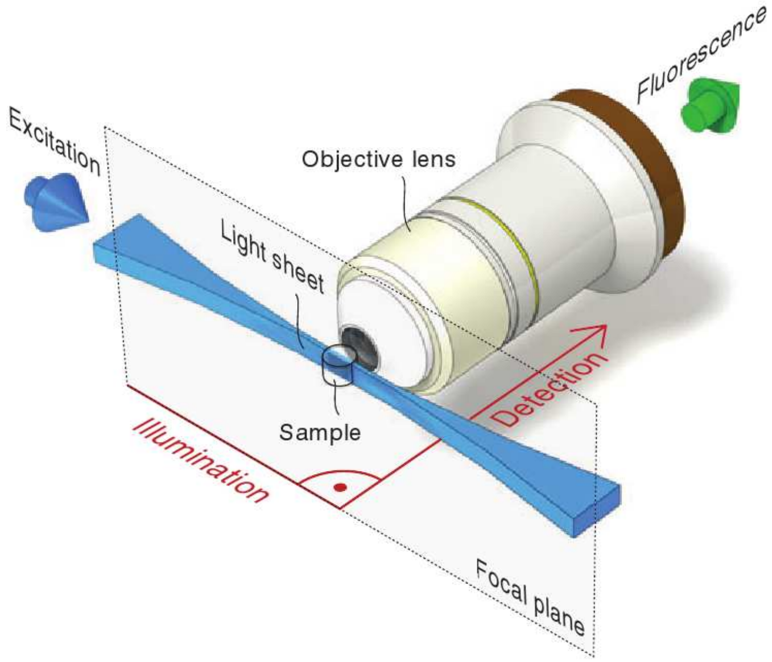

Figure 2.1: Basic Light Sheet Fluorescence Microscope (LSFM) setup. A collimated light beam passes through a cylindrical lens to form a light sheet. This light sheet is place at the focal plane of the objective (from [36]).

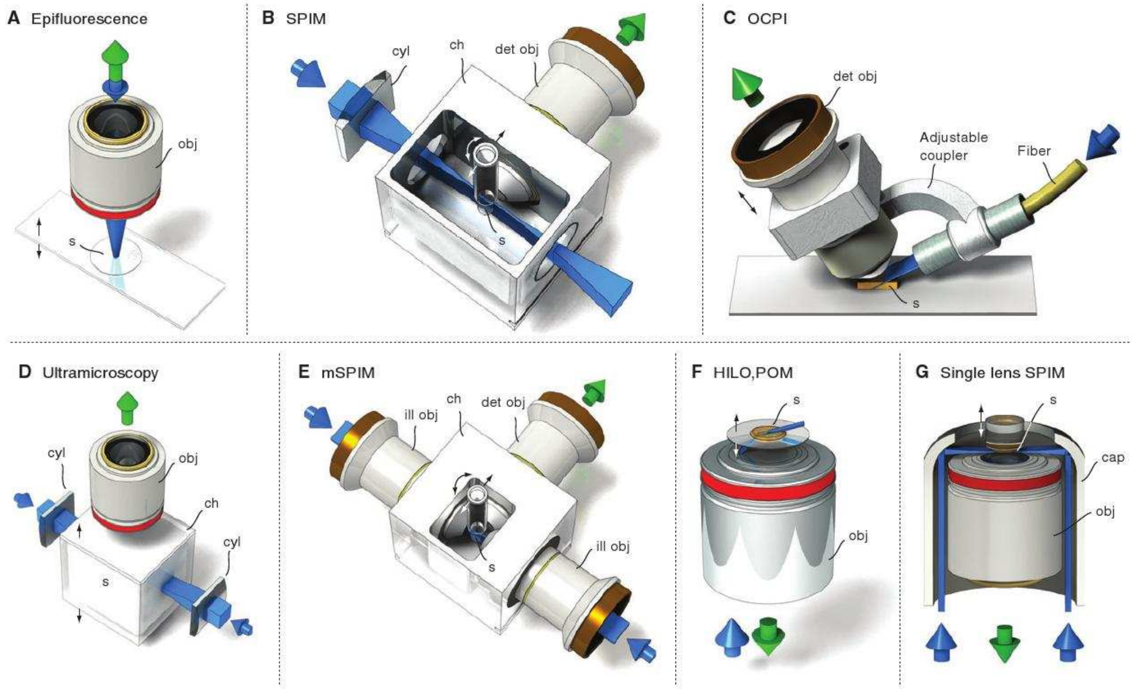

Figure 2.2: Various existing LSFM optical layouts. The differences in the layouts depends on the needs of biological system being investigated (from [36]).

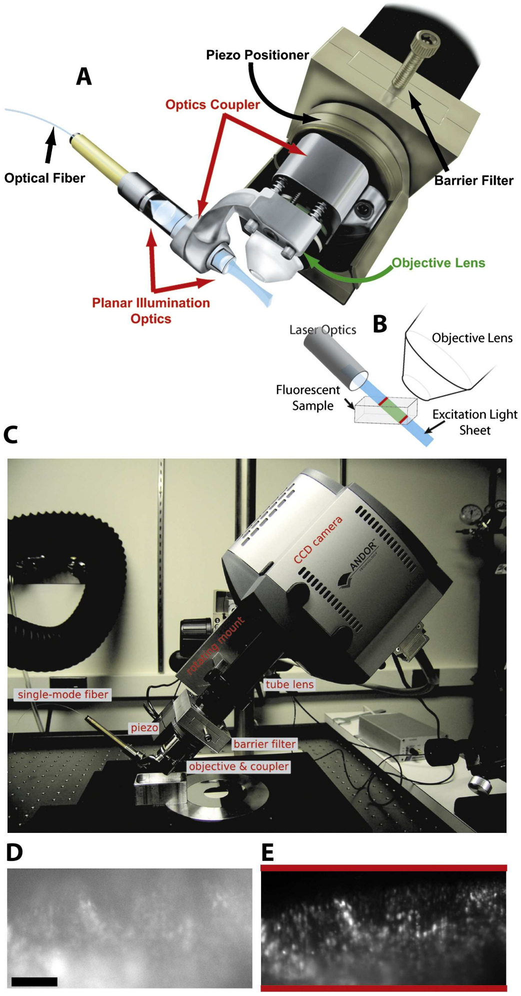

Figure 2.3: Objective-Coupled Planar Illumination Microscopy. **(A)** OCPI microscope schematic. Excitation light from a laser arrives via optical fiber and is shaped by two lenses into a thin sheet of light (≈3–5 μm thick in the objective field). Sectioning is accomplished by aligning this light sheet with the objective focal plane, preventing fluorescence excitation in out-of-focus regions. Illumination optics are coupled to the objective lens, maintaining alignment with the objective focal plane during z-axis scanning with a piezoelectric positioner. Objective lens and illumination optics are designed for water immersion. Boom arm and rotating mounting adapter allow the orientation of the microscope to be adapted to the needs of the preparation. **(B)** Schematic showing the orientation of tissue, objective, and illumination optics. **(C)** Labeled photograph of the complete OCPI microscope. **(D)** A single image frame of fluorescently-labeled mouse vomeronasal sensory epithelium (see text and Experimental Procedures for animal preparation) using conventional wide-field fluorescence illumination shows significant out-of-focus fluorescence signal, which obscures visualization of individual neurons. **(E)** The same optical field shown in (D) using objective-coupled planar illumination reveals individual neurons and demonstrates the optical sectioning capabilities of OCPI. Scale bars, 100 μm. From [20].

and the cylindrical lens) depend on the required beam waist (or alternatively to the field of view of interest).

A simplified derivation of the ideal beam waist for a required field of view is given below: The beam waist is dependent on two factors (1) the geometric convergence/divergence of light, and (2) diffraction. The geometric term can be given as $l \tan\theta$ where l is the displacement from the center and θ is the angle of divergence[5] (Fig. 2.4). The diffraction term is bounded by beam waist w by $w \sim \lambda/\mathrm{NA}$, where λ is the wavelength of light and NA is the numerical aperture of the illumination lens[6]. The total beam waist is the sum of the geometric and diffraction contributions giving beam height h being $h = l \tan\theta + \lambda/\mathrm{NA}$. The height h is thus a function of NA, field of view l and wavelength of light λ. Optimum beam height throughout the FOV can be obtained by minimizing h with respect NA. This results in $\mathrm{NA} \approx \sqrt{\lambda/l}$. Thus for a given field of view, there is an optimum NA lens that needs to be used to provide ideal light sheet thickness throughout the FOV. Substituting NA into equation for beam height results in $h \approx \sqrt{l\lambda}$ [7].

For imaging VNO, we implemented a system which can image a FOV of ~500 μm, which necessitated a sheet of ~4-10 μm. A thinner sheet of light can be produced by using a higher NA cylindrical lens — but this will be obtained at the cost of a smaller FOV where the light sheet is optimumly thin.

Resolution of a LSFM The resolution of a given microscope can be described in terms of its lateral and axial resolutions. The lateral resolution of LSFM is the same as of epifluorescence microscopes — dependent solely on the NA of the objective and wavelength of light [19]. The axial resolution of a LSFM is dependent on the

---

[5] Angle of divergence (θ) is directly related to the NA of the lens, $\mathrm{NA} = nSin\theta$

[6] The effect of diffraction can be understood on the basis of Heisenberg's uncertainty principle. The greater the uncertainty in the angular momentum (θ), the more certain is the measurement of the position (w). So the beam waist w is inversely proportional to θ.

[7] A more detailed analysis, assuming gaussian illumination, gives beam waist $W(l) = \sqrt{(2l\lambda)/(\pi n)}$ [20]

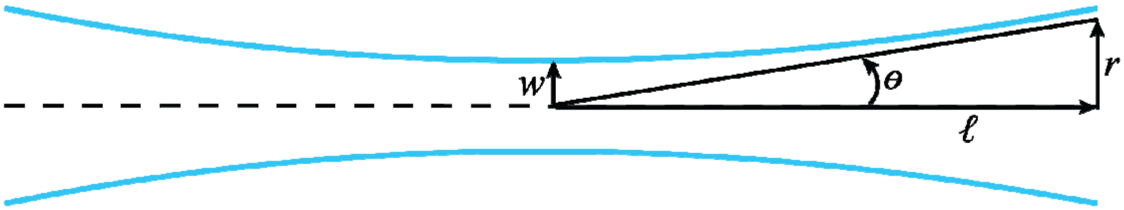

Figure 2.4: Gaussian Beam: A schematic of the gaussian beam, where θ is the angle of divergence, l is the displacement from the center, w is the beam waist at the center, r is the beam waist at distance l from the center.

thickness of the light sheet and the axial resolution of the objective (Fig. 2.5). The axial resolution of OCPI microscope is depicted in Fig. 2.6.

Alternate method to create light sheet Stelzer and colleagues recently developed an alternate method of creating a light sheet — called Digitally Scanned Light Sheet Microscope (DLSM) [38] . In DLSM, a sheet of light is produced by scanning a line of light (produced by a low NA aspheric lens) across the focal plane of the objective. DLSM allows for uniform illumination of the entire plane[8] [39]. It is yet to be seen if scanning is an effective method to create a light sheet in applications where there is need for high SNR imaging at high frame rates (such as neuronal activity imaging).

2.3 Light sheet positioning

An essential requirement of LSFM is the proper positioning of the light sheet at the focal plane of the objective. This positioning has been implemented differently in the various implementation of LSFM. In implementations by Huisken *et al.* and Dodt *et al.* the microscope objective does not move; the cylindrical lens is placed on a six-axis positioner[9] to position the light sheet at the objective's focal plane, and once positioned accurately it is fixed there permanently [33, 34]. This permanent positioning of the cylindrical lens and the objective forces the sample to be scanned (moved through the light sheet) to achieve 3D imaging. Such 3D imaging can only be performed on small samples and samples which are fixed (i.e. whose structure can remain rigid while it is being scanned).

OCPI microscopy was implemented with a goal that the sample remain fixed,

---

[8] If a gaussian beam passing through a cylindrical lens is used to produce a light sheet, the intensity of light is gaussian in the direction perpendicular to the light propagation. I.e. it produces a light sheet which has lower intensity at the sides compared to the center. Using DLSM one can obtain uniform illumination throughout the FOV.

[9] Three translational axes and three rotational axes

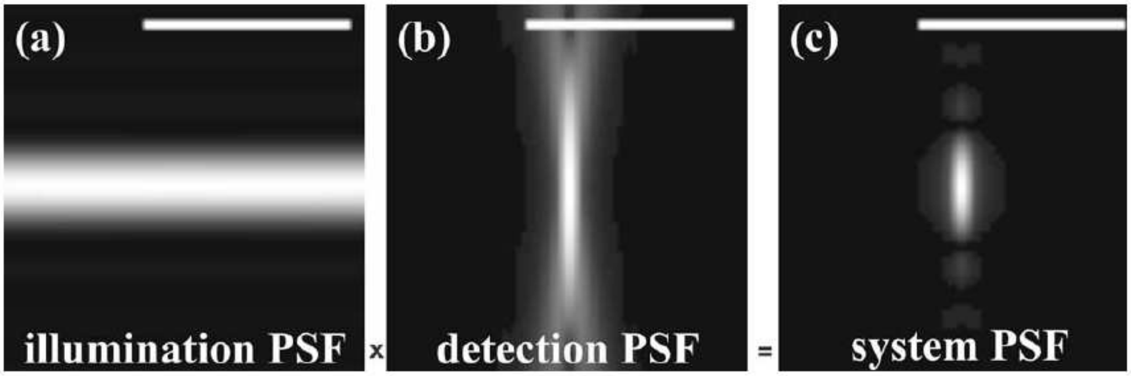

Figure 2.5: The axial resolution of LSFM depends on the thickness of light sheet **(a)** and axial resolution of the microscope objective **(b)**. The axial resolution of LSFM **(c)** is simply the product of the two PSFs (point spread functions) ((a) and (b)) (Adapted from [37]).

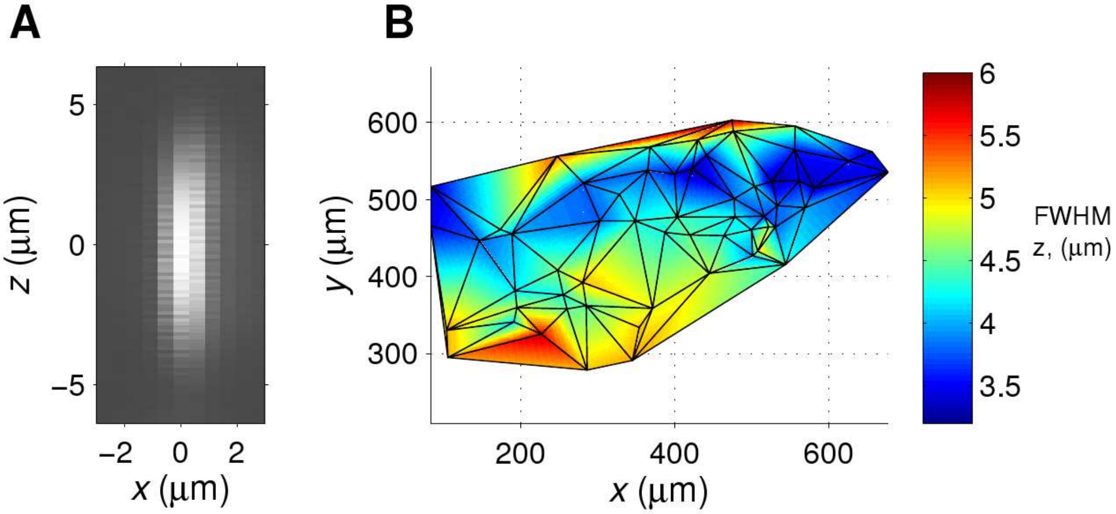

Figure 2.6: Characterization of the illumination sheet width in OCPI microscopy. **(A)** Three- dimensional image of a 2 μm fluorescent bead, rotated to show the axial direction (z) along the objectives optic axis as well as one lateral (x) axis. Frames were spaced every 0.1 μm along the z-axis by translating the piezoelectric objective positioner (Fig. 1). **(B)** The z-thickness of the image of 2 μm beads varies only slightly with lateral (x,y) position. For well-isolated beads (58 total), the full width at half max (FWHM) of the image along the z-axis was calculated. Each bead is represented at a vertex of the triangular surface, which is viewed from above; colorscale (at right) indicates the FWHM at each bead position. Blank areas indicate regions where no well-isolated bead was found. One notes that the sheet thickness does not vary strongly with x, but increases modestly along y with increasing distance from the waist.

but optics be made to move to create 3D imaging. To allow for such 3D imaging, the objective and the light sheet have to move together[10] [20]. We achieve such a configuration by aligning the light sheet to the objective and then rigidly coupling the light sheet to the objective. Thus when the objective is now made to move, the properly aligned light sheet also moves. We place the coupled optics on a piezoelectric manipulator; by moving the objective, we scan a different region of the tissue — leading to 3D imaging of tissue.

2.4 Detection axis

LSFM and epifluorescence microscopes are very similar in the detection axis (i.e. behind the objective). The detection axis consists of an emission filter, an infinity focused tube lens[11] and a fast camera. Ideally the focal length of the tube lens is optimized to allow for Nyquist criterion[12] to be fulfilled [19] — based on the physical size of the camera pixels and the lateral resolution of the objective[13]. Also, a high speed camera with high dynamic range will allow for high SNR imaging[14].

---

[10] In LSFM, the objective and the light sheet should always be positioned such that the light sheet is at the focal plane of the objective.

[11] Typically used microscopes use infinity focusing objectives — the rays from a single point in the sample are parallel behind the objective. A separate infinity focusing lens (tube lens) is used to converge the parallel rays back to a (diffraction-limited) point on the camera.

[12] Nyquist criterion can be described as the following: to measure a continuous signal with a precision of a frequency f, one will have to ideally digitally sample the signal at frequency $2f$.

[13] The lateral resolution of the objective depends on the NA of the objective and wavelength of light ($0.61\,\mathrm{NA}/\lambda$). For a typical application — 488 nm excitation and 0.5 NA objective — the lateral resolution is $\sim 0.6\,\mu$m. The pixel spacing on the camera — after correcting for the magnification in the optical system — should thus be less than $\sim 0.3\,\mu$m to fulfill Nyquist criterion.

[14] The upper limit on the SNR depends on the dynamic range of the camera. An 8 bit camera can measure changes no smaller than 1/256 while a 14 bit camera can measure changes as small as 1/16384.

2.5 Photobleaching

LSFM allows for low photobleaching imaging as compared to confocal microscopy. In confocal microscopy, both the in-focus and out-of-focus regions of the sample are continuously illuminated, leading to high photobleaching. In LSFM, photobleaching is lower due to the fact that only the in-focus region of the sample is illuminated. In [20] we show that OCPI microscopy has ∼100× less photobleaching as compared to confocal microscopy (Fig. 2.7). This advantage proves to be vital in imaging neural activity since the ultimate length of a given experiment is determined by photobleaching and phototoxicity; any decrease in these factors allows for longer neuronal activity experiments.

2.6 Neuronal imaging using OCPI microscope

In [20] we imaged Oregon Green BAPTA labeled Vomeronasal organ (VNO). Fig. 2.8 shows a 3D imaged volume containing ∼700 labeled neurons. The neurons were repeatedly imaged while applying different stimuli; the stimulus driven responsivity patterns of the identified neurons were obtained (Fig. 2.9). Repeated trials of a given stimuli were performed, and a robust functional characterization of the imaged neurons was obtained.

OCPI microscopy is not limited to imaging the VNO. Fig. 2.10 shows an image of a mouse olfactory bulb slice taken under OCPI microscope. One can clearly see layering of neuronal soma.

2.7 Improving OCPI microscopy

OCPI microscopy allows for imaging neuronal activity at pixel rates 100× faster than LSM. This speed advantage should lead to more widespread implementation of OCPI

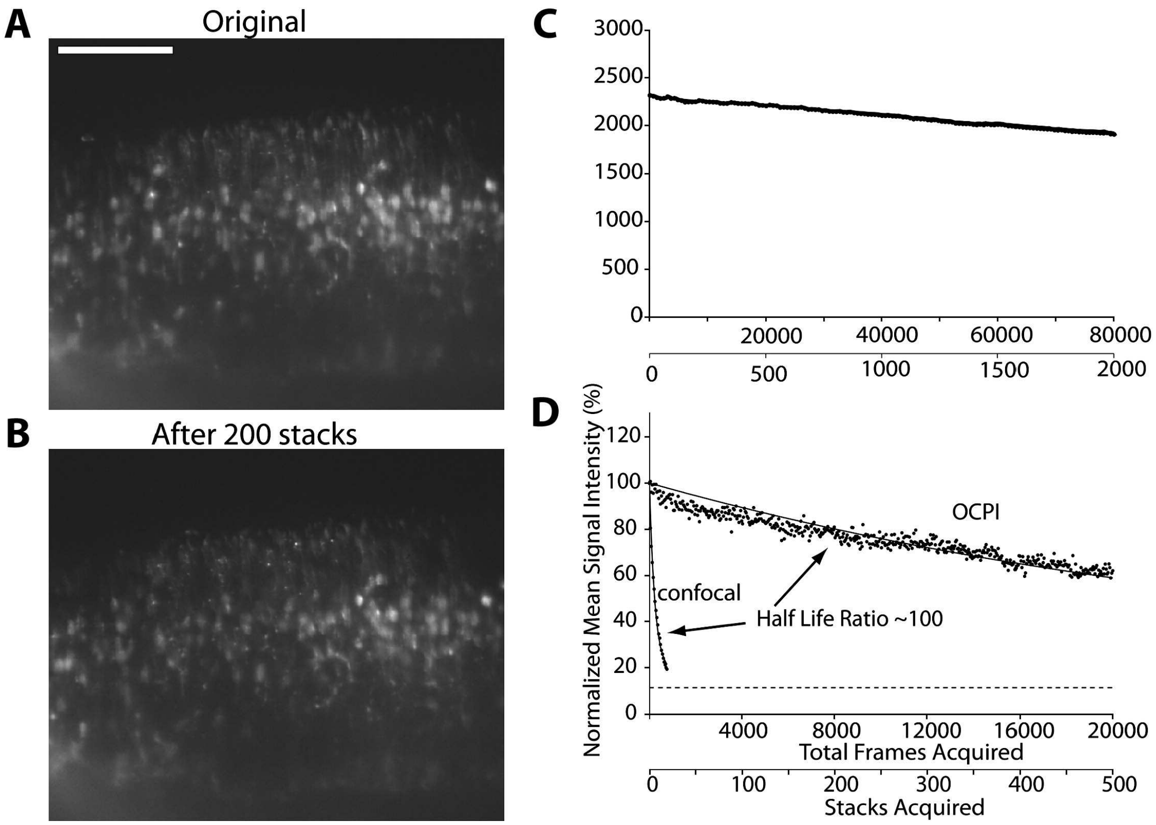

Figure 2.7: **(A and B)** Images from live excised VNO sensory epithelium loaded with Oregon green BAPTA-1. **(A)** Initial image from a calcium imaging experiment during which 40-frame stacks were taken every 6 sec. **(B)** shows the same optical section presented in (A) after acquisition of 200 stacks/ 8000 frames. Grayscale contrast limits are the same in (A) and (B). **(C)** Plot of mean signal intensity over time for the uppermost z-plane of each stack from an 80,000-frame (∼4.5 hr) experiment. Regression slope indicates the average photobleaching rate is ∼0.0002% intensity lost per frame acquired. **(D)** Controlled comparison of photobleaching rates reveals much slower bleaching by planar illumination than with a confocal microscope (Olympus FV1000). Repeated stacks (40 1M-pixel frames) were acquired of agarose-embedded FITC-dyed beads (2 μm diameter) with a 20× 0.5 NA objective. Laser intensities and scanning conditions were set to acquire ∼4000 photons in the brightest pixels of the initial image. Shown are mean signal intensities; decay rates were estimated using an exponential model with an unbleachable component indicated by the dashed line (see Experimental Procedures). Scale bar, 100 μm.

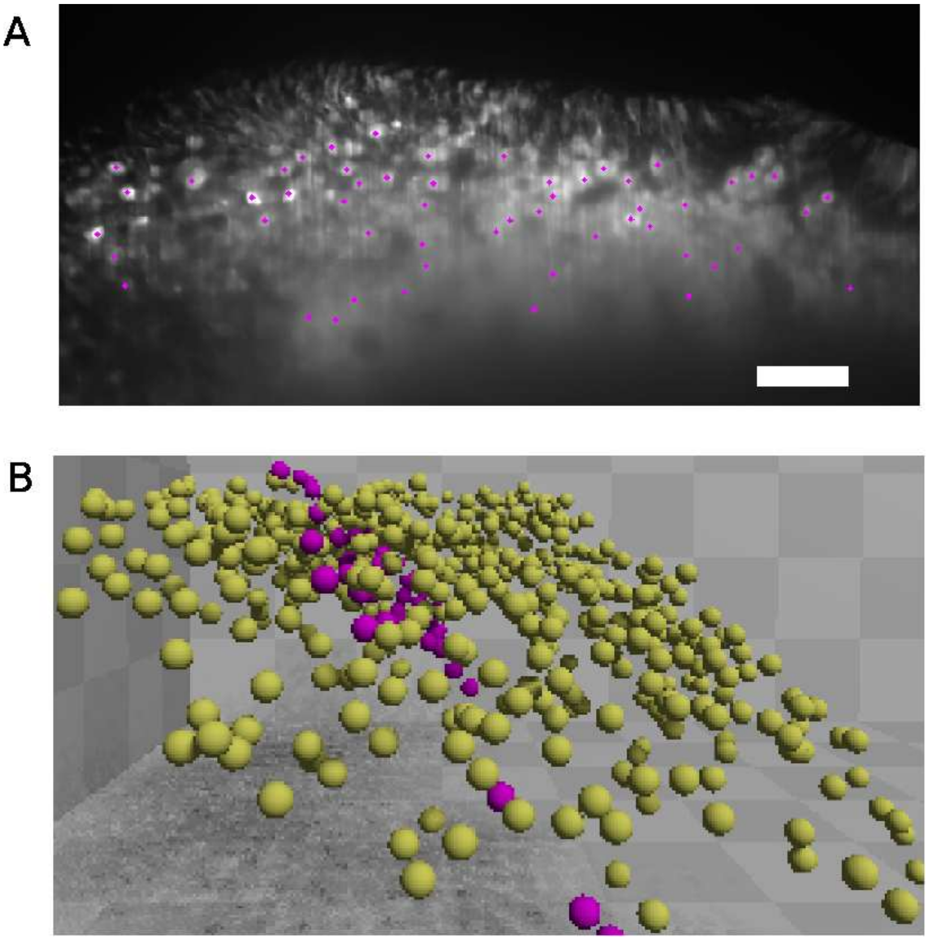

Figure 2.8: **(A)** Intact vomeronasal epithelium labeled with Oregon green BAPTA-1; single optical section by planar illumination. Purple dots indicate position of regions of interest (ROI) corresponding to single neurons. Scale bar = $50\,\mu$m **(B)** Three-dimensional rendering of the ROI positions for the entire 40-image stack. ROIs drawn in purple were in the single section pictured in (A). Sensory surface of the tissue is at the top.

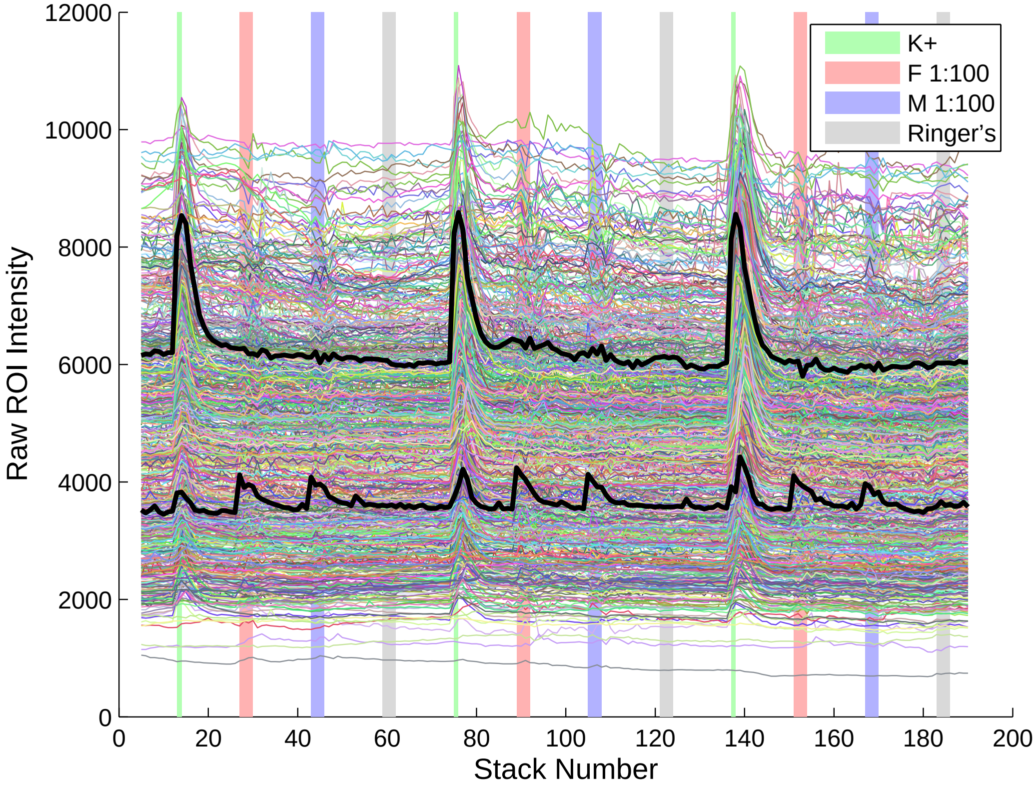

Figure 2.9: Probing responses to chemical stimuli of single VNO neurons by high-speed three-dimensional calcium imaging Intact vomeronasal epithelium labeled with Oregon green BAPTA-1; Raw total intensity of each ROI is plotted versus stack number. Stacks were taken every 5 sec. Two example traces are highlighted in black. Stimuli are K+ (High Potassium Ringers), F 1:100 (female mouse urine at a 1:100 dilution), M 1:100 (male mouse urine at a 1:100 dilution), and Ringer's solution.

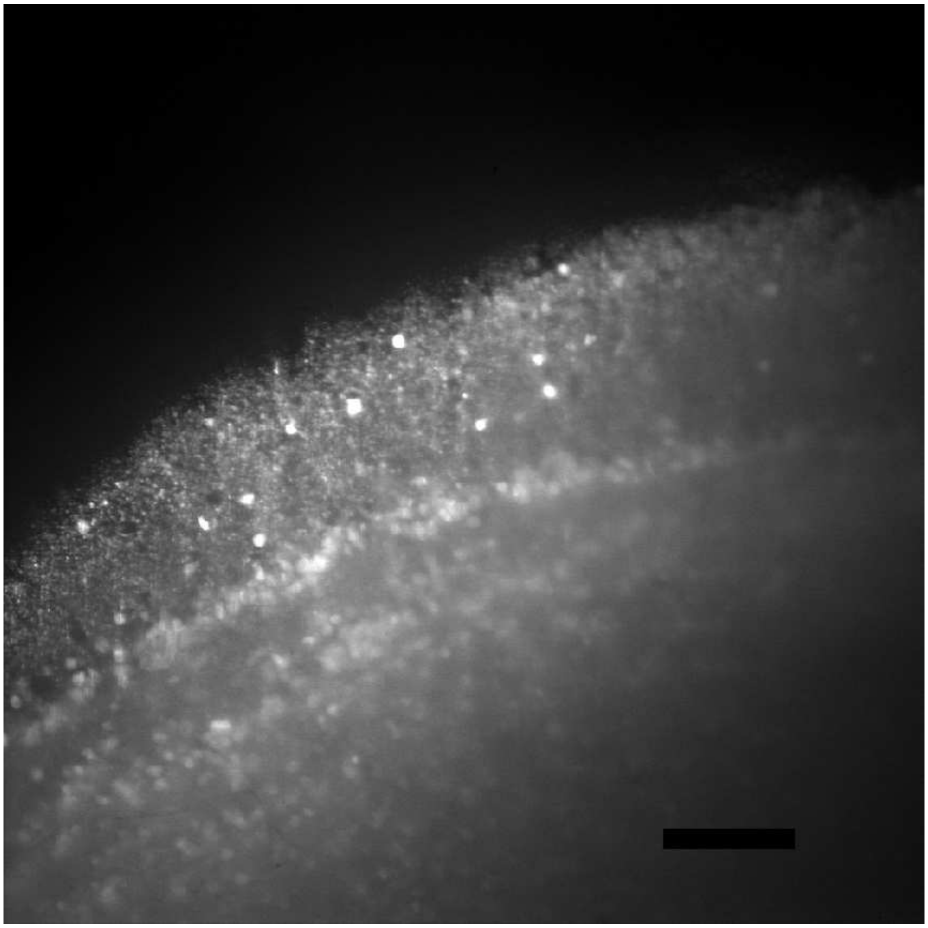

Figure 2.10: An OCPI microscope image of a 500 μm thick slice of olfactory bulb from a GAD65-GFP mouse. Scale bar = 100 μm

microscopy in the neuroscience community. But in order to make OCPI microscopy more appealing to the neuroscience community there are a few improvements which can be made to the OCPI microscope design:

(1) The current OCPI microscope design has bulky objective coupler and illumination optics. The bulk makes it difficult to, for example, perform simultaneous imaging and electrophysiology experiments — there is little space to introduce an electrode into the preparation while imaging the tissue. More space can be created by miniaturizing the optics and the coupler.

(2) In optimal LSFM imaging conditions[15] the lateral resolution depends on the numerical aperture (NA) of the objective and the axial resolution is a function of the light sheet thickness and the NA of the objective. Higher NA objectives lead to better lateral resolution; higher NA cylindrical lens with high NA objectives allows for better axial resolution. But in OCPI microscopy on neuronal tissue, the tilted imaging configuration leads to significant aberrations (Fig. 2.11). A higher NA objective will collect larger number of rays which are "more-refracted," leading to lower contrast. Thus paradoxically, higher NA objectives lead to worser lateral resolution due to larger contribution of aberrations. These aberrations can partly be corrected using adaptive optics (AO). Improving the image resolution deeper into tissue will allow for applying the microscope in more diverse neuroscience applications.

In Chapter 3, I will describe the miniaturization of OCPI microscopy and the correction of one of the basic aberrations (defocus) in OCPI microscopy. In Chapter 4, I will describe the calibration of a deformable mirror in OCPI microscopy setting; a well calibrated deformable mirror is essential in implementing adaptive optics to compensate aberrations in OCPI microscopy. In the same chapter I will also show the preliminary results of implementing adaptive optics for OCPI microscopy; the data suggest that the implementation of adaptive optics to OCPI microscopy leads

---

[15] For example, imaging beads embedded in agar ($n \approx 1.33$) using a water immersion objective

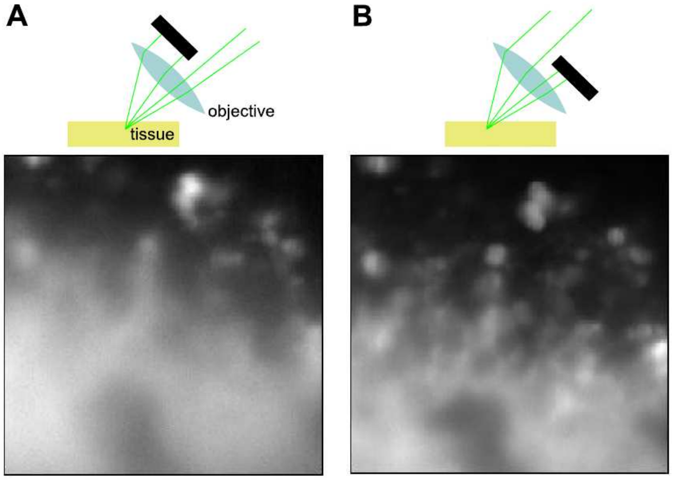

Figure 2.11: Aberrations limit resolution in OCPI microscopy. **(A)** Image of vomeronasal tissue with a 40× NA 0.8 objective in which the half of the objective transmitting the less-refracted rays was blocked. Image is exceptionally blurry. **(B)** Image of the identical field with the same objective in which the half with the more-refracted rays was blocked. Image is less blurry, but still contains significant aberration.

to higher resolution imaging deeper into tissue.

Chapter 3

Miniaturization and Defocus correction for OCPI microscopy

3.1 Introduction

Epifluorescence microscopy and laser scanning (confocal and multi-photon) fluorescence microscopy (LSM) have become indispensable tools in biology, but each of these techniques has a fundamental limitation. Epifluorescence has little depth resolution and thus encounters difficulty when imaging thick samples. LSM, with its sequential pixel scanning, encounters a fundamental tradeoff among speed, imaged area, and signal-to-noise ratio [20].

One approach to overcome these limitations is planar illumination microscopy [20, 30–34]. A thin sheet of light (typically formed with a cylindrical lens) is projected from the side and positioned to illuminate the focal plane of the objective, exciting fluorescence only in the in-focus portion of the sample. This achieves optical sectioning, and eliminates photodamage in out-of-focus regions of the sample. Moreover, because emission from all illuminated points can be collected simultaneously, this approach permits entire images to be collected quickly at high signal-to-noise ratios. High speed and low phototoxicity are essential for imaging fast events, such as electrical activity in large populations of neurons [20].

In our implementation of planar illumination, OCPI [20], the light sheet is rigidly coupled to the objective so that both can be rapidly translated together to attain fast three dimensional imaging. In this letter we report improving OCPI by: 1) Miniaturizing the objective laser coupler and 2) Correcting defocus aberrations that arise from refractive index mismatch.

3.2 Miniaturization of OCPI optics

In this new implementation of OCPI, we reduce the optical requirements to a single component: a uniaxial (cylindrical) GRIN lens. A GRIN lens bends light by having an index of refraction n that is highest in the center and falls off quadratically towards the edge, $n = n_0(1 - (gy)^2)$, where n_0 is the index of refraction at the center, y is the distance from the center, and g measures how quickly the refractive index changes with distance [40]. We employ a slab-shaped GRIN lens whose index of refraction varies only along one axis (as opposed to typical GRIN lenses whose n changes radially), thus behaving as a cylindrical lens. The custom GRIN lens (GRINTECH GmbH, thickness 1mm, width 3 mm, length 2.66mm, n_0 1.524, g 0.26/mm, working distance of 3.5 mm in water) is mounted on a custom objective collar that permits micropositioning of the light sheet [Fig. 3.1(a)].

The thickness of the light sheet over the field of view is determined by tuning the numerical aperture (NA) of the GRIN lens [20] using a slit at the rear aperture. In our current implementation, a 488 nm laser (Coherent 488-20) directly illuminates the back aperture of the GRIN lens to give a diffraction limited light sheet with a waist of 3-5 μm thick across a field hundreds of microns in size (Fig. 3.1(c)). Light collected by the objective (Olympus, 20× water immersion, NA 0.5) is focused by a

200mm tube lens (Edmund Optics) onto a CCD camera (Scion CFW-1308M). This configuration of using uniaxial GRIN lens with free space laser coupling leads to a substantial decrease in bulk of the illumination arm compared with our previous design [20], permitting a wider range of samples to be imaged — such as imaging murine cortex through a craniotomy in an anesthetized mouse (Fig. 3.3).

3.3 Defocus correction

OCPI images of tissue are degraded in part by scattering, which arises from inhomogeneities in the refractive index of the sample. However, image quality is also affected by low-order aberrations that arise from bulk index-mismatch: the immersion fluid has a refractive index $n_f = 1.33$ while the tissue sample typically has an average refractive index $n_s \approx 1.36 - 1.40$ [41]).

To study the consequences of this refractive index mismatch, we calculated the deviations of meridional paraxial rays under the idealization of an optically-homogeneous tissue sample. We assumed that the interface between two homogenous media, fluid and sample, is planar, with the normal vector at an angle α with respect to the optic axis [Fig. 3.4(a)]. Suppose also that we idealize the incident illumination as a plane, which is at an angle β with respect to the optic axis, and that the normal of the illumination plane lies in the same plane as the sample normal and the optic axis. Using Snell's law and assuming that the difference $\Delta n = n_s - n_f$ is small, one obtains $\theta_i \approx -(\Delta n/n_f)\tan\gamma_s$, where γ_s is the angle between the interface normal and the light sheet inside the sample [Fig. 3.4(b)]. So if the illumination plane coincides with the focal plane in the fluid, the two will not remain coincident in the sample, with the separation increasing deeper into the sample.

However, the total defocus also must account for a second phenomenon, the deviation of the emitted (collected) rays at the fluid/sample interface [Fig. 3.4(c)]. Parax-

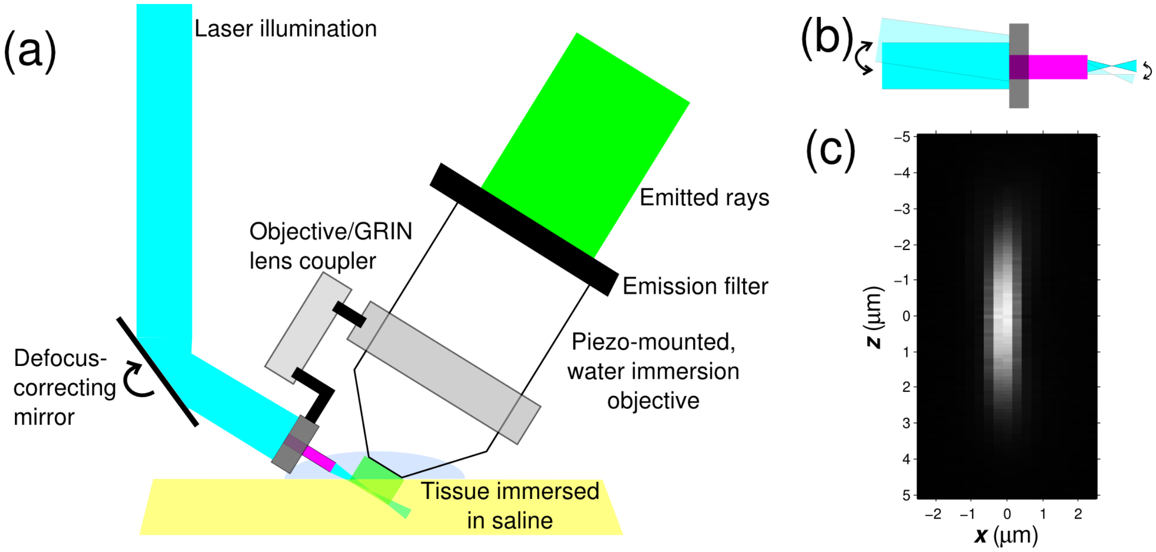

Figure 3.1: Schematic and calibration of OCPI microscope. (**a**) Schematic of miniaturized objective coupler. Uniaxial GRIN lens is positioned such that a sheet of light is formed at the depth of focus of the objective. (**b**) Angular defocus adjustment is obtained by changing the angle of incident light. (**c**) Example axial image of a $0.2\,\mu$m fluorescent bead in agar.

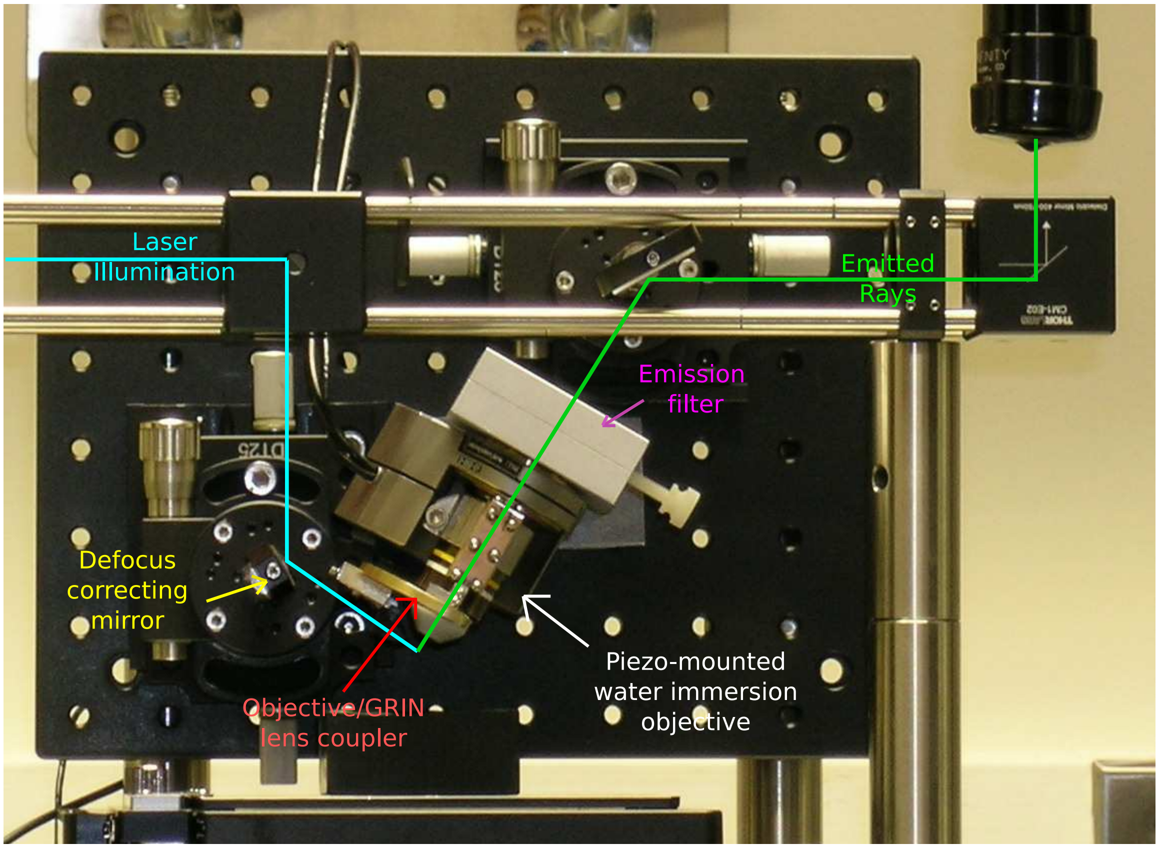

Figure 3.2: Picture of second generation OCPI microscope. Its two major design improvements over the first generation OCPI microscope are (1) miniaturized objective coupler and cylindrical lens system, and (2) defocus correcting mirror.

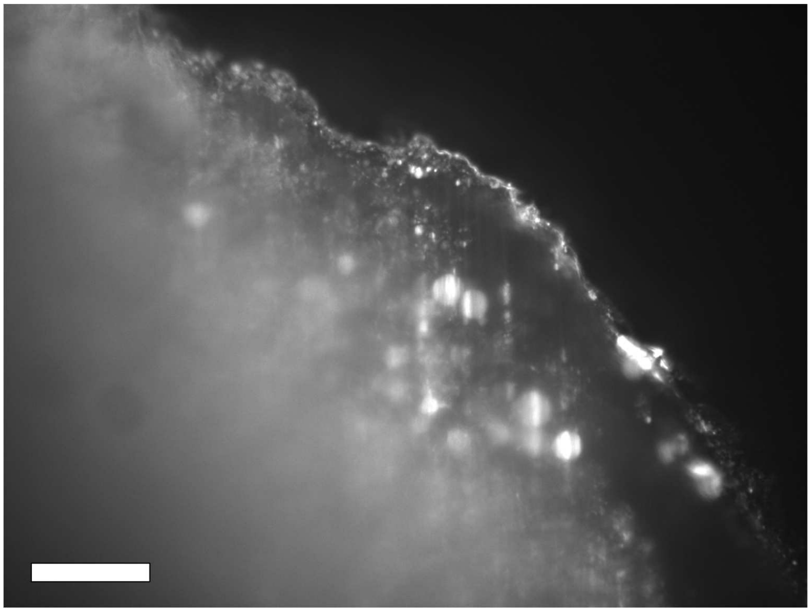

Figure 3.3: Image of olfactory bulb in an anesthetized mouse. The miniaturized OCPI optics allows for *in vivo* imaging of cortex of anesthetized mouse through a small craniotomy. Scale bar = $50\,\mu$m.

ial rays emitted from one object location O will appear to be emitted from a virtual source O' whose position can be determined by back-tracing the rays in the fluid. For a source point at a depth d below the interface as measured along the optic axis, the back-traced virtual rays intersect at a distance $s = d\frac{n_f \cos^2 \alpha'}{n_s \cos^2 \alpha}$, where α' is the angle between the interface normal and the refracted axial ray. (This is derived by considering two meridional rays emitted at angles $\pm\epsilon$ from the optic axis: to first order in ϵ, they strike the interface at points separated by $2\epsilon d/\cos\alpha$, and are refracted at angles that differ by $2\epsilon(n_s/n_f)\cos\alpha/\cos\alpha'$. The expression for s then follows using the law of sines.) If z measures along the optic axis, and y in the meridional plane, the apparent position shift of the object is $\Delta z = d - s\cos(\alpha' - \alpha)$ and $\Delta y = s\sin(\alpha' - \alpha)$. Note in particular that the deviation is linear in d, which means that for objects O in the illumination plane, the virtual origins O' also lie in a plane, but one that is tilted with respect to the illumination [Fig. 3.4c].

To correct the defocus of emitted rays, we need to ensure that the *virtual* source plane (rather than the illumination plane) lies in the focal plane of the imaging system (Fig. 3.4c). The illumination plane must therefore be tilted at an angle θ_c relative to the focal plane (the plane perpendicular to the optic axis). This angle is determined by the requirement that the position shift Δz for each illuminated point places it along a line perpendicular to the optic axis. For small Δn one finds

$$\tan\theta_c \approx \frac{\Delta n}{n_f}\left(1 + 2\tan^2\alpha\right)\tan\alpha \tag{3.1}$$

Fig. 3.4(d) shows the combined effect of the deviation of the illumination plane [Fig. 3.4(b)] and of the deviation of the emitted rays [Fig. 3.4(c)] in setting the ideal illumination angle [Fig. 3.4(a)] $\beta = \pi/2 + \Delta\beta$, where theoretically $\Delta\beta = \theta_i - \theta_c$.

Thus there is a small angular change ($\Delta\beta$) required to ensure that the illumination plane is properly positioned for the objective. By placing a mirror on a rotation stage

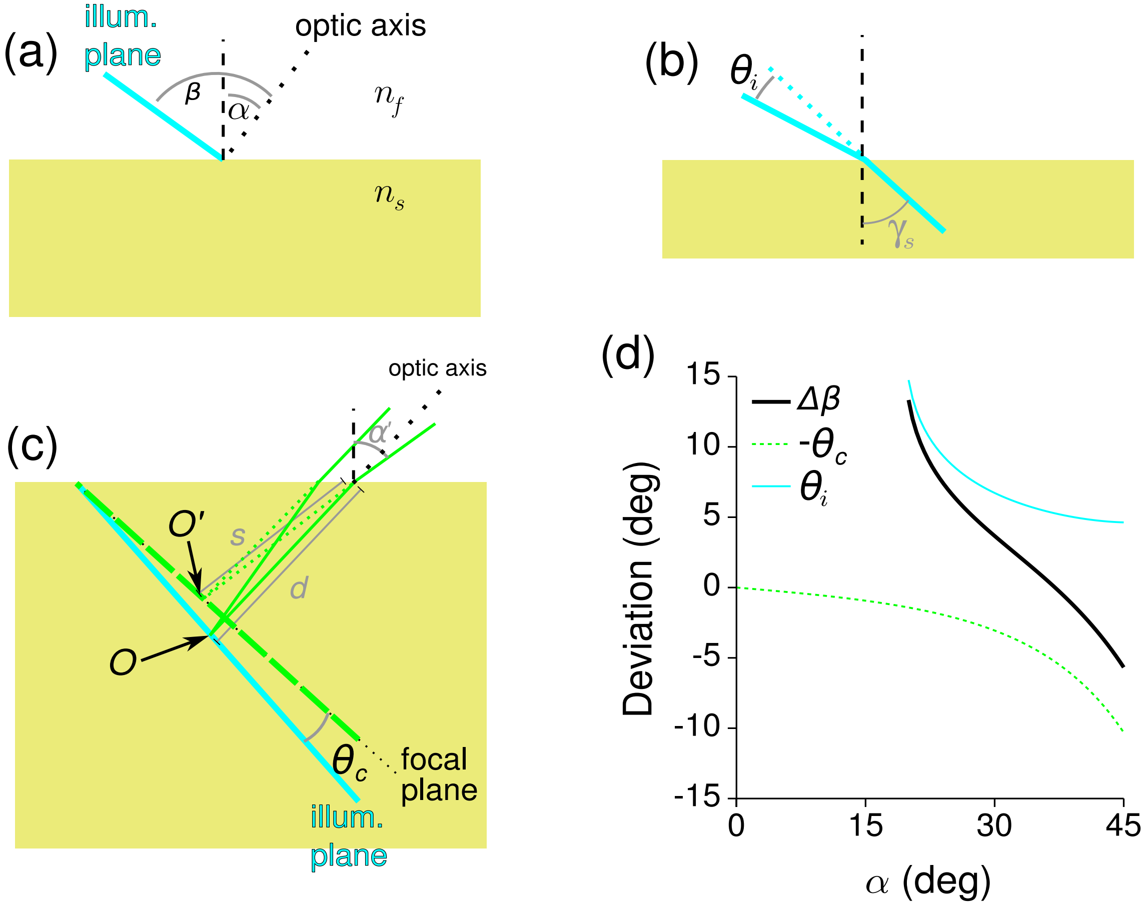

Figure 3.4: Sources and magnitude of defocus in tilted configurations of planar illumination microscopy. (**a**) Illumination strikes the sample/fluid interface at an angle; the optic axis is also tilted, at an angle α. The fluid has an index of refraction n_f, the sample n_s. (**b**) The illumination plane bends at the fluid/sample interface through an angle θ_i. (**c**) The emitted rays are bent at the interface, resulting in a virtual object location that resides on a different plane. (**d**) The magnitude of both effects, and their combination ($\Delta\beta$), for $n_f = 1.33$ and $n_s = 1.40$.

(Thorlabs), we were able change the angle of incident laser onto the back aperture of the GRIN lens to produce the required few degrees change in the illumination angle [Fig. 3.1(b)].

To test the effect of angular defocus, we imaged 0.2 μm fluorescent beads in water (n=1.33) and polydimethylsiloxane (PDMS, Dow Corning, DC 184-A and DC 184-B with a weight ratio of 10:1, n=1.40). When imaging beads in water (10 ms exposure time to limit the effects of diffusion), we tuned for the angle which produced the least defocus aberration throughout the imaged plane. This setting corresponds to the illumination axis being orthogonal to the objective axis (thus under our definition $\Delta\beta = 0°$) [Fig. 3.5(a)]. Under the same angular setting, beads in PDMS were increasingly blurry at increasing depths[Fig. 3.5(b)], as expected theoretically [Fig. 3.4].

We then tuned the illumination to find the optimum angle (determined experimentally as $\Delta\beta \approx 5.4°$) that minimized defocus aberration in beads embedded in PDMS[Fig. 3.5(d)]. At such an angle the beads in PDMS were adequately in focus across the field of view, with small defects in image quality from uncorrected higher-order aberrations. At this new angle, as expected, the beads immersed in water were considerably out of focus at increasing distance[Fig. 3.5(c)]. The 5.4° corresponds well with the theoretical prediction [Fig. 3.4(d)] of 3° for $\alpha = 30°$.

To see the net improvement of the miniaturized OCPI with defocus correction, we imaged a slice of olfactory bulb from a GAD65-GFP mouse [42]. A 500 μm thick tissue section was imaged under the old and new OCPI microscopes. Since the refractive index of the tissue is unknown, we empirically tuned the illumination angle, which for this sample was optimized at $\Delta\beta \approx 1.7°$. The improvement in image quality between the two instruments is striking. The remaining loss of sharpness deeper into the tissue is due to a combination of scattering and uncorrected classical aberrations (as seen in Fig. 3.5d). These remaining aberrations might be corrected by other methods,

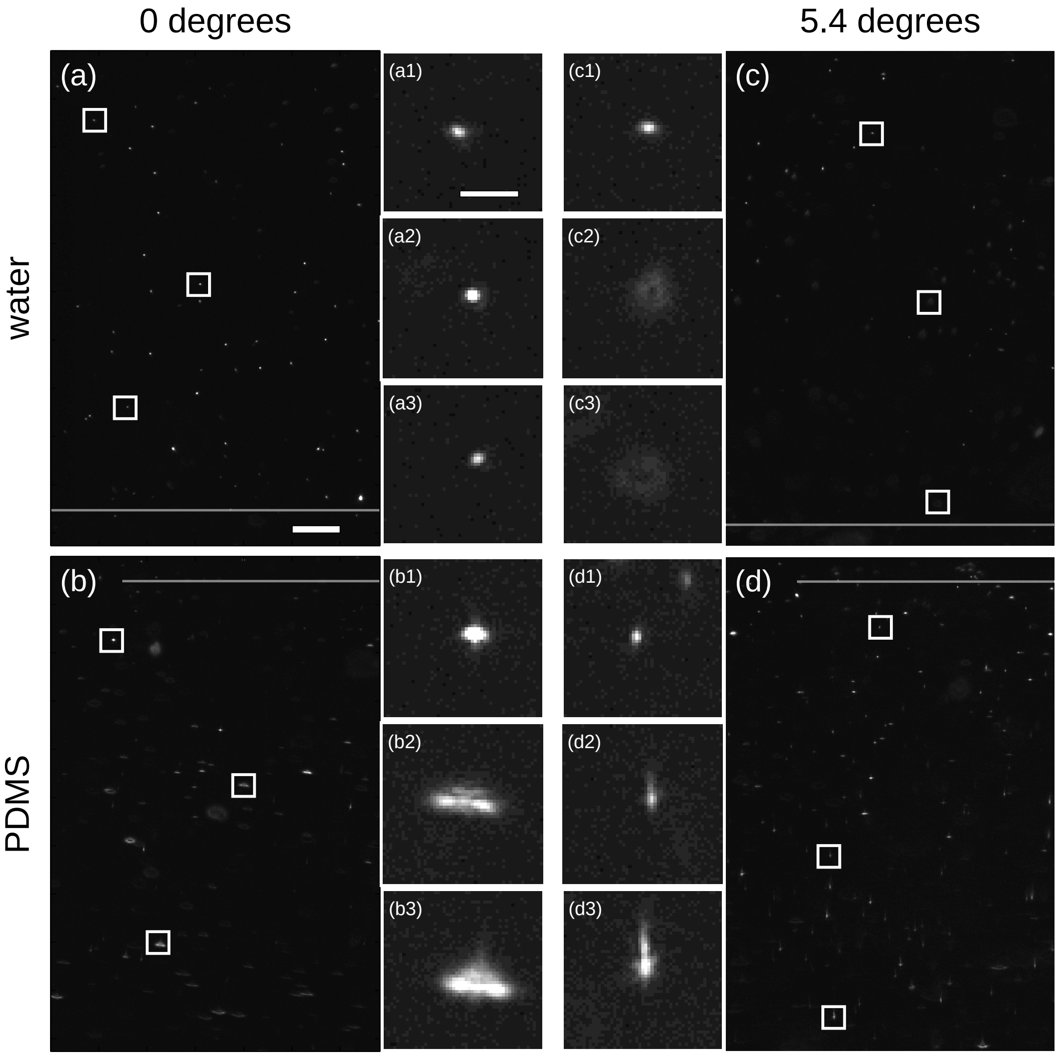

Figure 3.5: Defocus measurement. (**a**) Beads in water ($n = 1.33$) were imaged under OCPI. At this illumination angle, the image of beads is diffraction-limited. Insets are three different beads at three corresponding depths. Dotted line represents water/PDMS interface. (**b**) Beads in PDMS ($n = 1.40$), at same angle as (a). As expected, as depth increases, the defocus increases. (**c**) Beads in water. At an angle tuned for beads in PDMS, the beads in water are increasingly defocused as the "depth" increases. (**d**) Beads in PDMS at the same angle as (c). Although there are some higher-order aberrations, the beads are in focus at all depths. Scale bar in (a), 25 μm. Scale bar in (a1), 5 μm.

including adaptive optics, which should lead to even greater improvement in image sharpness deeper into tissue.

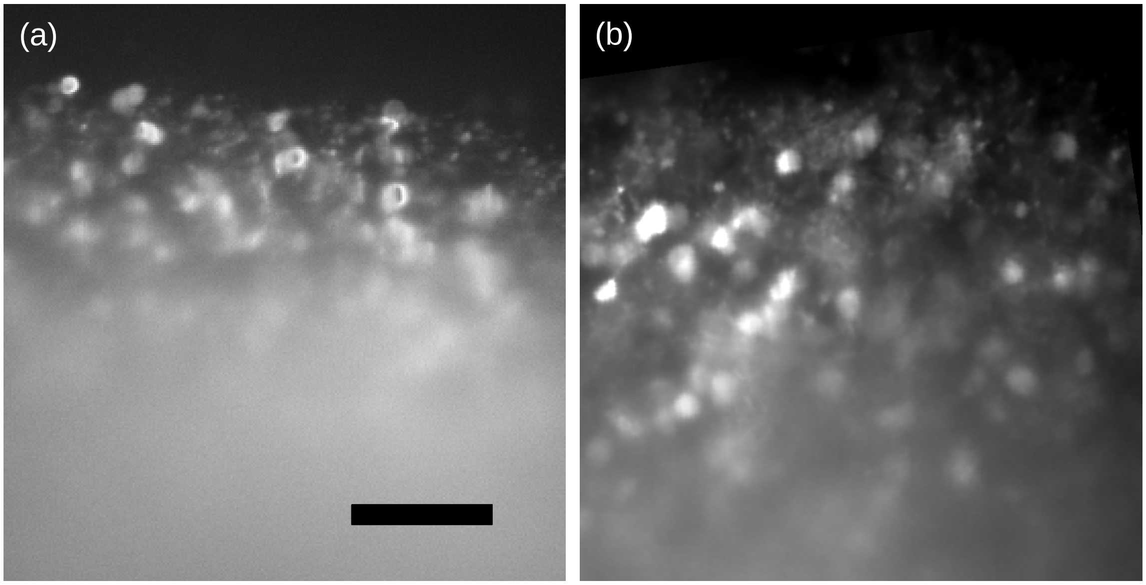

Figure 3.6: Resolution enhancement with miniaturized objective coupler with defocus correction. Images of a slice of olfactory bulb were taken under the same conditions with old (**a**) and new (**b**) OCPI microscopes. Scale bar 50 μm.

Chapter 4

Adaptive Optics for OCPI microscopy

4.1 Introduction

Light is refracted by biological tissues. This interaction can be exploited to generate image contrast; however, refractions also present a significant hindrance to image resolution deeper into tissue. The interactions between light and tissue are conventionally discussed in terms of two extremes: “scattering” typically describes the effects of small inhomogeneities in tissue, whereas the term “aberrations” most commonly refers to refractions induced by bulk (average) properties of tissue [19]. One common source for aberrations is the mismatch in index of refraction between the immersion fluid and the sample; for example, water or saline has a refractive index near 1.33, but tissue typically has a variable refractive index ranging from 1.36–1.40 [41].

In a situation in which the tissue is face-on with the objective (i.e., the tissue surface is orthogonal to objective’s optical axis), this refractive index mismatch leads primarily to two types of aberrations – defocus and spherical aberration [43]. The defocus aberration is often not even noticed (it is corrected by changing the focus of the objective), but the spherical aberration typically remains uncorrected and serves as an impediment to imaging deeper into the tissue. More problematic is the case where the tissue is not perfectly flat and/or the tissue surface is not orthogonal to the objective axis, because additional aberrations, which can be substantially larger, are introduced into the images ([44] and Chapter 3). An extreme case of such tilted imaging is found in a light-sheet based microscopic technique called objective coupled planar illumination microscopy (OCPI) [20].

In typical light-sheet microscopy (also sometimes called planar illumination microscopy) a cylindrical lens is used to create a sheet of light [20, 32–34]. This sheet of light is placed at the focal plane of the objective and the tissue is placed in this overlap region. This arrangement allows for only the in-focus region of the tissue to be illuminated and allows for the entire illuminated plane to be imaged simultaneously. Thus light-sheet microscopy allows for high speed and low photo-toxic imaging. To use such light-sheet microscopy to image large samples (i.e., the surface of the mouse brain *in vivo*), one should minimize the distance in tissue traversed by the excitation light and emitted light; consequently, the light sheet is tilted with respect to the tissue surface, and the objective is tilted correspondingly [Fig. 4.3(a)]. This tilted imaging introduces sizable new optical aberrations, including defocus, coma, and astigmatism. Previously we showed that the defocus aberration can be corrected by tilting the angle of the light sheet by a few degrees [44]. We hypothesize that wavefront-correcting techniques such as adaptive optics (AO) can be used to correct the remaining aberrations.

AO has been used in a variety of settings, initially by astronomers to correct the loss of resolution in images taken from earth-bound telescopes due to atmospheric turbulence [45]. In AO, a wavefront sensor (typically Shack-Hartmann Wavefront Sensor, SHWFS) is used to measure the aberrations, and a deformable mirror (DM) is used to correct the wavefront to achieve diffraction limited imaging (Fig. 4.1). The resulting improvement in image quality has made adaptive optics an integral part of major new ground-based telescope designs. Similar adaptive optics systems have also been used in vision science where the aberrations of the eye can be measured and corrected [46].

The most crucial element of any AO system is the wavefront sensor; here we focus on this problem as it applies to wide-field microscopy. A SHWFS is difficult to apply directly to most applications in microscopy because tissue samples typically lack point-source emitters [43]. Consequently, several alternative methods for wavefront sensing have been developed. Coherence-gated techniques [47,48] are applicable only when using a broadband light source, and these methods introduce some degree of complexity in the apparatus. A more general and (in terms of instrumentation) simpler approach is to use the images themselves to estimate the wavefront aberration. Approaches that iteratively improve the "sharpness" of an image have been found to be applicable in microscopy [49,50]. But such methods require large number of iterations and/or large number of images, and thus place constraints on the speed and fluorescence levels of the biological preparations. Phase retrieval is a method used to measure the point-spread-function (PSF) of the microscope [51], but such a method is not capable of measuring wavefront aberrations of extended objects. However, a closely related method—phase diverse imaging (PDI)—is capable of measuring wavefront aberrations of extended objects [52,53]. Phase diverse imaging can be described as follows: In a typical imaging experiment there are two unknowns, (i) the object and (ii) the wavefront aberration (PSF); a single image is insufficient to accurately measure the two unknowns. In typical PDI, one image is acquired with the camera in-focus and a second image is acquired with the camera slightly out-of-focus (Fig. 4.2). Thus with the two known images the two unknowns (object and wavefront aberration) can be extracted computationally [52,53]. In principle, such an image-based wavefront sensor is readily applicable in the high signal-to-noise imaging performed

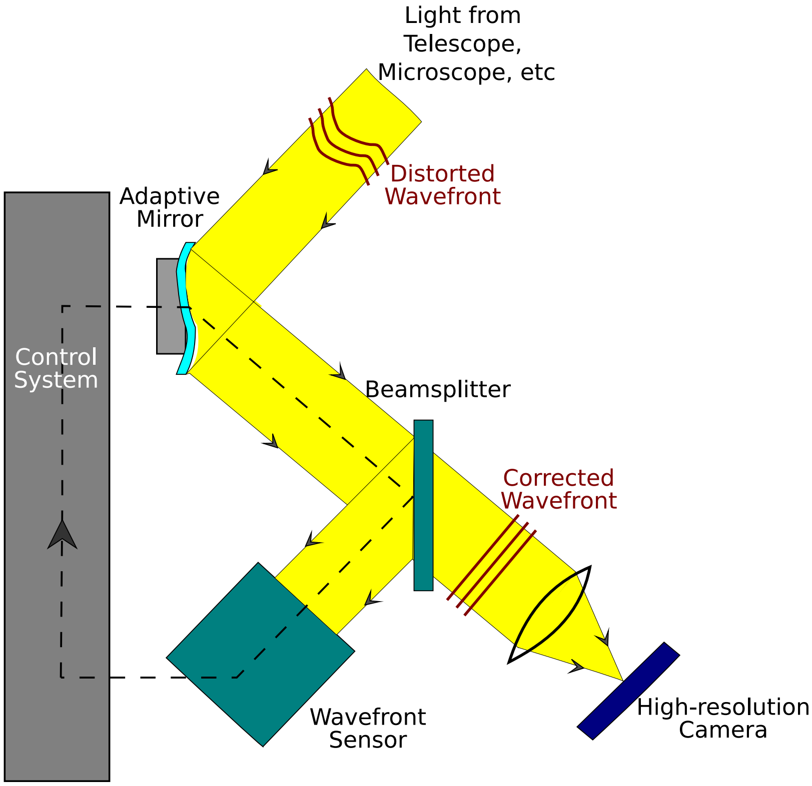

Figure 4.1: General schematic of an adaptive optics system (adapted from http://cfao.ucolick.org/). The two main components of an AO system are the wavefront sensor and adaptive element (usually a deformable mirror) which compensates for the wavefront aberration.

through OCPI microscopy.

4.2 Theory: Phase-diverse imaging

Consider a base object emitting light with (scalar) intensity $f(\mathbf{x})$ at the position $\mathbf{x}$ in a two-dimensional plane. (One challenge in applying traditional phase-diverse imaging to microscopy is the extended, three-dimensional nature of typical objects. The localization of excitation in light-sheet microscopy makes its application more straightforward.) A total of K different images are collected of this fixed object; these images have different aberrations, which here are generated by different settings of the voltages for the DM. These K *diversity images* are denoted $d_k(\mathbf{x})$, $k = 1, \ldots, K$. The PSF for the kth diversity image is denoted $s_k(x)$, and because the imaging path is incoherent we write

$$s_k(\mathbf{x}) = |h_k(\mathbf{x})|^2 \tag{4.1}$$

where h_k is the inverse Fourier transform of the optical transfer function for coherent illumination, H_k. Explicitly,

$$h_k(\mathbf{x}) = \mathrm{FT}^{-1}[H_k(\mathbf{u})] = \int \mathrm{d}\mathbf{u}\, e^{-2\pi\imath\mathbf{u}\cdot\mathbf{x}} H_0(\mathbf{u}) e^{\imath\phi_k(\mathbf{u})} \tag{4.2}$$

where FT^{-1} is the inverse Fourier transform, $\mathbf{u}$ is a point in the pupil, H_0 is the aperture mask (usually zero outside the pupil and one inside) and ϕ_k is the aberration phase associated with the kth diversity image.

The unknowns, f and the set $\{\phi_k\}$ of all aberration phases, will be determined by nonlinear optimization, minimizing the square-difference between observed (d_k) and predicted ($s_k * f$, where $*$ is convolution) images:

$$E[f, \{\phi_k\}] = \sum_{k=1}^{K} \int \mathrm{d}\mathbf{u}\, |D_k(\mathbf{u}) - F(\mathbf{u}) S_k(\mathbf{u})|^2 \tag{4.3}$$

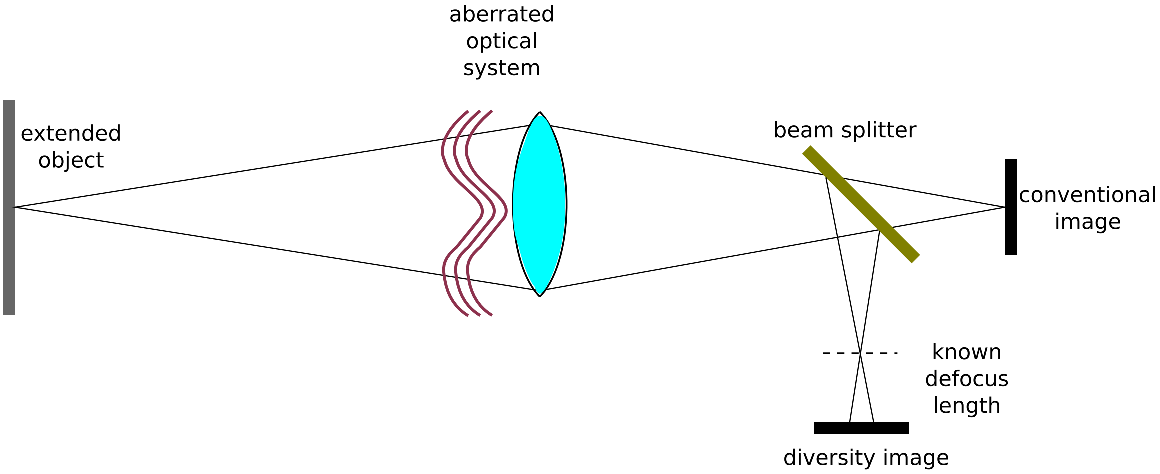

Figure 4.2: Schematic of a typical phase diversity system: The image acquired by a microscope depends on both the object being viewed and the nature of any aberrations. These two unknowns cannot be determined from a single image; however, by acquiring two (or more) images that differ by application of an additional known aberration, one obtains sufficient data to resolve this degeneracy (Adapted from [53]).

where D_k, F, S_k are the fourier transforms of d_k, f, s_k respectively.

As shown previously [52, 53], the penalty Eq. (4.3) can be converted to a pure function of the ϕ_k by substituting the analytic solution for the optimum F,

$$F = \sum_{k=1}^{K} D_k S_k^{\dagger} / \sum_{l=1}^{K} |S_l|^2, \tag{4.4}$$

where † is the complex conjugate, leading to a phase-only penalty function

$$E'[\{\phi_k\}] = \int d\mathbf{u} \, \frac{\left| \sum_k D_k(\mathbf{u}) S_k^{\dagger}(\mathbf{u}) \right|^2}{\sum_l |S_l(\mathbf{u})|^2} - \int d\mathbf{u} \sum_k |D_k(\mathbf{u})|^2 . \tag{4.5}$$

We note that the second term does not depend upon the aberration. In minimizing the resulting penalty function, the speed of convergence is substantially enhanced by using the penalty gradient [53], which for our parametrization is

$$\frac{\delta E'}{\delta \phi_k(\mathbf{u})} = 4\mathrm{Im} \left[\sum_{k=1}^{K} H_k(\mathbf{u}) \, (Z_k * H_k^{\dagger})(\mathbf{u}) \right] \tag{4.6}$$

where

$$Z_k = \Big[\sum_l |S_l|^2 (\sum_j D_j S_j^{\dagger}) D_k^{\dagger} - |\sum_j D_j S_j^{\dagger}|^2 S_k^{\dagger} \Big] / \left(\sum_l |S_l|^2 \right)^2 . \tag{4.7}$$

4.3 Theory: ϕ parametrization

For a parametric representation of $\{\phi_k\}$, Eq. (4.6) allows the derivative with respect to any parameter p to be calculated via the chain rule,

$$\frac{\partial}{\partial p} = \sum_k \int d\mathbf{u} \, \frac{\partial \phi_k(\mathbf{u})}{\partial p} \frac{\delta}{\delta \phi_k(\mathbf{u})} . \tag{4.8}$$

4.3.1 Gaussian parametrization

Since individual actuators are expected to have a localized influence in the pupil plane, one simple (few-parameter) approximation of the aberration phase would be a Gaussian. (Here, the primary value of a Gaussian parametrization is to provide an initial guess for a more accurate method requiring more parameters.) We postulate that the phase aberration can be approximated as

$$\phi(\mathbf{u}) = Ae^{-(\mathbf{u}-\mathbf{u}_0)^2/2\sigma^2} \tag{4.9}$$

where A is the amplitude of deformation, $\mathbf{u}_0$ is the center of deformation, and σ is the estimate of the width of the deformation. The partial derivative of ϕ_k with respect to the parameters is

$$\begin{aligned} \frac{\partial \phi_k}{\partial A} &= e^{-(\mathbf{u}-\mathbf{u}_0)^2/2\sigma^2}; && (4.10) \\ \nabla_{\mathbf{u}_0} \phi_k &= \frac{A(\mathbf{u}-\mathbf{u}_0)}{\sigma^2} e^{-(\mathbf{u}-\mathbf{u}_0)^2/2\sigma^2}; && (4.11) \\ \frac{\partial \phi_k}{\partial \sigma} &= \frac{A(\mathbf{u}-\mathbf{u}_0)^2}{\sigma^3} e^{-(\mathbf{u}-\mathbf{u}_0)^2/2\sigma^2}. && (4.12) \end{aligned}$$

Together with Eq. (4.6) and (4.8), these equations allow one to calculate the gradient of the penalty with respect to the parameters of the Gaussian.

4.3.2 Zernike parametrization

The most common way to parametrize aberrations is with a Zernike expansion [54],

$$\phi_k = \sum_{j=1}^{J} \alpha_j Z_j \tag{4.13}$$

where Z_j is the jth Zernike function (using a single-indexing scheme [55]) and α_j is the coefficient for the jth Zernike function.

The partial derivative of ϕ_k with respect to α_j is simply

$$\frac{\partial \phi_k}{\partial \alpha_j} = Z_j. \tag{4.14}$$

4.3.3 Biharmonic parametrization

An attractive alternative to these phenomenological parametrizations is to consider a direct physical model of the deformable mirror, i.e., parametrizing ϕ in terms of the shape of the surface of the mirror. In the general case, the alignment of the pupil with respect to the DM is unknown, and in any event the projection of the pupil onto the DM surface is "compressed" along one axis due to the angle of reflection off the surface (Fig. 4.3). These statements may be encapsulated as

$$\phi_k(\mathbf{u}) = \psi_k(\mathbf{A}\mathbf{u} + \boldsymbol{\xi}_0), \tag{4.15}$$

where the matrix $\mathbf{A}$ and offset $\boldsymbol{\xi}_0$ correspond to a "rigid body deformation" of the pupil, and $\psi_k(\boldsymbol{\xi})$ is effectively the mirror shape represented in two-dimensional coordinates $\boldsymbol{\xi}$ in the plane of the mirror. This representation thus casts the problem as fundamentally a rigid registration problem, but with respect to pupil coordinates (phase) rather than a registration of two observed images. $\mathbf{A}$ needs to allow rotation and scaling but not shearing ($\mathbf{A} = \mathbf{R}\mathbf{S}\mathbf{R}^T$ where $\mathbf{R}$ is a rotation matrix and $\mathbf{S}$ is diagonal), and thus is a generic 2×2 symmetric matrix

$$\mathbf{A} = \begin{pmatrix} a_1 & a_2 \\ a_2 & a_3 \end{pmatrix}. \tag{4.16}$$

After fitting, the rotation angle and scaling diagonals may be extracted from a singular value decomposition of $\mathbf{A}$; in particular, the absolute value of the ratio of the diagonals of $\mathbf{S}$ should be equal to the cosine of the angle of reflection off the mirror surface.

The form of ψ depends on the DM. For the Mirao 52-d, the linearity with respect to perturbation of individual actuators (see Fig. 4.6) suggests a model

$$\psi_k(\boldsymbol{\xi}) = \sum_i (m_i v_{ki} + \zeta_i) b_i(\boldsymbol{\xi}), \tag{4.17}$$

where v_{ki} is the control voltage applied to the ith actuator in the kth diversity image, m_i and ζ_i are the slope and offset for this actuator, respectively, and $b_i(\boldsymbol{\xi})$ describes the shape of the surface induced by applying "unit" voltage to the ith actuator. b_i encapsulates the physics of the device, and in this case the necessary details (equation of motion and boundary conditions) are not publicly disclosed by the manufacturer. However, because this mirror is constructed from an elastic membrane, we postulate that the membrane energy is a function of the curvature, i.e.,

$$E_{\text{membrane}}[b] \propto \int \mathrm{d}\boldsymbol{\xi}\, (\nabla^2 b)^2, \tag{4.18}$$

where ∇^2 is the Laplacian with respect to coordinates $\boldsymbol{\xi}$. Hence b satisfies the fourth-order *biharmonic equation*

$$(\nabla^2)^2 b = 0. \tag{4.19}$$

This equation of motion needs to be supplemented by the boundary conditions, for which we will assume that the membrane is clamped at some radius R, and that this clamp sets both the membrane height and slope to zero on the boundary ($b = 0$ and $\hat{\mathbf{r}} \cdot \nabla b = 0$ on the boundary, where $\hat{\mathbf{r}}$ is the unit radial vector). Consequently, application of a "unit" force at point $\mathbf{c}$ will induce a (normalized) displacement given by the Green's function [56],

$$b(\tilde{\boldsymbol{\xi}}|\tilde{\mathbf{c}}) = \frac{1}{R^2}|\tilde{\boldsymbol{\xi}} - \tilde{\mathbf{c}}|^2 \log\left(\frac{R^2|\tilde{\boldsymbol{\xi}} - \tilde{\mathbf{c}}|^2}{|R^2 - \tilde{\mathbf{c}}^\dagger\tilde{\boldsymbol{\xi}}|^2}\right) + \frac{1}{R^4}(R^2 - |\tilde{\boldsymbol{\xi}}|^2)(R^2 - |\tilde{\mathbf{c}}|^2), \tag{4.20}$$

where $\tilde{\boldsymbol{\xi}} = \xi_x + \imath\xi_y$ is the complex number formed from the $x-$ and $y-$coordinates of

$\boldsymbol{\xi}$ and similarly for $\tilde{\mathbf{c}}$. For each actuator, the corresponding $\mathbf{c}_i$ is specified from the known grid arrangement of the actuators (Fig. 4.4a).

The advantage of this approach is in the comparatively small number of parameters required: rather than needing the first five orders of Zernike functions (20 Zernike coefficients for each actuator, a total of 1040 parameters), here each actuator is represented by only two parameters, m_i and ζ_i. Indeed, in a first-pass optimization one may take $\zeta_i = 0$ and use a common value $m_i = m$ for all actuators (assuming that each electromagnet produces similar force), and thus all 52 actuators contribute just a single parameter, m. One also must fit R and the rigid-deformation parameters $\mathbf{A}$ and $\boldsymbol{\xi}_0$, and for calibration with a single bead we also modify Eq. (4.15) to allow a defocus,

$$\phi_k(\mathbf{u}) = \psi_k(\mathbf{A}\mathbf{u} + \boldsymbol{\xi}_0) + \alpha(2\mathbf{u}^2 - 1), \tag{4.21}$$

to include the possibility that the bead is slightly above or below the focal plane (which may not be readily detectable in the "mirror flat" condition but can nevertheless have a substantial impact on the aberrated images). Together, these contribute an additional 7 parameters. Consequently, this approach requires a total of either 8 or 110 parameters, depending upon whether one requires a susceptibility and offset (m_i and ζ_i) for each actuator.

Optimization of these parameters greatly benefits from an analytic calculation of the gradients; for reasons of space we do not present explicit formulas, but their derivation is entirely straightforward (if slightly tedious) from Eqs. (4.21) and (4.20). The initial guess for the 8-parameter model is supplied by the user with the help of a custom GUI program, to ensure that the pupil registration parameters do not get trapped in a local minimum far from the optimum solution.

4.4 DM calibration

In order to apply AO to OCPI microscopy, a DM needs to be placed in the light path of the microscope; the DM has a number of control signals, and the effect of these control signals on the aberration structure must be calibrated. SHWFS or interferometry-based systems can be used to calibrate a DM, but that would entail adding a new optical system to the microscope. Since this problem is conceptually equivalent to the wavefront sensing needed for AO, PDI algorithms should also be useful for calibration [57] [Fig. 4.3(b)]. Below we describe the calibration of a DM in an OCPI microscopy setting using PDI.

4.4.1 Optical layout for DM calibration

In OCPI microscopy the optics needed to form a light sheet are rigidly coupled to the objective, illuminating just the focal place of the objective [20] [Fig. 4.3(a)]. To permit imaging of extended neural tissues, we tilt the objective (with the coupled laser sheet) from the traditional face-on imaging to an angle of 30 degrees. This minimizes the distance through tissue traveled by both the excitation light and the emitted light.

To correct the resulting aberrations, a DM (Mirao 52-d, Imagine Optics) is placed behind the back aperture of the microscope objective (20× infinity-corrected, 0.5 NA, water immersion, Olympus). The light collected by the objective is reflected off the DM before it is focussed onto a camera (GRAS-14S5M, Point Grey) by a 200 mm tube lens (Edmund Optics) [Fig. 4.3(a)].

The Mirao 52-d is a 52-actuator DM [58], with the actuators encompassing a circular pupil of 15 mm diameter [Fig. 4.4(a)]. The reflective surface is made of a silver-coated sheet with an array of permanent magnets on the back side; to change the shape of the mirror, one applies force by controlling the current in coils placed

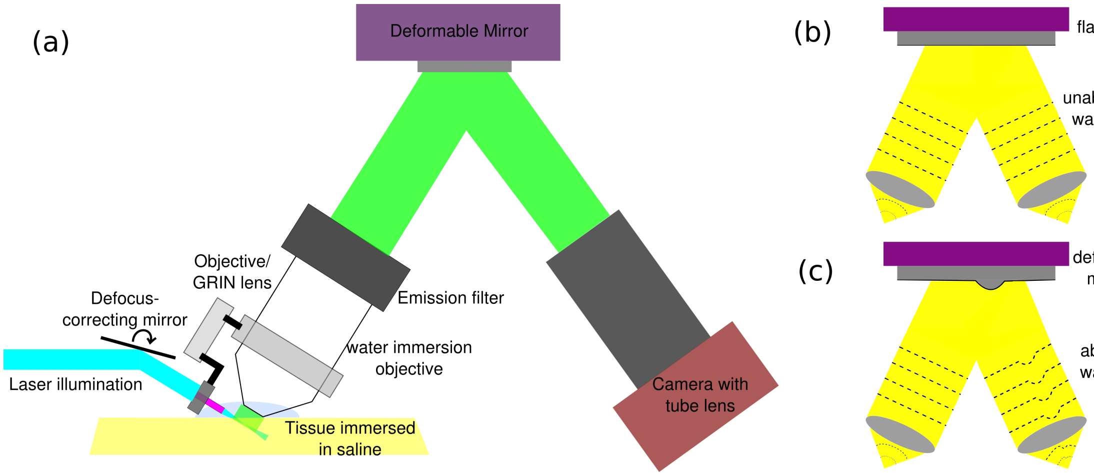

Figure 4.3: Optical layout for DM calibration: **(a)** A DM is placed behind the back aperture of the objective. The light reflected off the DM is imaged onto a camera. **(b,c)** Schematic of wavefront aberration when the DM is "flat" and when one actuator on the DM is moved.

opposite each magnet [Fig. 4.4(b)].

4.4.2 Experiments

We imaged a 0.2 μm (diffraction limited) fluorescent bead embedded at the surface of a flat slab of poly-dimethylsiloxane (PDMS, Dow Corning, DC 184-A and DC 184-B with a weight ratio of 10:1). Each actuator was manipulated by applying voltages ranging from -0.1 V to 0.1 V with 0.01 V steps (all the other actuators were maintained at 0 V), and an image was collected at each step. Thus, we obtained 21 images for each of the 52 actuators, for a total of 1092 images. In Fig. 4.5 we show the images obtained by moving one of the actuators (actuator 22, see Fig. 4.4(a)) from -0.09 V to 0.1 V .

4.4.3 Results

Zernike parametrization Each actuator was manipulated separately, and the resulting aberration parameterized using the first five orders of Zernike functions (20 parameters in total per actuator). We found that the calculated estimate of ϕ did not improve when larger number of Zernike functions were used. In the optimization, the initial guess for these Zernike coefficients was created by first fitting a Gaussian model of the aberration, which (having far fewer parameters) allowed for rapid and relatively exhaustive search. In Fig. 4.6a we show that each of the Zernike parameters varies approximately linearly with voltage; the slope of the relationship is plotted as a phase plot in Fig. 4.6b. The “single-hump” peak reflects the movement of an actuator at the location of the peak. In Fig. 4.7 we demonstrate the accuracy of the calibration of one actuator (number 22, Fig. 4.4a) by showing the measured and calculated images for images obtained when different voltages are applied to this actuator.

Each actuator was calibrated individually with an identical voltage series comprising of 21 images. One observes that the resulting aberrations define a grid structure

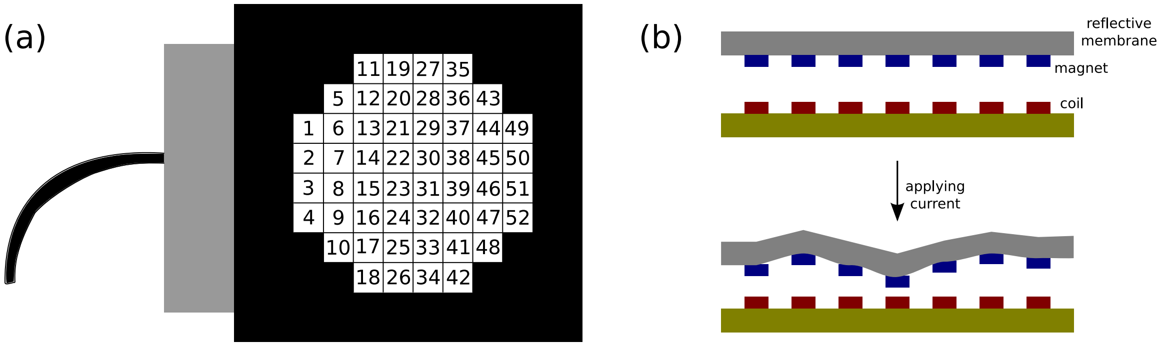

Figure 4.4: Mirao 52-d. **(a)** A schematic image of the Mirao 52-d deformable mirror. The 52 actuators encompass a pupil of diameter 15 mm. The numbering of the actuators presented here is used in rest of the paper. **(b)** The mirror is made of a sheet of mirror with voltage-controlled magnetic actuators on the back surface of the mirror.

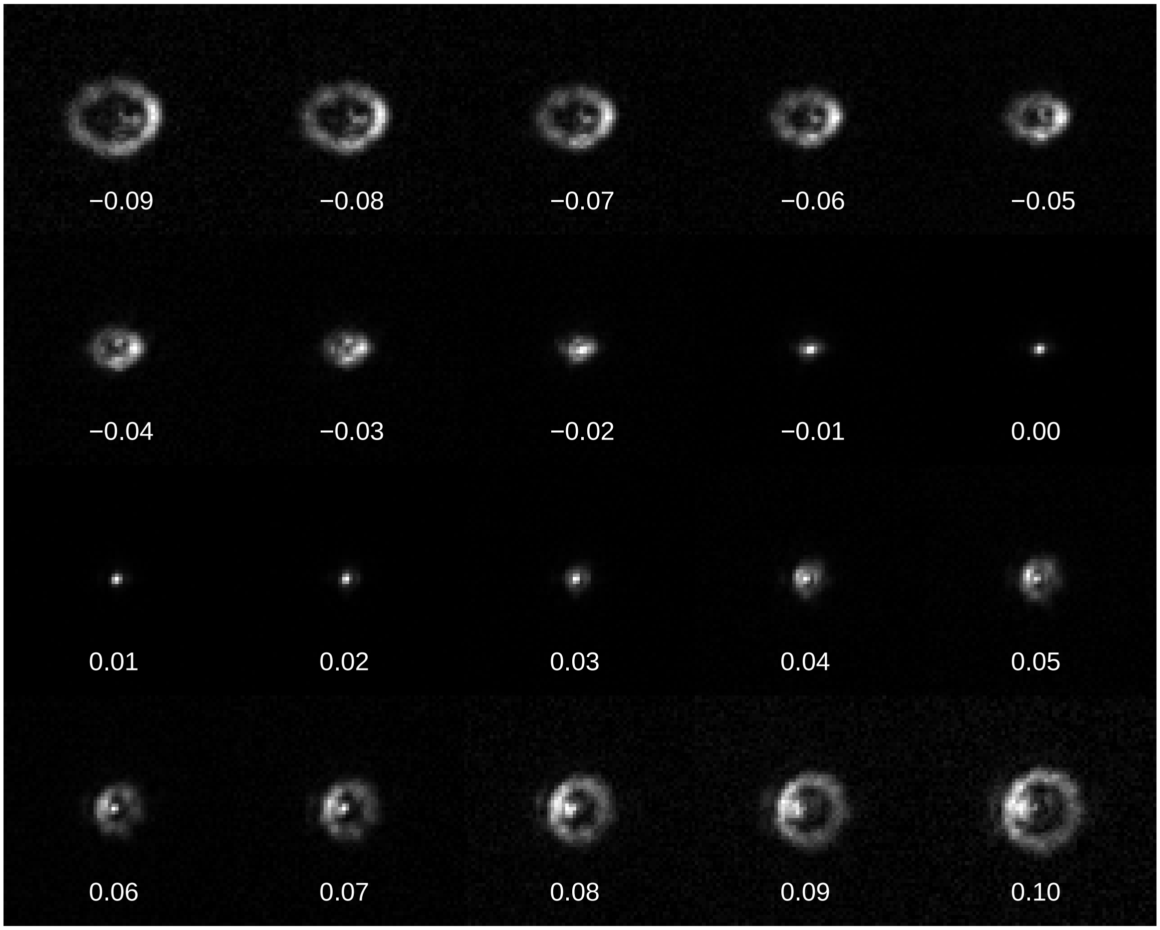

Figure 4.5: The images of a 0.2 μm bead obtained after applying -0.09 V to 0.1 V to actuator 22 (see Fig. 4.4a for the location of the actuator). Each image is 64×64 pixels, with 1 pixel = 0.29 μm×0.29 μm. (All consequent bead images have the same dimensions).

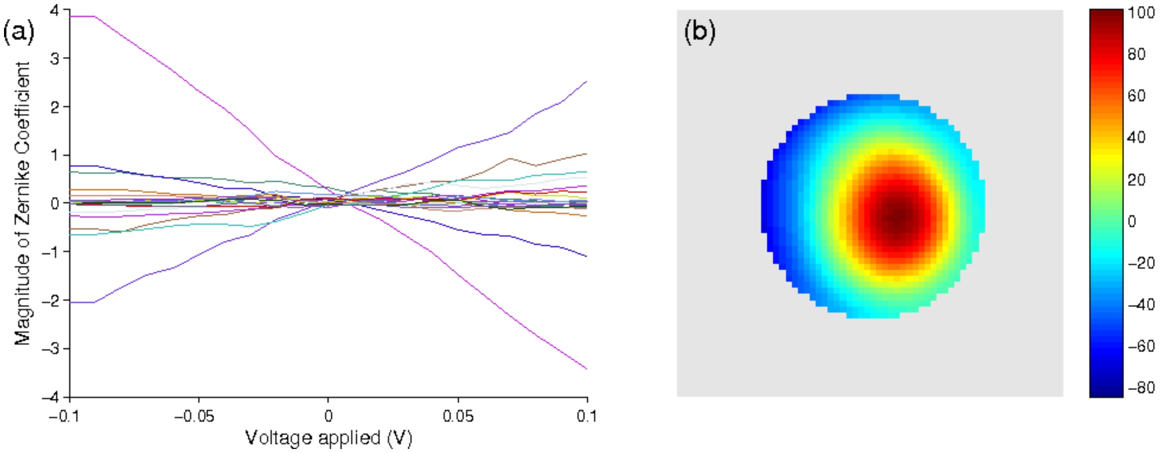

Figure 4.6: Actuator 22 calibration: **(a)** Each of the 20 Zernike coefficients varies nearly linearly with voltage. The slope of the relationship is plotted as a phase plot in (b). **(b)** The "single-hump" peak of the phase plate depicts the movement of the actuator at the location of the peak (colorbar units = radians/V).

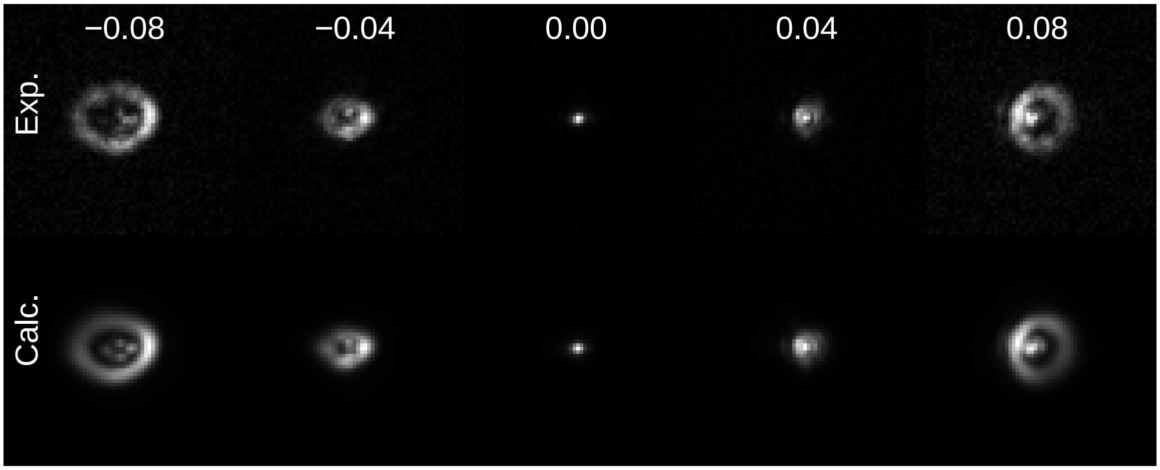

Figure 4.7: The experimentally obtained **(top)** and calculated **(bottom)** images of a bead when different voltages are applied to actuator 22. The calculated images were obtained from the calculated estimate of ϕ using Zernike parametrization.

reminiscent, as one might expect, of the underlying grid of actuators (Fig. 4.8). To visualize the alignment between Fig. 4.4(a) and Fig. 4.8 one needs to reflect the DM actuator grid across the vertical.

In Fig. 4.6a we can see that the Zernike coefficients have a non-zero component at zero applied voltage. This yields an estimate of the baseline aberrations of the system, which include any imperfections in the system optics (which tend to be small) and deviations in the mirror shape from nominally flat (which can be more substantial). In Fig. 4.9a we show that the zero-offsets measured for each of the actuators have similar values even though they were measured independently. By calculating the means of the offsets for each of the 20 Zernike coefficients, we estimated the shape of the mirror when it is "flat" (Fig. 4.9b). The flatness of the mirror can be improved by supplying an array of offset voltages $\mathbf{v}_0$, with

$$\mathbf{v}_0 = -\mathbf{M}^{+}\mathbf{Z}_0, \tag{4.22}$$

where $\mathbf{Z}_0$ is the vector of Zernike coefficients in the nominally-flat condition, $\mathbf{M}$ is the matrix formed from the slope of the Zernike coefficients for each actuator [Fig. 4.6a], and $^{+}$ denotes the Moore-Penrose pseudoinverse.

Physical membrane based model of DM We performed the 8 parameter and 110 parameter biharmonic parametrization of the aberrations caused by individual actuators. The eight parameter model was obtained by using all the 21×52 images to fit the parameters $\mathbf{A}$, $\boldsymbol{\xi}_0$, α, and a single value of m for all actuators, while setting $\zeta = 0$. The resulting phases for each of the actuators are shown in Fig. 4.10.

To obtain the actuator phases for the 110 parameter model, $\mathbf{A}$, $\boldsymbol{\xi}_0$ and α were held constant while m and ζ were fit separately for each actuator. In Fig. 4.11 we show the value of m_i obtained for each of the actuators. The m_i values appear to be dependent on the location of the corresponding actuator—suggesting an underlying

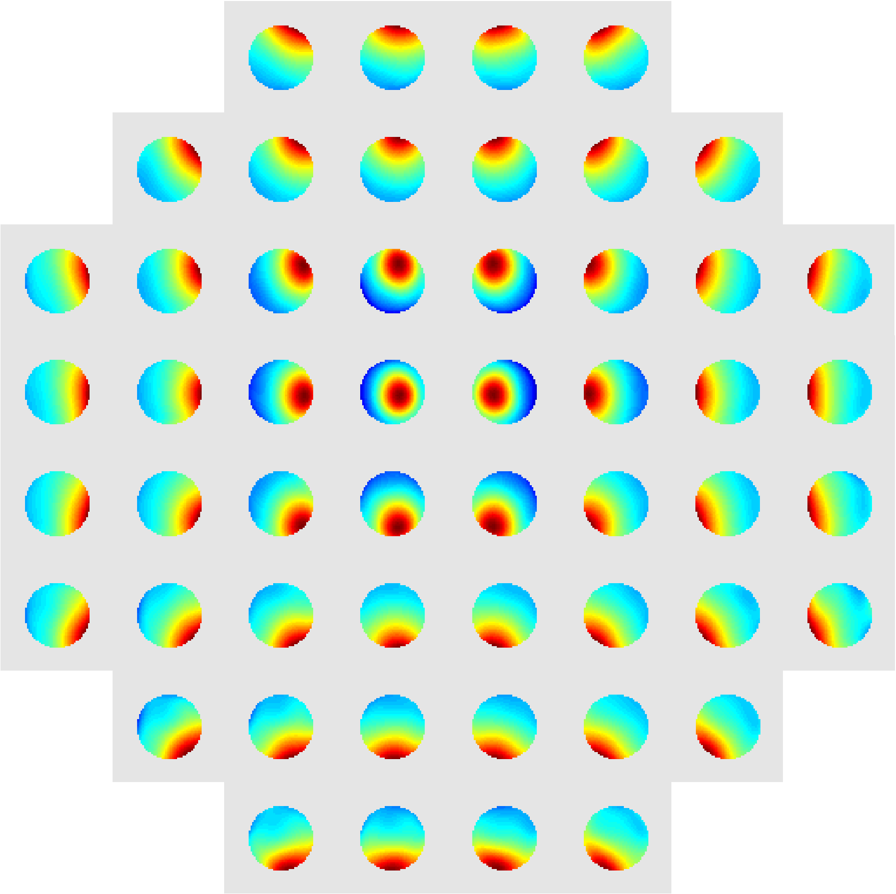

Figure 4.8: The phase plots obtained for all 52 actuators using Zernike parametrization. Each of the phase plots is scaled independently to demonstrate the underlying differences.

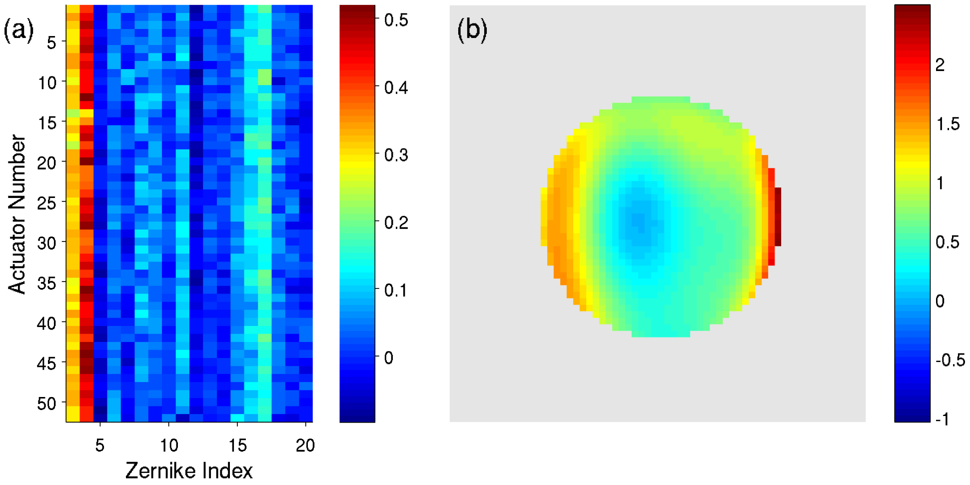

Figure 4.9: DM "flat" **(a)** Magnitude of Zernike coefficients for each of the actuators at zero applied voltage obtained from optimization of each actuator independently; note the consistency of the fitting result. The first two Zernike coefficients contribute to overall tip and tilt of the PSF, and are not shown in this figure. **(b)** The phase present at zero applied voltage (colorbar units = radians).

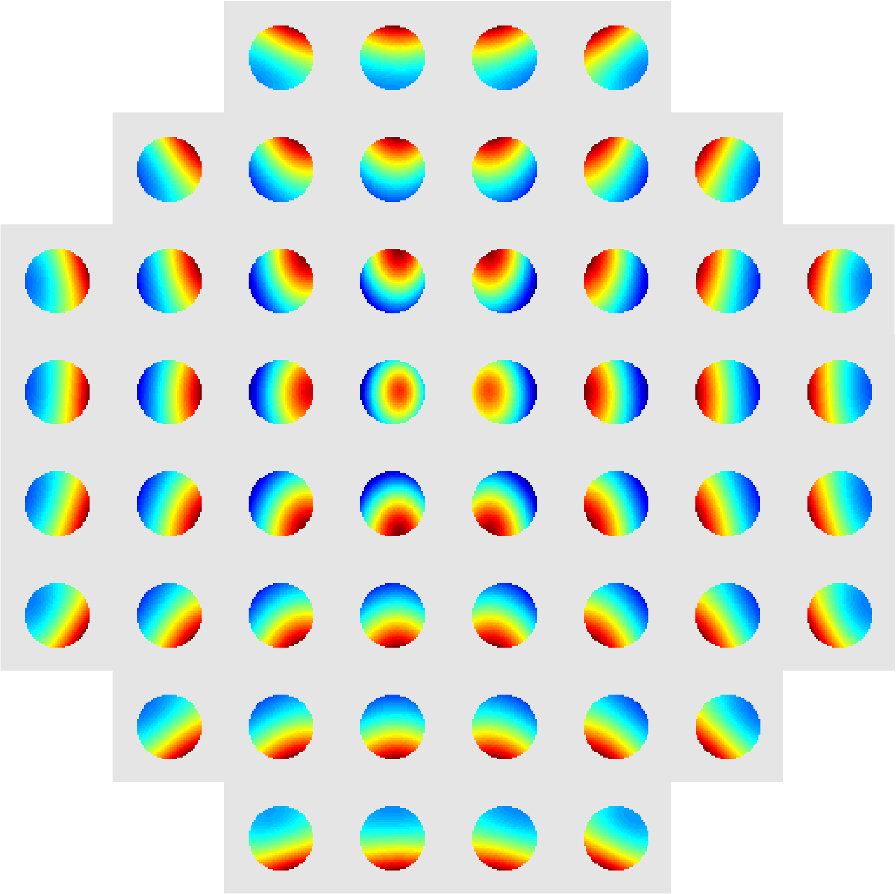

Figure 4.10: The phase plot obtained for all 52 actuators using the 8 parameter biharmonic parametrization. Each of the phase plots is scaled independently to demonstrate the underlying differences.

asymmetry in the DM.

In Fig. 4.12 we show the experimental and calculated images (using biharmonic parametrization) obtained when voltage is applied to actuator 22. The quality of the agreement is lower than observed for the Zernike fit (Fig. 4.7). Therefore, henceforth we adopted the Zernike parametrization.

Testing the Zernike model calibration The calibration was performed individually for each actuator, yet for AO one must manipulate all of the actuators simultaneously to compensate for arbitrary aberrations. To test whether the calibration procedure suffices in this circumstance, we specified random voltages for all the actuators in the DM and measured the resulting images of beads. Using the calibration data, we estimated the total wavefront aberration as the linear sum of aberrations caused by individual actuators. This predicted aberration was then used to calculate the theoretical PSF to obtain a calculated estimate of the image. A schematic of the procedure is shown in Fig. 4.13 .

To explore whether the deviation from nominal "flatness" requires compensation, we considered the random voltage test both before and after correcting for the true mirror flatness (Fig. 4.14). The calculated images are modestly improved by including the flatness correction.

We performed such a "random-voltage" test using 50 different sets of random voltages, with all of them leading to good agreement between the measured and calculated images (Fig. 4.14). Thus we conclude that the Zernike expansion yields an accurate model of the mirror.

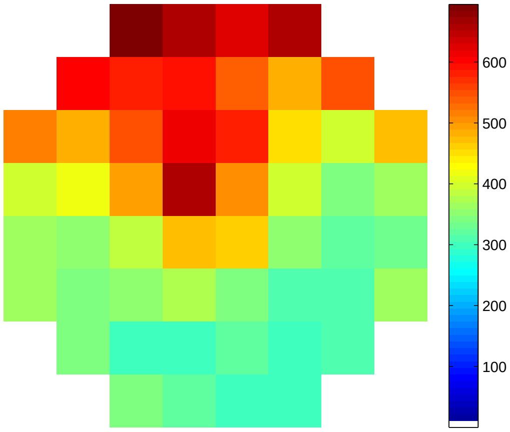

Figure 4.11: The values of m_i obtained for each of the actuators after a 110 parameter biharmonic parametrization of ϕ. colorbar units = radians/V.

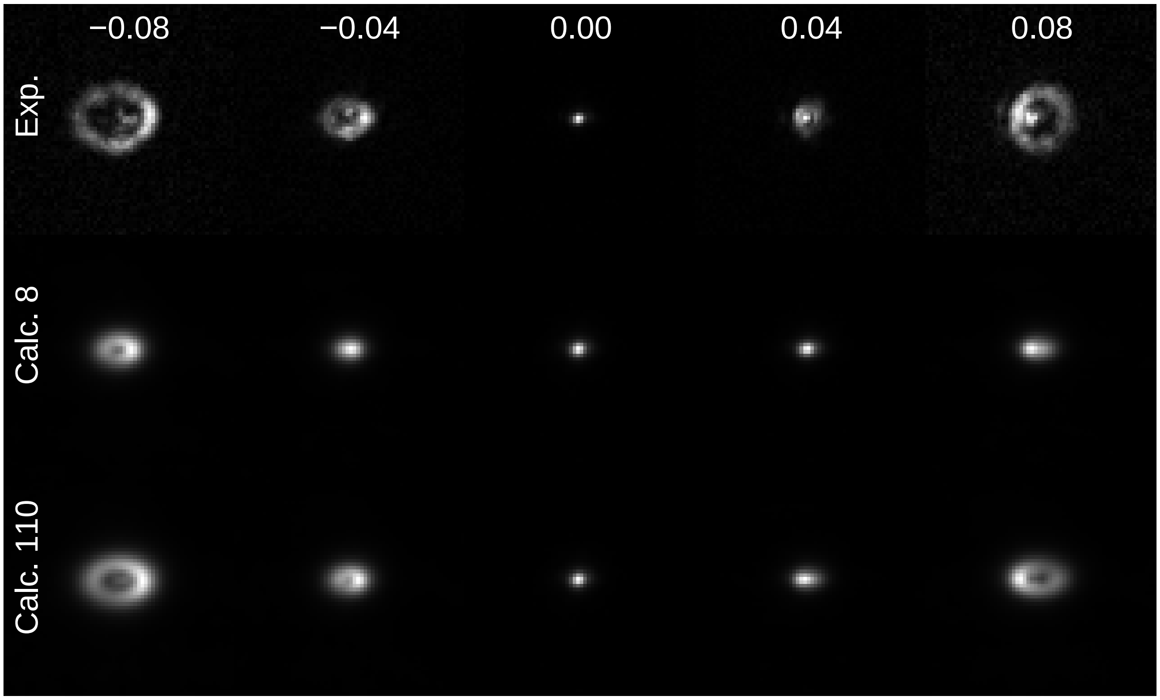

Figure 4.12: The experimentally obtained **(top)** and calculated **(middle, bottom)** images of a bead when different voltages are applied to actuator 22. The calculated images were obtained from the calculated estimate of ϕ using biharmonic parametrization with 8 (middle) and 110 (bottom) parameters.

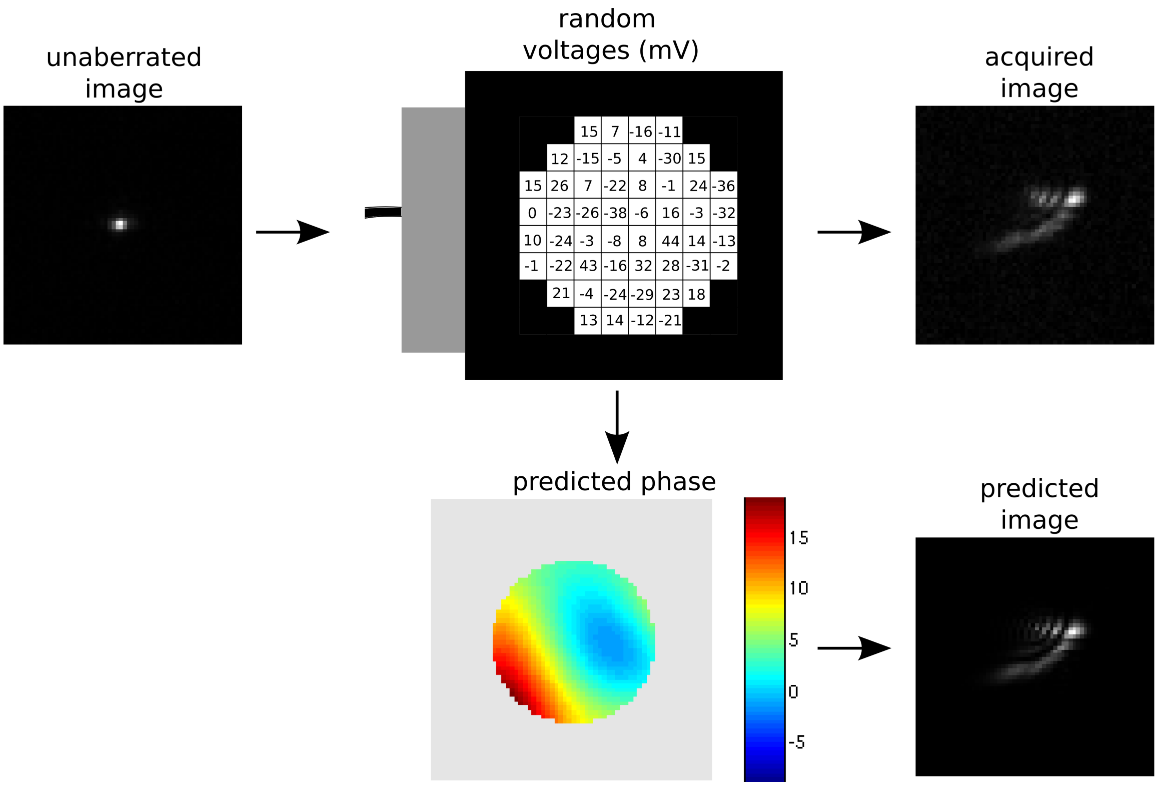

		15	7	-16	-11		
	12	-15	-5	4	-30	15	
15	26	7	-22	8	-1	24	-36
0	-23	-26	-38	-6	16	-3	-32
10	-24	-3	-8	8	44	14	-13
-1	-22	43	-16	32	28	-31	-2
	21	-4	-24	-29	23	18	
		13	14	-12	-21		

Figure 4.13: A random set of voltages are applied to the DM to produce the acquired image. The Zernike parametrization based calibration of the DM is used to calculate the phase produced by the set of random voltages (colorbar units = radians). The calculated phase is then used to create the calculated image. The agreement between the acquired and calculated images demonstrates the accuracy of the calibration of the DM.

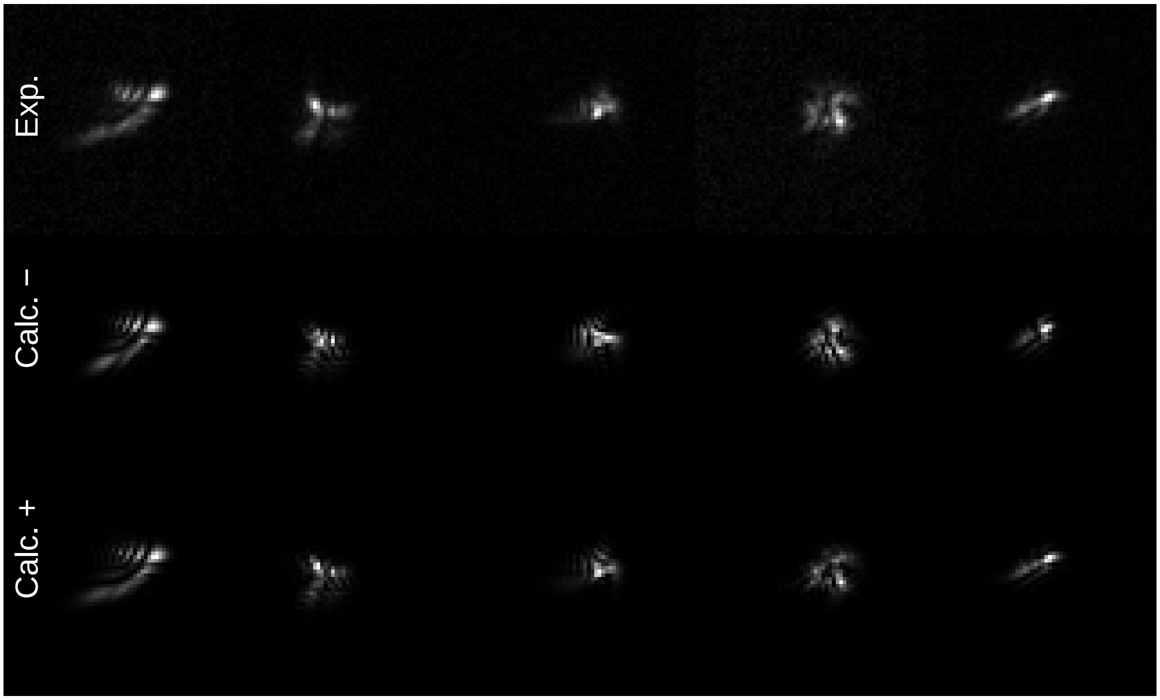

Figure 4.14: Sets of random voltages were applied to the DM to obtain the experimental (Exp.) images. Zernike based calibration of the DM was used without (Calc.-) and with (Calc.+) offset correction to obtain the calculated images for the given set of random voltages. Each column represents images obtained from a different set of random voltages.

4.5 Preliminary application of AO for OCPI microscopy

In order to pursue PDI, I implemented an AO-OCPI system (see Fig. 4.15, Fig. 4.16). In the AO-OCPI microscope, a beam splitter was placed at the back aperture of a microscope objective. One of the resultant paths is aberrated by a deformable mirror (Mirao 52D) before it is imaged onto a camera. The second pathway is imaged onto a camera unaberrated. This setup allows for obtaining two images — one DM-unaberrated (in-focus) image and one DM-aberrated (can be tuned to apply a defocus aberration) image. The two images can be used to calculate the wavefront aberration using PDI algorithms.

In Fig. 4.17 we show that the image of an aberrated bead in sylgard can be improved upon by using PDI and AO. A fluorescent bead was embedded in sylgard ($n = 1.4$). The refractive index mismatch between sylgard and immersion fluid (water, $n = 1.33$) produces wavefront aberrations while imaging using OCPI microscopy. Two images of the bead were obtained — one in-focus and one defocused. The two images were used to calculate the wavefront aberration in the imaging using PDI algorithms (Fig. 4.15B). The wavefront aberration was corrected using the DM to obtain a higher resolution image of the fluorescent bead (Fig. 4.15C).

Applying 2D PDI algorithms to 3D tissue is unfortunately not trivial. A “defocused” image of a 3D object includes a previously out-of-focus portion of the object now newly in-focus. In order to compensate for this phenomenon further theoretical modifications need to be made to PDI algorithms. But one can “cheat” by analytically calculating the aberration present in tilted imaging; one can then produce the appropriate DM shaped needed to correct for the calculated aberration. Fig. 4.18 shows that such an approach leads to moderate improvements in image quality. But major gains in image quality will be achieved only by implementing 3D PDI algorithms.

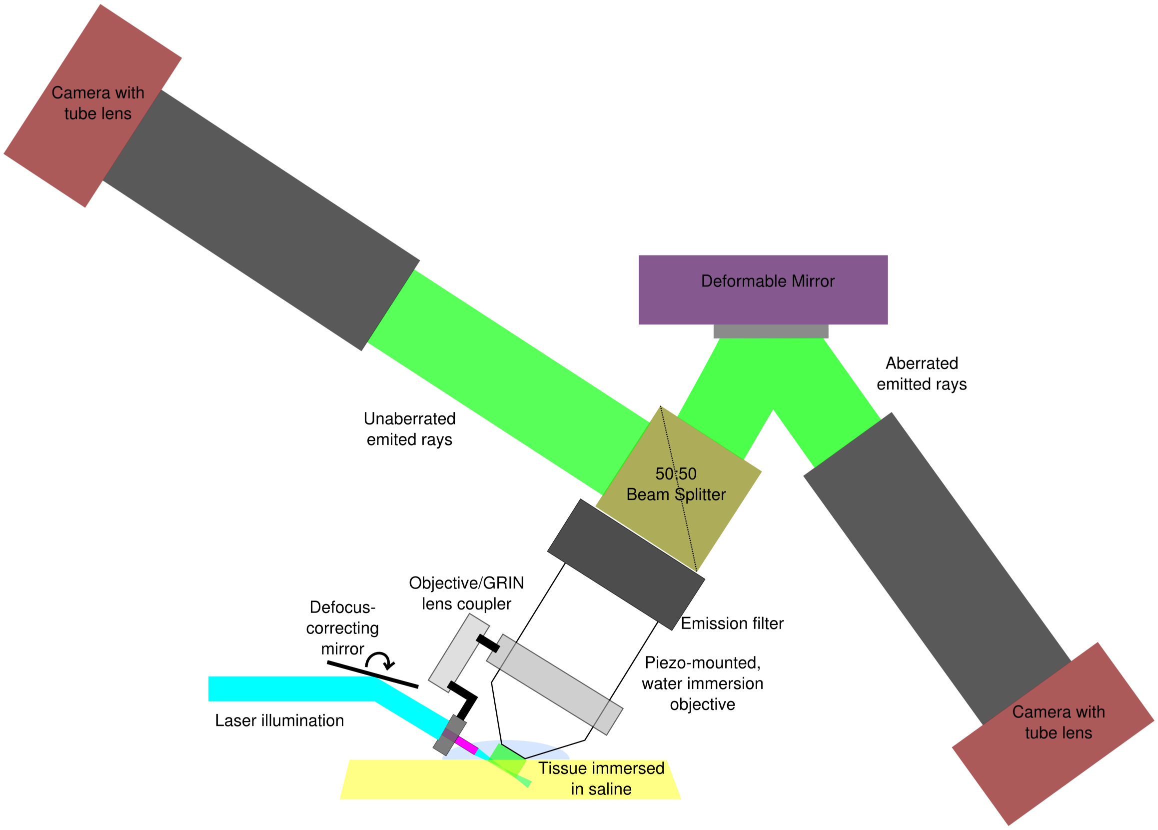

Figure 4.15: In AO-OCPI we place a beam splitter at the back aperture of a microscope objective. One of the resultant paths is aberrated by a deformable mirror (Mirao 52D) before it is imaged onto a camera. The second pathway is imaged onto a camera unaberrated. This setup allows for obtaining two images — one in-focus (DM-unaberrated) image and one out-of-focus (DM-aberrated) image. The two images can be used to calculate the wavefront aberration using PDI algorithms.

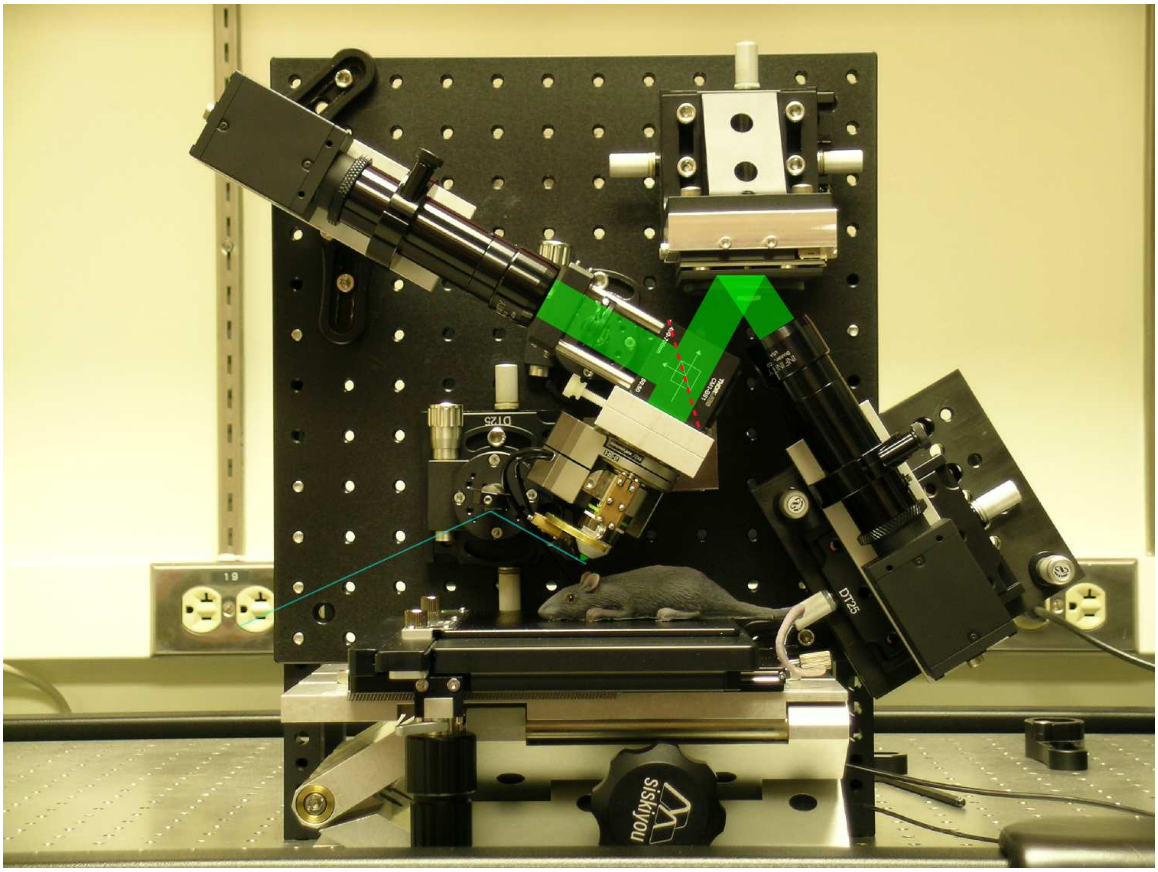

Figure 4.16: Picture of AO-OCPI

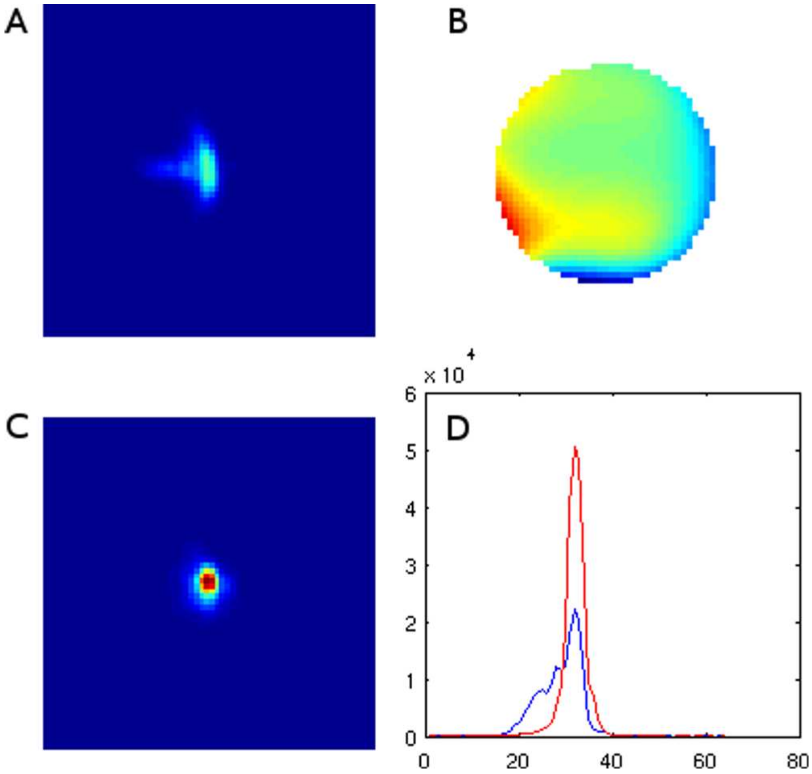

Figure 4.17: Proof of principle of wavefront aberration correction using adaptive optics: **(A)** Image of diffraction limited 200 nm bead in sylgard (polydimethylsiloxane, a transparent silicone, refractive index $n = 1.40$). We can clearly see aberrations in the bead image (1 pixel = 0.25 μm). **(B)** The calculated DM shape which can compensate for the aberration seen in (A) (colorbar units = radians). **(C)** The image of the same bead after aberration correction 1 pixel = 0.25 μm). **(D)** A plot of the middle row from A and C showing an increase in sharpness of the bead after aberration correction (y axis = pixel intensity, x axis = pixel number).

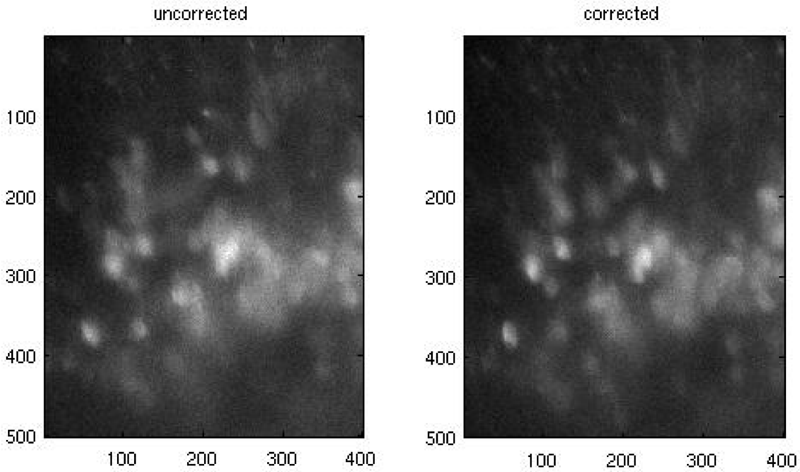

Figure 4.18: Proof of principle of wavefront aberration correction using adaptive optics in tissue: (Left) Image of fluorescent labeled VNO without aberration correction. (Right) A model of tissue dependent aberration was used to shape the DM. A modest improvement in image sharpness can be seen after the wavefront correction. 1 pixel $= 0.71\,\mu$m.

Chapter 5

Perspectives on OCPI microscopy

5.1 Scattering as a limitation for imaging deep

Biological tissue scatters light. Once aberrations due to tilted imaging are corrected using adaptive optics, scattering becomes the next limitation for imaging deep into tissue. One solution to imaging deeper into tissue is to use longer wavelength excitation light; longer wavelength excitation/emission undergoes lower scattering in biological systems [11]. This approach is possible as of today — but lack of calcium sensitive dyes in the infra-red (IR) region makes the approach not applicable for neuronal activity imaging.

An alternate possibility is to apply two-photon excitation to create a line and then scan the line[1]. This approach might lead to lower scattering because the excitation uses an IR laser; in biological samples, IR light has lower scattering than visible light.

There have been other approaches to decrease scattering. A potential approach pioneered by Dodt and colleagues uses refractive index matching to decrease scattering [34]. Dodt *et al.* apply a clearing solution of 1 part benzyl alcohol in 2 parts benzyl benzoate to tissue to produce uniform refractive index through out the tissue; this allowed for low scattering, high contrast imaging using LSFM. But such an approach is

---

[1] similar to [38], but with 2-photon excitation

only applicable in fixed tissue and thus not applicable to live cell imaging. Researchers are actively working on producing other chemicals which can decrease scattering in live tissue. One promising chemical is iodixanol, a X-ray contrast agents, which might allow for refractive index matching in physiological conditions[2].

5.2 Limitations on speed of OCPI

5.2.1 Two-Dimensional imaging

The ultimate limit in fluorescence microscopy comes from the excitation/emission cycle of a fluorophore. For a SNR of 100, one needs a pixel dwell time of ∼1 μsec [20]. Due to parallelization of acquisition of pixels in OCPI microcopy, in theory, OCPI microscopy can image at ∼1 μsec per frame. This limit has not been achieved due camera and hardware limitations; but as the cameras and computer hardware technology improve one can start going as much 10000× faster than laser scanning microscopes. At such speeds the laser power becomes the next limitation; one needs high enough power density to collect enough photons in limited time for high-speed/high-SNR imaging. But higher laser intensity leads to faster photobleaching and phototoxicity (i.e. shorter experiments). So the ultimate speed limitation of 2D OCPI imaging will be dependent on the trade-off between the laser intensity and the required duration of the experiment.

5.2.2 Three-Dimensional imaging

To pursue 3D imaging one needs to scan the light sheet. First generation OCPI microscope image's a 200 μm thick volume in 2 sec. This speed is sufficient for imaging neuronal activity in the Vomeronasal organ[3] (VNO). But for faster 3D imaging, one

---

[2] Iodixanol has a refractive index close to tissue. Perfusing tissue with the contrast agent might allow for the tissue to decrease its refractive index inhomogeneity.

[3] In VNO experiments, the stimulus is applied for ∼30 sec and the activity is measured.

needs to move the piezo-electric positioner faster. As the piezo-electric technology improves one might be able to image volumes of $125\,\mu\text{m}\times 700\,\mu\text{m}\times 100\,\mu\text{m}$ at speeds as high as 100 Hz, allowing for true 3D imaging at speeds close to action potential (AP) resolution.

5.3 Future

Throughout this section I have discussed methods to improve imaging through improving the microscopy. But simultaneously, there have been huge improvements in the dyes available. The new version of GCaMP — GCaMP3 — is shown to have a 3 fold improved SNR over GCaMP2 [17]. Such high SNR dyes can readily be applied to OCPI microscopy and should lead to even faster imaging.

With technological improvements such as high-speed cameras, high-speed piezo-positioners and aberration correction, one can truly reach a stage where one can image a population of thousands of neurons at AP speeds. Thus OCPI microscopy is positioned to provide a whole new dimension to our understanding of neuronal circuits.

Chapter 6

Accessory Olfactory System

6.1 Olfaction in mammals

Mammals explore their environment using multiple sensory cues. One of the sensory cues is smell. The olfactory system's ability to detect changes in chemical environment is known to play a direct role in a number of behaviors [59].

There are two primary subdivisions in the olfactory system — the main olfactory system (MOS) and the accessory olfactory system (AOS) [60,61] (Fig. 6.1). The MOS consists of olfactory epithelium, main olfactory bulb and higher level cortical areas; it is thought to be primarily involved in sensing volatile chemicals. The AOS consists of vomeronasal epithelium, accessory olfactory bulb and higher level areas; it is thought to be involved in sensing non-volatile chemicals. These non-volatile chemicals, sometimes known as social odors, can produce characteristic behaviors in mammals [62]. For example, a male mouse produces either a fighting or a mounting response on sensing the chemicals in the urine [63]. The identity of individual chemicals leading to complex behavior has been an area of intense study [64–67].

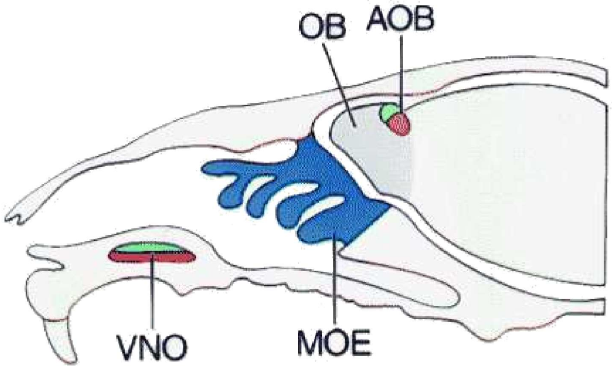

Figure 6.1: Anatomy of the olfactory systems in mice. Main olfactory systems consists of the olfactory epithelium, main olfactory bulb and higher order cortical areas. The accessory olfactory system consists of the vomeronasal organ, accessory olfactory bulb and higher order areas. From [68].

6.2 Accessory Olfactory System

6.2.1 Structure of Vomeronasal Organ

The primary sensory neurons of the AOS — vomeronasal sensory neurons (VSNs) — are found in the Vomeronasal organ (VNO). The VNO is located in a bony capsule dorsal to the palate (Fig. 6.2) [69]. In the VNO, VSNs are organized in a stratified layer; each of the VSNs sends a single dendrite to the surface of the epithelium. VSNs can express three major classes of ligand receptors, known as V1R, V2R, and FPR (formyl peptide receptors) [68, 70–75]. The receptors belong to the class of proteins called G-protein coupled receptors (GPCRs). V1R receptors are thought to consist of $\sim$200 receptor types, and the VSNs expressing them are known to reside in the apical layer of the VNO [76]; they have been shown to co-express GTP-binding protein subunit $G_{\alpha i2}$. V2R consist of $\sim$120 receptor types, and the VSNs expressing them are known to reside in the basal layer of the VNO [76, 77]; they have been shown to co-express GTP-binding protein subunit $G_{\alpha o}$. The recently identified FPRs are a total of 5 in number, and are shown to be expressed mostly in the apical layer [74,75].

In the presence of such a large repertoire of receptor types, each VSN is known to express one or very few types of receptors — leading to $\sim$300 different types of VSNs [62,77]. Such large diversity in VSNs is one of the main challenges in identifying individual cells responding to individual ligands.

6.2.2 AOS circuit

The axons from the VSNs terminate in glomerular structures in the accessory olfactory bulb (AOB). The axons synapse with excitatory mitral cells of the AOB. There is an added layer of spatial organization at this level: the V1R expressing neurons project to the anterior portion of the AOB and the V2R expressing neurons project to the posterior AOB. The purpose of such a segregation is still under active investigation

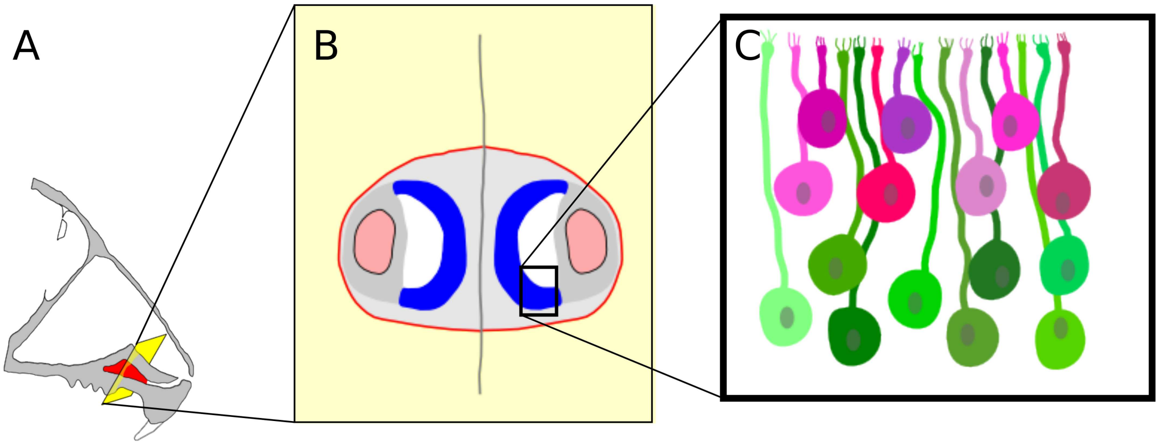

Figure 6.2: Schematic of VNO, the sensory organ of AOS. **(A)** A sagittal section of the nasal cavity of the mouse, VNO is shown in red. The coronal section (yellow plane) reveals the structure of the VNO. **(B)** Neuroepithelium (blue) containing VSNs and the blood vessel (pink). **(C)** A detailed view of the neuroepithelium. Each VSN sends a single dendrite to the tissue surface to detect chemical stimuli. Apical neurons (magenta hues) express members of the V1R family, while basal neurons (green hues) express V2R receptors.

[78–80].

AOB, in addition to mitral cells, contains inhibitory neurons which are known to help in processing information arriving through the VSNs [78, 80, 81]. ∼90% of the mitral cells project to the amygdala, and the rest are thought to project to the bed nucleus of stria terminalis (BSNT) (Fig. 6.3). The outputs of the amygdala are known to terminate in the hypothalamus; hypothalamus is one of the primary modulators of the behavioral status of mice. Thus AOS is a comparatively simple circuit; behavioral responses to individual ligands are made through very few intermediate processing steps.

6.3 Ligands for the VNO

A long-standing goal in the field of olfaction is to identify the specific ligands which lead to olfactory driven behaviors.

6.3.1 Natural ligands

Urine is known to be an important source of ligands to the VNO [62]. Mice can determine the sex and strain of another mouse based on cues present in urine[1]; the VNO is known to play a significant role in this behavior. The VSN responses to urine of different sexes and strains have been well characterized [20, 85–87].

We used OCPI microscopy with calcium imaging to measure VSN responses to male and female urine [20]. Urine was found to primarily activate the apical layer of the VNO, suggesting that urine contains chemicals which predominantly activate the V1R expressing VSNs [Fig. 6.4, Fig. 6.5].

---

[1] Mice can identify sex of the urine: Male mice are known to sing in the presence of female urine [83] and show aggressive behavior in the presence of male urine [66]. Female mice undergo estrous synchronization in the presence of other female urine. Female mice can form a memory of the strain of the male mouse it mated with; in the presence of a urine of a different strain, the female mouse terminates pregnancy [84].

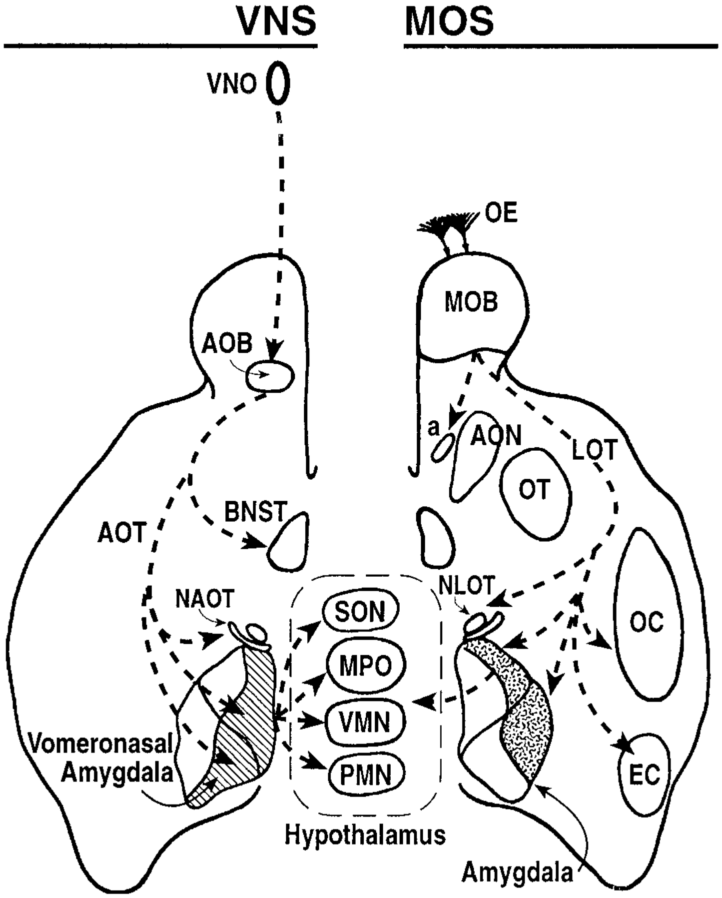

Figure 6.3: Circuit of the main and accessory olfactory systems: In particular, note that in AOS (left), the VNO projects to the AOB; AOB projects to vomeronasal amygdala and BNST. The amygdala in turn projects to the hypothalamus. From [82].

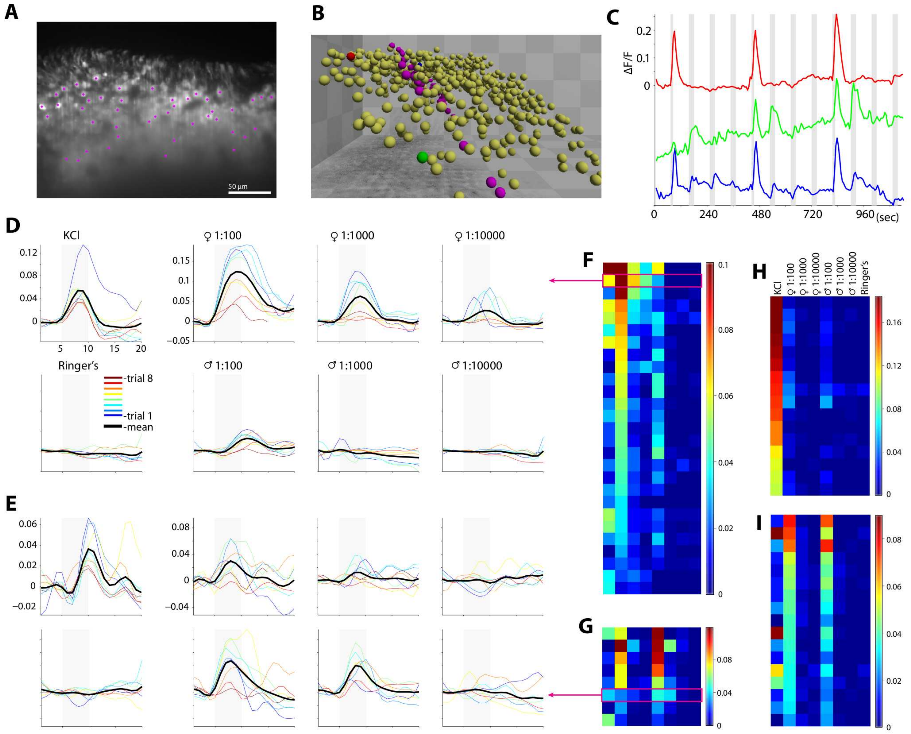

Figure 6.4: Probing responses to chemical stimuli of single VNO neurons by high-speed three-dimensional calcium imaging. **(A)** Intact VNO epithelium labeled with Oregon Green BAPTA-1; single optical section by planar illumination. Purple dots indicate position of regions of interest (ROIs) corresponding to single neurons. **(B)** Three-dimensional rendering of the ROI positions for the entire 40-image stack. ROIs drawn in purple were in the single section pictured in (A). Each checker is 100μ on a side. Sensory surface of the tissue is at the top. **(C)** Normalized fluorescence change vs. time for 3 ROIs indicated in red, green, and blue in panel (B). Vertical gray bars indicate periods of stimulation, a thrice-repeated cycle of high potassium (50mM), female mouse urine diluted 1:100 in Ringer's solution, 1:100 male mouse urine, and Ringer's solution (negative control). **(D and E)** Time course of fractional intensity changes induced by various stimuli for two selected neurons in a different preparation. Responses on single trials (thin lines) and the across-trial mean (thick black line) are shown. Period of stimulus delivery (valve opening) marked in gray. **(F-I)** Colorized activity profile for selected cells showing sensitivity or selectivity for particular stimulus. Rows correspond to individual neurons and columns represent different stimuli. Colorbars indicate fraction intensity change scale. **(F)** shows cells exhibiting high sensitivity (down to 1:10,000 fold diluted in Ringer's solution) and/or selectivity (up to 1:1000 selective over male) for female mouse urine. **(G)** presents cells exhibiting sensitivity (down to 1:1000 dilution) or selectivity (up to 1:10 over female) for male mouse urine. **(H)** presents cells showing maximum stimulated changes in fluorescence in response to 50mM KCl. **(I)** shows cells with large stimulated changes in response to urine from both sexes.

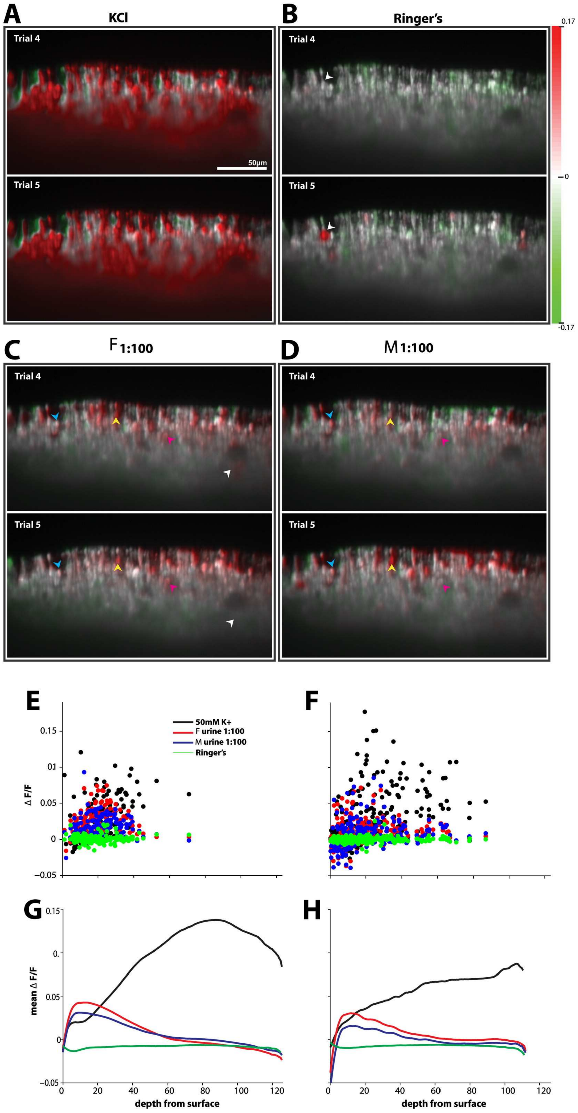

Figure 6.5: Imaging Reveals Patterned Responses to Pheromones in VNO: Images are color coded to represent the normalized fluorescence intensity change (ΔF/F) upon stimulation (colorbar, right). Shown are two sequential trials of (A) 50 mM KCl, (B) Ringer's solution, (C) 1:100 female mouse urine, and (D) 1:100 male mouse urine. White arrow marks cell exhibiting spontaneous activity not reproducible across trials; yellow arrows mark cells that appear relatively unselective for sex; blue and pink arrows mark cells with some preference for male or female mouse urine, respectively. Colorbar indicates magnitudes of fractional intensity changes. Scale bars, 50 μm. (E and F) ΔF/F versus depth for individual ROIs. Each neuron/stimulus combination marked with a single point; stimulus coded by the indicated color. (E) and (F) show the result for two different preparations. ΔF/F values represent averages over six trials. (G and H) ΔF/F averaged over all voxels of a given depth. Traces are averages of ten trials.

6.3.2 Sulfated Steroids

Nodari *et al.* have used chemical separation of female mouse urine to identify a novel class of ligands to the VNO — sulfated steroids [67] (Fig. 6.6). Sulfated compounds are shown to contribute ∼80% of the VSN activity due to female urine[2]. Such a large percent of activity attributed to the sulfated compounds suggests a vital role played by molecules. Sulfated steroids have been hypothesized to represent "true" signals of the internal functioning of the mouse — letting one mouse spy on another[3] [67,88,89].

The true test for a ligand to be characterized as a pheromone lies in proving (1) that a mouse can detect the ligand, and (2) that the ligand affects the mouse's behavior. In order to pursue that question, we performed mate choice experiments[4] (Fig. 6.7). In Fig. 6.7 we show the results of the experiment where Ringers (negative control) or corticosterone-21-sulfate (cort21S) was applied to one of the females. We found that when the male mouse had to choose between a Ringers painted female and a non-painted female, it was equally likely to choose either of them. But when the male mouse was made to choose between a cort21S painted female and a non-painted female, it pre-dominantly chose the non-painted female. This suggests that the male mouse detects cort21S and chooses to mate with the "non-stressed" female mouse. Further behavioral studies with different concentrations of cort21S might need to be performed to further quantify the results.

Meeks *et al.* have recently performed a more detailed study of the early processing

---

[2] BALB/c female urine

[3] For example, a female mouse might want to judge to "fitness" of the male mouse before it mates. If the female mouse is detecting a compound X in the urine, then it is to the advantage of the male mouse to artificially increase its level of X. Under such circumstances, the value of detecting X will decrease. But if the compound X is inherently involved in regular metabolism of the mouse, and is very hard to increase artificially, then the detection of compound X will be valuable for the female mouse. This compound X can then be called the "true" signal of fitness. Sulfated steroids are ideally placed to play this role of "true" signals. Sulfated steroids are intimately involved in the metabolism of sex steroids such as testosterone and stress steroids such as corticosterone.

[4] In a typical mate choice experiment, two female mice were placed in a cage. One of the mouse was painted with a stimulus at the ano-genital regions — the other female mouse remains unpainted. A male mouse was introduced into the cage, and the preference of the male for each of the females was scored.

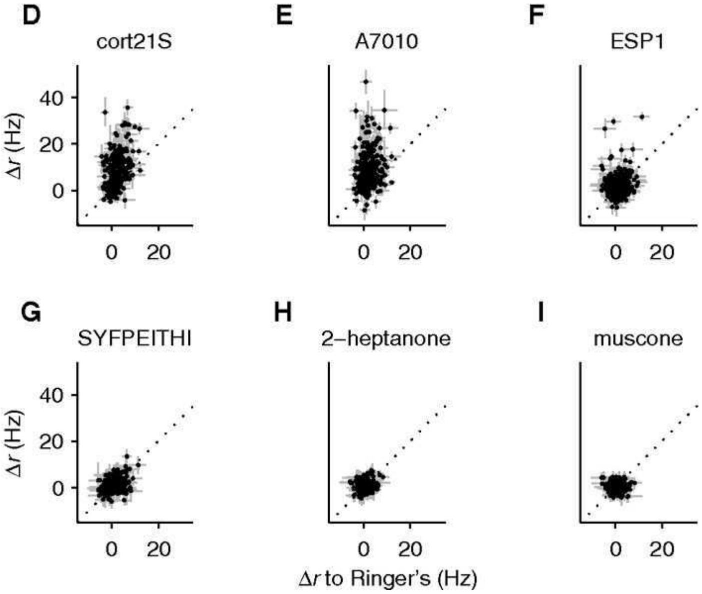

Figure 6.6: Neural responses to six compounds: cort21S (D), A7010 (E), ESP1 (F), SYFPEITHI (G), 2-heptanone (H), and muscone. The data show robust VSN activity in response to the sulfated steroids: cort21S and A7010. The axes represent the amount of increase in firing rate on presentation of the given stimulus. From [67].

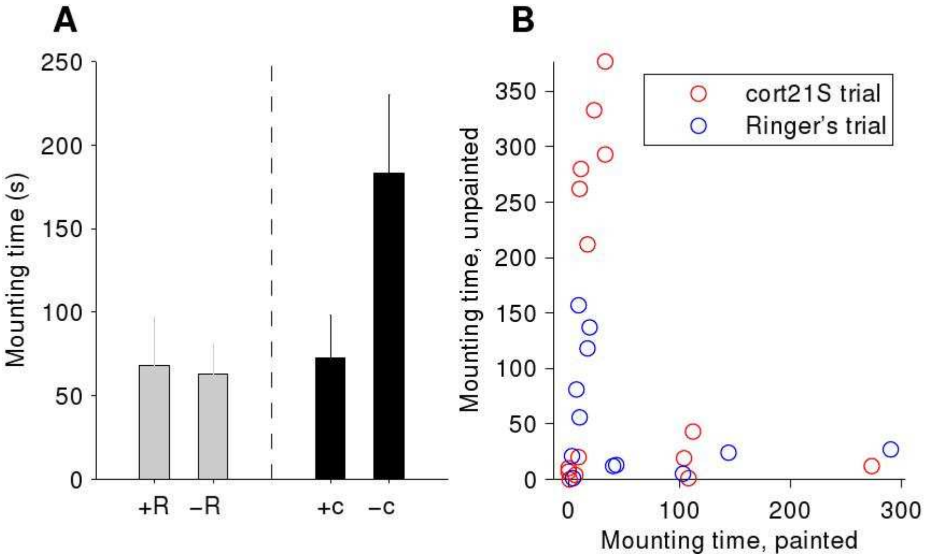

Figure 6.7: Social behavior is affected by cort21S. (A) Males mount Ringers-painted (+R) and unpainted (–R) females for equivalent amounts of time, but prefer unpainted (–c) to cort21S-painted (+c) females. (B) Male mouse presented with two females displayed an almost exclusive preference for one or the other; cort21S signicantly extends the time spent mounting the unpainted female, but does not determine which female is chosen most frequently. This indicates a role for determinants beyond cort21S. Experiments were performed in collaboration with Illya Tolokh.

of sulfated steroids responses in the AOS. They used a battery of 12 sulfated steroids to measure activities of VSNs and mitral cells using electrophysiological methods [80]. Using multi-electrode array (MEA) recording of VSN responses to the 12 ligands, they identified distinct activity patterns[5] in VSN responses. Using single electrode recordings in a hemi-head preparation of the AOS, they measured activities of the mitral cells to the same 12 sulfated steroids. They found that a significant number of response patterns in the VSNs were replicated in the mitral cells, suggesting that in these cases AOB behaves essentially as a relay center. But they also found novel activity patterns in the AOB not directly present in the VNO; these novel patterns could be produced through a linear manipulation of the existing activity patterns in the VNO. This suggested that there were cases where the AOB integrates VSN responses.

6.3.3 Other identified ligands

Exocrine-gland secreting peptides Exocrine-gland secreting peptides (ESPs) were first identified as ligands for the VNO by Touhara and colleagues [65,90]. ESP1 is a male-specific peptide which activates V2R expressing VSNs. Recently it has been shown that the peptide is involved in enhancing female receptivity behavior during mating [91].

Major histocompatability complex peptides The ligands of major histocompatability complex (MHC) have been found to activate basal VSNs [64]. MHC peptides were found to activate specific V2R expressing VSNs at sub-picomolar concentrations [92]. It has been shown that the peptides are sufficient to produce pregnancy block (Bruce effect) in pregnant females — suggesting that the peptides play a role as markers of mouse strain [64].

---

[5] The activity patterns can be thought of as being the chemical receptive fields of the neurons

Major urinary proteins Highly purified major urinary proteins (MUPs) have been found to activate basal VSNs [66,93]. In a particular study, MUPs was sufficient to produce aggressive behavior in male mice [66]. Recently, it has also been shown that the proteins of the MUPs family can produce interspecies defensive behaviors in mice [93].

Formyl peptides Formyl peptide receptor-like peptides have been found to be expressed by VSNs [74, 75]. Typically, formyl peptide receptors are expressed in the immune system, where they detect formylated peptides of bacteria and mitochondria. This new class of VSN receptors are thus hypothesized to help in detection of formylated peptides produced by pathogens or pathogenic states [74, 75].

2-Heptanone 2-Heptanone, a volatile molecule and a component of urine, has been found to activate V1R expressing VSNs [94, 95]. 2-Heptanone specific neurons have been found to detect the molecule at concentrations as low as 10^{-11} M. The molecule is shown to cause estrous cycle extension [95].

6.3.4 Ligands to circuits to behavior

The central question in AOS is how does a specific chemical lead to a stereotyped behavior. The first step in answering the question lies in learning the identity of some of the ligands. Sulfated steroids prove to be an excellent source of ligands which activate the VNO. The large repertoire of sulfated steroids provides the diversity in VSN activation such that one can now start asking population/circuit level questions —how is the information encoded in the VNO and how does the information transform from the VNO to AOB to higher order regions. At the same time one can also start investigating the behavioral responses to the given ligands. Putting together the neuronal responses with the behavioral outcomes will finally allow us to have a basis for understanding how ligands produce stereotyped behavior.

6.4 Studying VNO using OCPI microscopy

VNO studies by Nodari *et al.* and Meeks *et al.* were performed using a multi-electrode array, which consisted of 60 electrodes [67, 80]. Such electrophysiological studies of VNO are powerful due to their ability to perform long experiments (typically 4+ hours). But such studies are constrained by the relatively low number of cells that can be detected in any given experiment[6] and the lack of spatial information of the cells. In Fig. 6.4 we show that OCPI microscopy with calcium imaging can address the two limitations [20]. In a single experiment we were able to measure the tuning properties of ∼700 neurons to male and female urine. Due to the large numbers of identified neurons, we have been able to identify the rare cells which have very high sensitivities to a given stimulus. For example, in six experiments we have identified over ten cells which are responsive to 10^{-4}M-diluted female urine; such highly sensitive cells are rarely detected by MEA recordings. In addition, we have used the spatial information obtained through OCPI microscopy to show that urine activates predominantly the apical regions of the VNO – suggesting that ligands in VNO activate V1R expressing VSNs. Thus calcium imaging using OCPI microscopy on VNO allows for efficient studies of sulfated steroid responses of the VNO.

In [20] we use a bulk loading strategy to label the VSNs with an organic calcium indicator. Such a loading procedure entails inserting a tube into the VNO and applying the dye; the mice are allowed to recover for ∼1 week before the VNO is harvested. This method of labeling is laborious and time consuming. Recently He *et al.* have developed a transgenic mouse model with a genetically encoded calcium indicator (GCaMP2) in the VNO [86]. The combination of OCPI microscopy with the GCaMP2 labeled VSNs should allow for robust studies of VSN responses.

---

[6] Typical MEA experiment followed by spike sorting produces tens of neurons in a single experiment

Chapter 7

Organization of vomeronasal sensory coding revealed by fast volumetric calcium imaging

7.1 Introduction

Neurophysiology is frequently compared to the parable of the blind men and an elephant, in which the exploration of small parts of the elephant leads to very disparate views of its nature. This state of affairs is a consequence of technical barriers that limit the ability to record from more than a few tens or hundreds of neurons simultaneously, typically a small portion of the activity required to represent a naturalistic stimulus. For sensory systems like olfaction—in which odorant information is encoded via the ligand-binding properties of families of hundreds or thousands of distinct receptor types [96]—the limited scale of current recordings poses a major challenge. In principle, natural behaviors may be triggered by a very small percentage of cells, or might alternatively depend upon the collective activity of the full population. With only a partial view of the sensory information possessed by the animal, connecting molecular cues to circuits and behavior remains, particularly for mammals, a major challenge.

One of the most promising approaches to circumvent these barriers is calcium imaging. However, for intact tissue the most commonly-used imaging techniques, two-photon and confocal microscopy, suffer from slow throughput due to the requirement for point-scanning. Consequently, there has been considerable interest in developing alternative fast-scanning microscopes [97], but these do not produce full volumetric data without encountering the fundamental limit on the time spent dwelling over each voxel [19]. Recently we introduced a alternative approach, objective-coupled planar illumination (OCPI) microscopy [20]. Because OCPI microscopy illuminates an entire focal plane at once, it allows parallel acquisition from a million (or more) voxels at once. Consequently, it offers optical sectioning at speeds far higher than point-scanning approaches.

Here we show that OCPI microscopy permits recording from thousands of neurons simultaneously in three-dimensional volumes, and that by successively recording from separate volumes, more than ten thousand neurons may be sampled in a single day. We apply this technique to study sensory coding in the vomeronasal epithelium, a sensory organ detecting chemical cues (sometimes called pheromones) relevant for social communication. Vomeronasal sensory neurons (VSNs) express approximately 300 distinct receptor types [76], of which a single neuron abundantly expresses one or a few types. By sampling from thousands of neurons in a single imaging volume, OCPI microscopy permits nearly-exhaustive recording of the sensory representations at the first stage of this sensory system.

We found that between a quarter and half of all apical VSNs, and a subset of basal VSNs, were activated by just 12 members of a recently-reported family of ligands, sulfated steroids [67,98]. Given the size of the receptor families, one might expect such abundant responses to be extremely diverse, reflecting the action of many receptor types; surprisingly, the large majority of responses were organized into a small number of categories, whose functional characteristics correlated with their spatial position within the epithelium. We discuss the implications of these findings for vomeronasal sensation and as a model for comprehensive recording in the wider nervous system.

7.2 Materials and Methods

7.2.1 Animals

The tetO-GCaMP2 and OMP-IRES-tTA (on a C57Bl6 background) mice were a gift from Ron Yu, Stowers Institute [86, 99]. The F1 generation from the cross were genotyped and the mice containing both the tetO-GCaMP2 and OMP-IRES-tTA genes were used in the experiments. The mice were housed and handled in accord with practices approved by the Washington University Animal Studies Committee. All the mice used in the experiments were female and 12–24 weeks in age.

7.2.2 Imaging

The imaging was performed on a custom Objective Coupled Planar Illumination microscope [20]. Illumination was at 488 nm, the light sheet was $\sim 5\,\mu$m thick, and the objective was a water-immersion 0.5 NA 20× (Olympus). The camera was an iXon DV885-KCS-VP cooled EM-CCD (Andor).

7.2.3 Solutions and stimuli

The excised VNO was continuously superfused with Ringer's solution (115 mM NaCl, 5 mM KCl, 2 mM $CaCl_2$, 2 mM $MgCl_2$, 25 mM $NaHCO_3$, 10 mM HEPES and 10 mM glucose). High-potassium Ringer's (70 mM NaCl, 50 mM KCl, 2 mM $CaCl_2$, 2 mM $MgCl_2$, 25 mM $NaHCO_3$, 10 mM HEPES and 10 mM glucose) was used to test the placement of the superfusion/stimulus delivery tube before the beginning of the experiment. Sulfated steroids were purchased from Steraloids and were stored at −20°C in solid form. We employed the following compounds, referenced by their Steraloids catalog number: A6940, 4-androsten-17α-ol-3-one sulfate (epitestosterone sulfate); A7010, 4-androsten-17β-ol-3-one sulphate (testosterone sulfate); A7864, 5-androsten-3β, 17β-diol disulphate; E0893, 1, 3, 5(10)-estratrien-3, 17α-diol 3-sulphate (17α-estradiol 3-sulfate); E1050, 1, 3, 5(10)-estratrien-3, 17β-diol disulphate (17β-estradiol disulfate); E4105, 4-estren-17β-ol-3-one sulphate (nandrolone sulfate); P3817 5α-pregnan-3α-ol-20-one sulphate (allopregnanolone sulfate); P3865, 5α-pregnan-3β-ol-20-one sulphate (epiallopregnanolone sulfate); P8200, 5β-pregnan-3β-ol-20-one sulphate (epipregnanolone sulfate); Q1570 4-pregnen-11β, 21-diol-3, 20-dione 21-sulphate (corticosterone 21-sulfate); Q3383, 4-pregnen-17-ol-3, 20-dione sulphate; Q3910, 4-pregnen-11β, 17, 21-triol-3, 20-dione 21-sulphate (hydrocortisone 21-sulfate). 100 mM stock solutions of the sulfated steroids were made using either water or methanol and stored at 4°C. Before each experiment, the stock solutions were further diluted with carboxygenated (95% O_2, 5% CO_2) Ringer's solution for a final concentration of 10 μM. Methanol concentration never exceeded 0.01% in the final solutions. 2-heptanone (Sigma-Aldrich) was made by serial dilution into Ringer's, and tested at both 10^{-7} M and 10^{-5} M with identical results. MHC peptide ligands AAPDNRETF and SYFPEITHI (PolyPeptide Laboratories) and fMLF and Lipoxin (Sigma-Aldrich) were tested at 1 μM.

7.2.4 Physiology

At the start of the experiment, the mouse was euthanized under CO_2, decapitated and the VNOs were removed quickly and placed in cold Ringer's solution. The VNO epithelium was carefully removed from the bony capsule, and the tubular corpus cavernosum was separated from the epithelium. The tissue was adhered to a nitrocellulose membrane (Millipore) such that the dendrite layer was on the top. The nitrocelluose membrane was placed on a custom chamber and placed under the OCPI microscope. The tissue was continuously perfused with Ringer's solution, alternating with a given stimulus, all at 35°C. The stimulus and flush were delivered through a custom computer controlled ValveLink fluid handling system (Automate Scientific).

Each stimulus was applied for 30 s following by a 60 s flush (Ringer's solution) period. 40-frame image z-stacks of the neuronal tissue were obtained in 2 s, with a 3 s pause to save the data. Each battery of stimuli was applied 4 times, with the stimulus order being randomized.

7.2.5 Image registration

Small but significant shifting and warping of the tissue occured as the experiment progressed. Such shape-changes were corrected using custom three-dimensional non-rigid registration software that minimized the mean square error compared to a fixed reference stack.

7.2.6 ROI identification

ROIs (regions of interest) were selected manually, each ROI corresponding to a single neuron. No ROIs were drawn in the dendritic knob layer. ROIs were defined unambiguously through their change in fluorescence due to neuronal activity. For Figs. 3–5, both spontaneous and stimulus-driven activity were used to identify ROIs. In the two additional preparations shown in Fig. 7.6, we restricted our analysis to activity coincident with stimulus presentation, identifying 992 and 1004 neurons; of these, over half (527 and 530, respectively) satisfied the criteria for responsiveness and reproducibility.

7.2.7 Functional analysis

For each ROI, the mean intensity was calculated in each stack. A trial was defined as the 4 pre-stimulus stacks and 5 peri- and post-stimulus stacks, and the intensity was normalized to the mean pre-stimulus intensity. Because of a small nonspecific fluorescence increase on each trial (visible in the raw movies, Movie 2 and 3), the average response to Ringer's solution was subtracted from each trace. To calculate the *scalar* $\Delta F/F$ response for a given trial, we defined a weighted average over time using singular value decomposition: Given the the matrix $\mathbf{F}$, where F_{ij} is the fluorescence intensity of the ith ROI on the jth stack, we extracted a block of time around each trial and then used SVD (retaining the first component only) to approximate $\mathbf{F} \approx s\mathbf{u}\mathbf{v}^T$, where $\mathbf{u}$ is a vector whose entries correspond to the intensity of different ROIs, and $\mathbf{v}$ a vector corresponding to the intensity over time. The scalar response in the ith ROI was defined as su_i, or equivalently the dot product of its time course with $\mathbf{v}$. This procedure yielded results which were qualitatively similar to simply averaging over time, but with larger signal-to-noise ratio because it automatically emphasized the time periods of largest $\Delta F/F$. The scalar $\Delta F/F$ values over four trials were used for the t-test for reproducibility; in all other cases, the displayed response was the average across trials.

7.2.8 Clustering analysis

Clustering was performed using a variant of mean shift clustering. To ensure consistent categorization, cells from all three experiments shown in Fig. 7.6 were combined, clustered, and then split back into their individual experiments. Clustering individual experiments yielded very similar results to those shown in Fig. 7.6.

7.2.9 Spatial analysis

The spatial coordinates of the ROIs were corrected for the tilted imaging; the new spatial co-ordinates had perpendicular distance from the surface represented as depth (z position) [20].

7.2.10 Surface analysis

Using a single stack, the VNO surface was identified using an automated algorithm: in each "column" of pixels, the location of the surface was identified as as a sudden increase in intensity, and across columns the locations were median-filtered over a region 21 μm long. Visual inspection was used to verify that this algorithm correctly identified the surface of the tissue in all cases.

7.3 Results

7.3.1 Imaging strategy

OCPI microscopy works by illuminating the objective's focal plane with a thin sheet of light cast perpendicular to the objective's axis (Fig. 7.1A); the objective and illumination optics may be moved together to rapidly scan in three dimensions. A tilted configuration allows surface regions of extended tissues to be visualized. Neuronal activity was visualized via the expression of the calcium-sensitive protein GCaMP2 [16, 86]. Using OCPI microscopy, we scanned a tissue volume $700 \times 175 \times 200\,\mu\mathrm{m}^3$ (Fig. 7.1B) with 5 μm z-spacing in two seconds; this volume contains several thousand sensory neurons, and includes the entire depth of the vomeronasal epithelium. Typical experiments involved the acquisition of nearly one thousand stacks over a period of approximately one hour (Fig. 7.1C). Because excitation is limited to the focal plane, the degree of phototoxicity is many-fold smaller than experienced with confocal microscopy [20], thus enabling long recording sessions.

7.3.2 Characteristics of responses to VSN ligands

We stimulated the epithelium with several classes of previously-reported VSN ligands. Sulfated steroids, a class of compounds first isolated from mouse urine and which conveys information about the current physiological state of conspecifics [67], have been previously studied by electrical recording [67, 80, 100], but no imaging study has examined responses to these ligands. A set of 12 synthetic sulfated steroids from 4 families—androgens, estrogens, pregnanolones, and glucocorticoids (see Methods)—were presented individually at a concentration of $10\,\mu$M over repeated randomly-interleaved trials with periods of flush between stimuli.

VSNs displayed both spontaneous and robust stimulus-driven activity resulting in raw changes in fluorescence ($\Delta F/F$) of magnitudes ranging from a few percent to over 35% (Fig. 7.1C). Activity in hundreds of neurons could be visualized in a single image plane, but the true scale of these recordings can only be appreciated in three-dimensional renderings of the entire volume over time (see static image in Fig. 7.1D). Stimulus responses could be distinguished from spontaneous activity by their clear reproducibility across repeated, interleaved trials (Fig. 7.1E, see also Fig. 7.1C).

We also tested several other classes of previously-reported VSN ligands, including the volatile 2-heptanone, small peptides that bind to the grooves of major histocompatability complex (MHC) receptors, and formylated peptides. These ligands have been reported to activate a small percentage of neurons in the VNO in several studies [64, 74, 94], but other studies have been unable to observe responses to these ligands [67, 75, 101]. Because of the methodological difficulties inherent in studying responses that activate only a few percent of neurons in the VNO, the proper interpretation of these negative data has been unclear. We reasoned OCPI microscopy's comprehensive sampling of the intact vomeronasal epithelium might help refine our

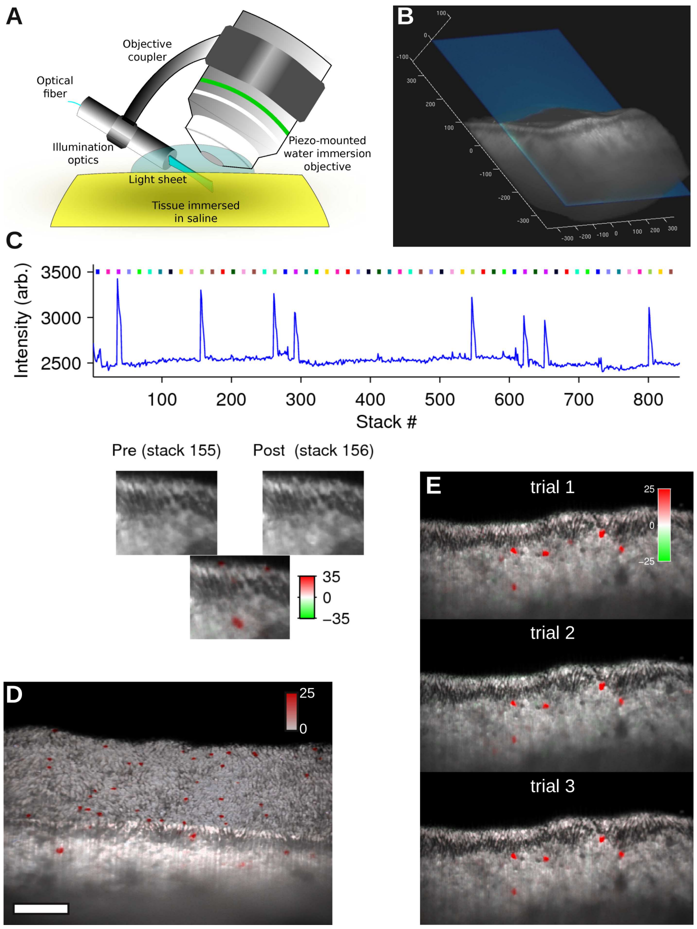

Figure 7.1: (**A**) Schematic of OCPI microscope. The focal plane is illuminated by a thin sheet of light; to scan in three dimensions, the objective and illumination are moved by the piezoelectric manipulator. (**B**) Volume of the vomeronasal organ (VNO) scanned in two seconds (all units in microns). A single plane of illumination (blue) is shown. (**C**) Spatial and temporal representations of fluorescence changes. Below, raw fluorescence images in single optical sections from two successive stacks (dendritic knobs at surface, cell bodies with visible nuclei below); % fluorescence change is also represented in the bottom middle image using a red/green colorscale. Above, mean fluorescence intensity as a function of time for the responsive cell body in the images below; delivery of different stimuli indicated by color bars (10 μM Q1570, olive; 10 μM Q3910, dark magenta). Each stack is acquired in 2 s, with 3 s to save the data. (**D**) Volume rendering of VNO under stimulation by Q1570. Red color scale indicates intensity of fluorescence change, which can be seen in isolated dendritic knobs at the tissue surface as well as in cell bodies deeper in the tissue. Scale bar 100 μm. (**E**) Reproducibility in a single optical section across interleaved repeated presentations of responses to 10 μM Q1570.

understanding of the role of these ligands.

We compared, in single optical sections, responses to 2-heptanone and the sulfated steroids P8200, Q1570 and E1050. While robust responses were seen to the sulfated steroids, 2-heptanone proved to be indistiguishable from Ringer's control (Fig. 7.2A,B). Similar conclusions were reached upon inspection of the entire imaged volume. Occassional spontaneous activity [100] could be distinguished from sensory responses when comparing the same optical section across multiple trials (Movie 5). We also tested the MHC peptide ligands AAPDNRETF and SYFPEITHI [64] and the formylated peptides fMLF and Lipoxin [74]. We were likewise unable to find responses in single optical sections (Fig. 7.2C,D), nor in the imaged volume (Movies 6 and 7). These stimuli were tested on multiple imaging volumes (2-heptanone 0.1 and 10 μM, 5 volumes across 3 epithelia; MHC peptide ligands, 4 volumes across 3 epithelia; fMLF and Lipoxin, 5 volumes across 3 epithelia) that, for each stimulus, collectively contained an estimated 10,000–25,000 neurons. Inspection of these data sets did not reveal obvious examples of neurons that reproducibly responded to any of these non-steroid stimuli.

Given the robust stimulus responses to sulfated steroids, we focused our efforts on characterizing the cell-by-cell patterns of sensory responses to sulfated steroids.

7.3.3 Sulfated steroids activated a large fraction of neurons in the apical VNO

Color-coded representations of the responses to multiple stimuli (Fig. 7.2E,F) suggested that these 12 sulfated steroids activated a sizable percentage of VSNs. We estimated the percentage of responsive neurons in two ways. First, we performed an unbiased pixel-based analysis, computing the maximum response in individual pixels across all 12 sulfated steroids (Fig. 7.2G). In the apical regions of the epithelium (where members of the V1R family of receptors are expressed [70]), responsive

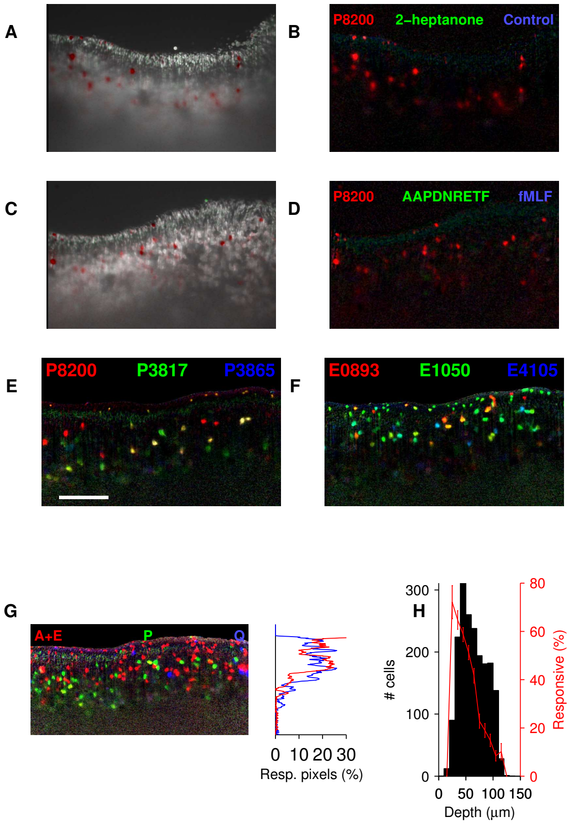

Figure 7.2: (**A**) Single optical section of VNO, with a red/green color scale used to indicate pixels responsive to the sulfated pregnanolone P8200. (**B**) The same optical section, with three overlaid color channels to indicate responses to P8200, 2-heptanone, and Ringer's control. Of these three stimuli, only P8200 caused obvious responses. (**C**) A second preparation, responses to P8200 in a single optical section. (**D**) Same optical section, comparison of responses to P8200 and two putative peptide ligands, AAPDNRETF and fMLF. (**E**) A third preparation, showing a single optical section's responses to three different sulfated pregnanolones. Each pregnanolone causes responses, with some cells responding to more than one of these ligands (indicated by the yellow and white cells). (**F**) Responses to three sulfated estrogens in this same optical section. (**G**) Responses to all 12 steroids as a function of depth within the VNO. Left, a maximum-projection of $\Delta F/F$ across the twelve stimuli displayed as an RGB image (A=androgens, E=estrogens, P=pregnanolones, and Q=glucocorticoids). Right, the percentage of pixels with $\Delta F/F > 5\%$ for raw image (blue) and one in which the surface was computationally "flattened" by aligning columns of pixels (red). The vertical axis is aligned to the image at the left. (**H**) Number of active cells (histogram, left axis) and percentage of these that are steroid-responsive (red line, right axis) as a function of depth below the tissue surface. All panels: responses are average of three trials; color scale from 0 to $15\%\Delta F/F$ (except panel G, which used 0 to $10\%\Delta F/F$); scale bar in E $100\,\mu$m.

pixels consistently occupied $\sim$15–20% of the total volume (single frame shown in Fig. 7.2G; across 36 frames, peak percentage of pixels with $\Delta F/F > 5\%$ was 20±2% mean±std.dev.). However, because of gaps between neurons (e.g., secretory ducts visible as black patches in Fig. 7.1G and Movie 1, and the volume occupied by axons and dendrites), this measure likely underestimates the percentage of cells activated by these stimuli.

We therefore also performed a cell-based analysis, identifying individual neurons by their activity. Within a single imaging volume, we identified 2,446 VSNs as being active, either spontaneously or due to stimulus, at some point during the recording. A large percentage (795 cells, 33%) responded with $\Delta F/F > 3\%$ and $p < 0.05$ (t-test for reproducibility against Ringer's control) to at least one sulfated steroid. In the apical epithelium, the proportion of responsive cells was approximately 50% (Fig. 7.2H). Because activity is used to unambiguously identify cells, and sensory stimulation is an important source of this activity, this likely represents an upper bound.

Thus, both pixel-based and cell-based analyses indicated that these twelve sulfated steroids activated a large fraction—between a quarter and half—of apical VSNs.

7.3.4 VSNs responses to steroids are stereotyped

Given that the apical V1R family contains approximately 200 different genomic sequences, *a priori* one might expect that 25–50% of apical neurons would correspond to a specific population expressing on the order of 50–100 distinct receptor types. This implies a large functional diversity, whose overall features would be difficult to make sense of by traditional techniques. Indeed, displaying the responses using a random ordering of the recorded cells (Fig. 7.3) does not suggest any obvious pattern, consistent with expectations of high diversity. However, the number of responsive cells observed in single preparations by OCPI microscopy was several-fold larger than the anticipated diversity of the population. Because multiple examples of each cell type might be observed in single preparations, the patterns of stimulus responses should reveal the functional organization of this sensory system. We consequently performed a detailed quantitative analysis of these response patterns.

The number of neurons responding to each stimulus varied widely (Fig. 7.4A). In many cases, individual neurons responded to multiple sulfated steroids (Fig. 7.4B). To quantify the specificity of responses across the population, we captured each cell-ligand interaction with a single number, the average $\Delta F/F$, and displayed the population responses with each cell represented by a column of intensities (Fig. 7.4B, left). Remarkably, ordering the cells by response similarity revealed that the majority of responses were accounted for by a modest number of clusters or “processing streams” (Fig. 7.4C).

To test whether these clusters represent arbitrary divisions or instead capture the intrinsic organization of these sensory responses, we reduced these 13-dimensional response vectors to two dimensions using linear discriminant analysis. The top-level two-dimensional projection (Fig. 7.4D) revealed several large, clearly-separated groupings of points, and more focused projections (Fig. 7.4E) confirmed the independence of the remaining clusters. Conversely, a principal components analysis of each cluster individually did not reveal obvious further natural divisions in the data (Fig. 7.5), suggesting that these seven clusters provide a faithful representation of the intrinsic structure of the data. Across preparations, the number of cells in each cluster varied somewhat, but the general pattern was consistent (Fig. 7.6).

7.3.5 Steroid-responsive classes are spatially localized

A further layer of organization was revealed by analyzing the location of responsive neurons according to their functional class. Consistent with the observation that most responsive neurons were apical, virtually all of the clusters also displayed a strong apical bias (Fig. 7.7). However, one processing stream, which responded to

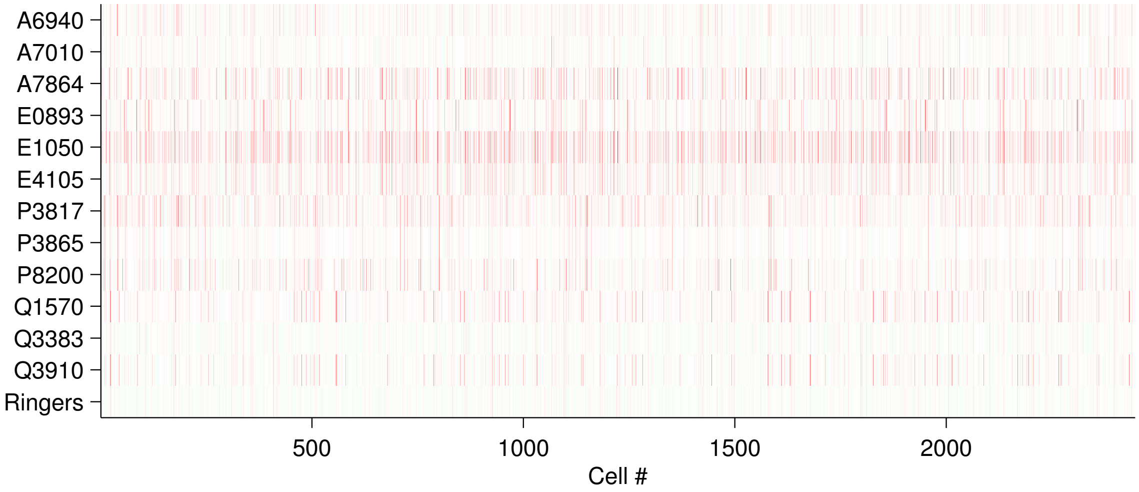

Figure 7.3: Responses to 12 sulfated steroids and the Ringer's control in 2,446 VSNs from a single experiment. Color scale is as shown in Fig. 7.4B.

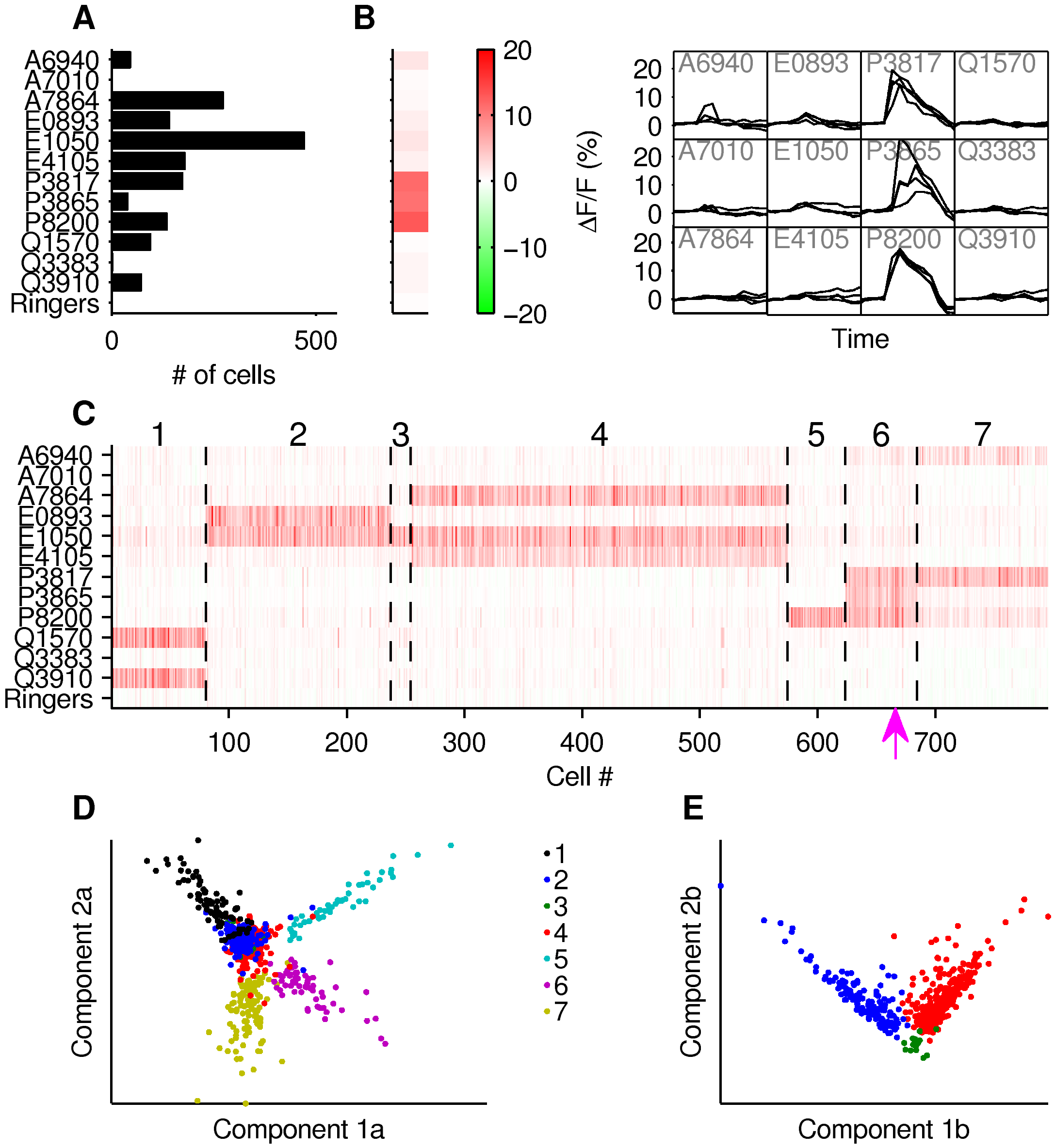

Figure 7.4: (**A**) Histogram of number of cells responding to each stimulus (10 μM) in a single imaging volume. (**B**) A single example cell's responses, plotted as a $\Delta F/F$ color scale (left, stimulus labeling as in panel A) and as traces on individual trials (right). (**C**) Clustered organization of responses across all 795 responsive cells. Each cell displayed as a single column; magenta arrow indicates the example cell in panel B. (**D**) Two-dimensional projection, via linear discriminant analysis, of response data for all clusters (cluster identity indicated by color in legend); each dot represents a single neuron. (**E**) Separate two-dimensional projection of just clusters 2, 3, and 4; these clusters appear to overlap in panel D.

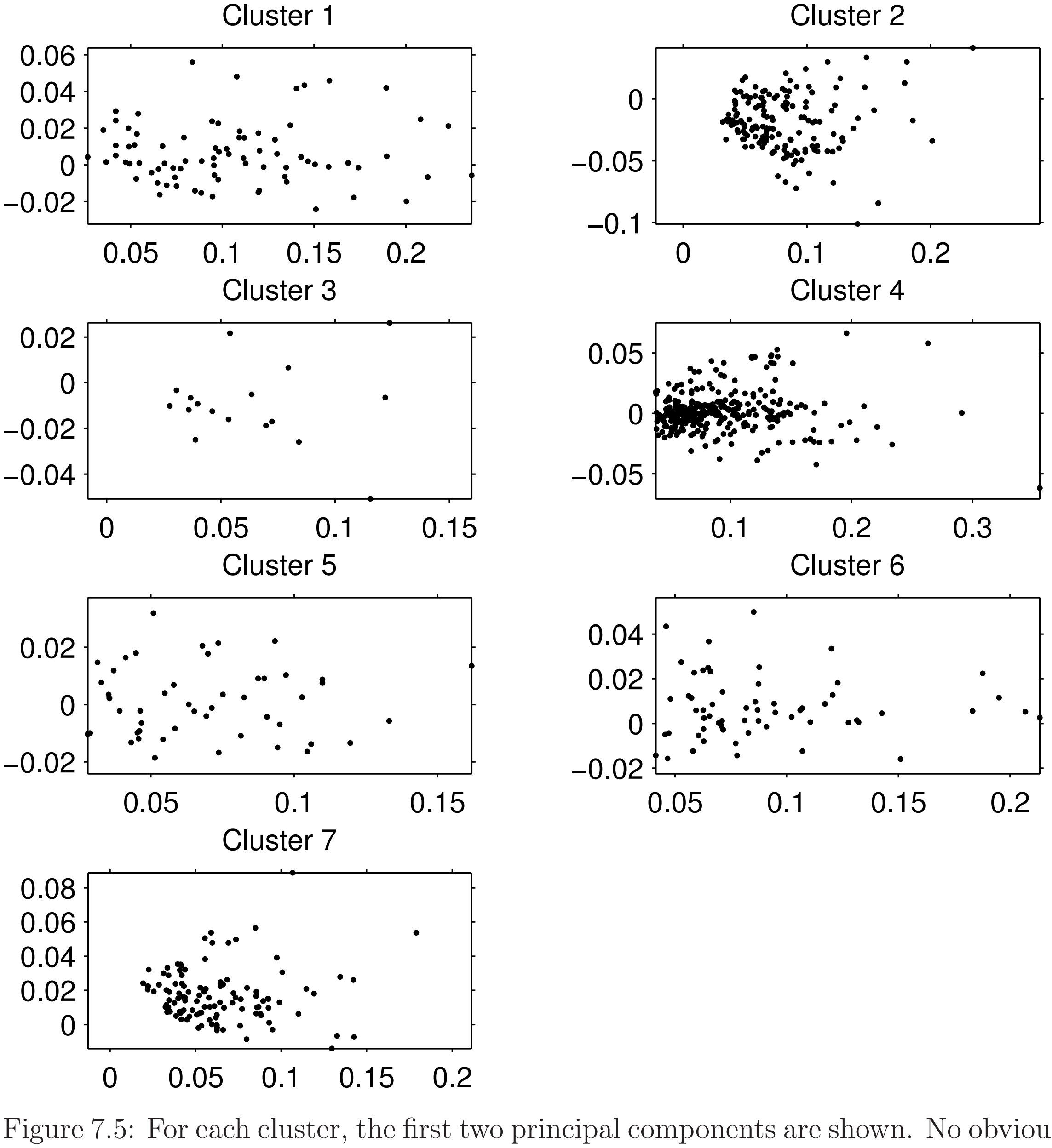

Figure 7.5: For each cluster, the first two principal components are shown. No obvious natural subdivisions can be seen.

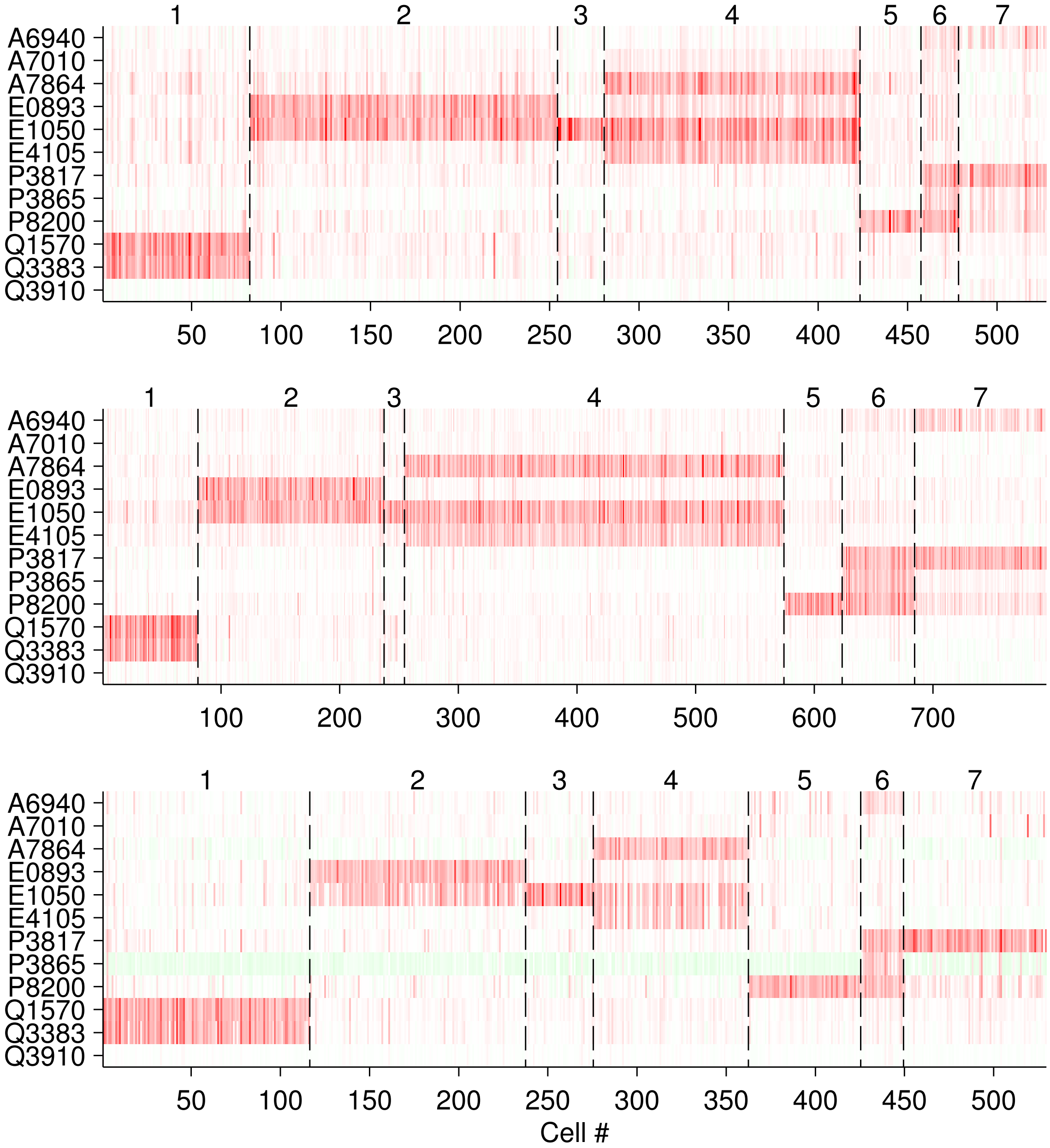

Figure 7.6: Color scale is as shown in Fig. 7.4B. By comparison to Fig. 7.4C (reproduced as the middle panel here), note the omission of Q3383, which was not tested in the third experiment (and was not active in the other two experiments).

both pregnanolones and an androgen (cluster 7 in Fig. 7.4C), was systematically basal (Fig. 7.7B). Consequently, the functional classifications allowed the identification of types that have a corresponding spatial localization within the epithelium.

7.4 Discussion

7.4.1 Fast calcium imaging

Both electrical and optical techniques allow population recording; for “dense recording” from the majority of neurons in a local volume, optical approaches appear to present a number of advantages. However, one challenge for optical recording is that neurons are distributed throughout a three-dimensional space, requiring methods for fast volumetric imaging. There are several strategies for three-dimensional imaging by point-scanning two-photon microscopy [97], but these approaches are limited by a trade-off among speed, volume, and signal-to-noise ratio that arises from the need to collect a sufficient number of photons from each voxel [19]. To circumvent this obstacle, we recently introduced Objective-Coupled Planar Illumination (OCPI) microscopy, which records fluorescence emission from a million or more pixels in parallel while providing optical sections with a thickness of a few microns [20]. From a single optical section, it is possible to record at speeds of hundreds of frames per second, endowing sensitivity (at least when using the organic indicator Oregon Green BAPTA-1) to single action potentials [20]. However, for our purposes here, a much better use of the speed of OCPI was to collect images from many different optical sections, thereby sampling thousands of neurons in a volume hundreds of microns on each side. This approach allowed us to record from neuronal populations that exceed, by a large margin, even the presumptive diversity of the VSN population.

Our results demonstrate that OCPI microscopy enables population recording on an unprecedented scale. Our current implementation of OCPI microscopy allows one

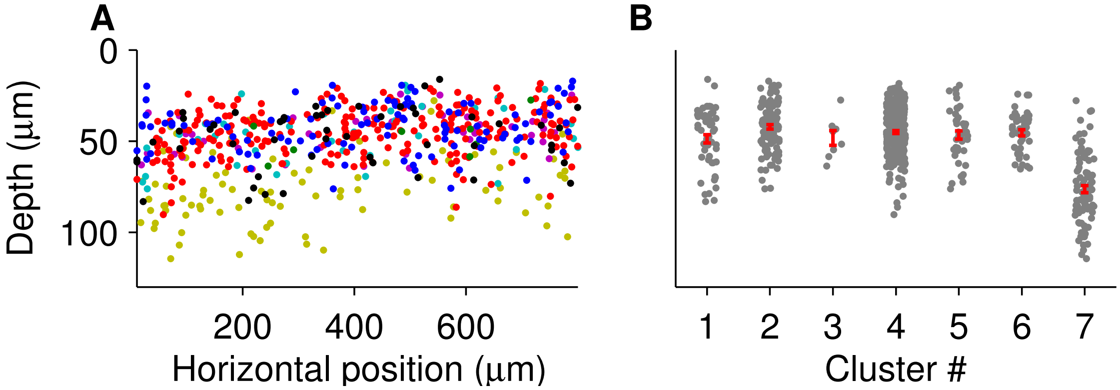

Figure 7.7: (**A**) Scatter plot of cell centers as a function of depth below the tissue surface and the longest imaging axis. Colors indicate cluster number as in Fig. 7.4D. Note axes are not of equal scale. (**B**) Mean and s.e.m. of depth as a function of cluster number. Cell centroids are plotted in gray, with small random horizontal offsets to reduce overlap.

to measure activity in several thousand neurons simultaneously. We have successively imaged multiple locations, thereby recording in excess of ten thousand neurons from a single animal in a single day.

The current speed of OCPI microscopy is far from any physical limit [20], and is set by the rate of data transfer from the camera. Recent and future innovations lead us to expect these numbers to grow considerably in the near future.

7.4.2 Lack of responses to several non-steroid classes of ligands

A surprising outcome of our experiments was the lack of responses to several ligands that have been previously reported to activate VSNs [64, 74, 94]. It is possible that our recordings, despite their apparently-comprehensive nature, somehow missed the activity of these ligands. One scenario is that responses to these ligands were systematically below our threshold for detection, a concern made more likely by the fact GCaMP2, when compared with extracellular recording or organic calcium indicators, has relatively low sensitivity [102]. This possibility cannot be discounted, although the burst firing of VSNs [100] and the abundant spontaneous activity evident in our recordings make this seem unlikely. Moreover, this same mouse was used in one of the reports [86] supporting the effectiveness of MHC peptide ligands, indicating that the properties of GCaMP2 cannot account for all of the differences. These results are also consistent with the results of some [67, 101] electrical recording studies, which are far less comprehensive but have single-spike sensitivity, and also failed to find responses to these ligands.

OCPI microscopy permitted such comprehensive recording, from intact vomeronasal epithelium, that the lack of responses cannot plausibly be attributed to undersampling: given 10,000 neurons, the probability of omitting a class representing 0.1% of the population is less than 10^{-4}. Thus, even quite rare responses, rarer than reported to be responsive to any of these ligands, should have been detected, and so their absence is highly significant. The reasons for the dicrepancies with some (but not all, [67,75,101]) previous studies is not clear. In addition to exhaustive sampling, another advantage of OCPI microscopy is its low phototoxicity. This allowed us to test every neuron reported here with 50–80 stimulus trials (Fig. 7.1C), a number which appears to significantly exceed the number of trials in previous studies that have reported positive results with these ligands. The extra statistical certainty afforded by having more trials is a major benefit in a sensory system whose spontaneous firing properties mimic many aspects of stimulated responses [100].

One possible explanation of the discrepancy is suggested by the observation that odorant receptors from the main olfactory system are sometimes expressed in the VNO [103]. Given reports that both 2-heptanone and the MHC peptide ligands activate the main olfactory system [104], it is possible that responses to these ligands were driven by "misexpressed" odorant receptors; if the amount or type of misexpression varies with the mouse strain being used, it could be a source of significant differences among laboratories.

At a minimum, the abundance and robustness of responses to sulfated steroids, particularly when compared with several previously-reported classes of ligands, suggests that steroid metabolites may play a particularly central role in vomeronasal sensation.

7.4.3 Abundant and stereotyped VSN responses to sulfated steroids

The mouse genome contains approximately 200 presumed-functional V1R family members [77,105]. A collection of just 12 sulfated steroids, delivered at 10 μM, activated between a quarter and half of all apical cells. The sheer number of these responses demonstrates the centrality of sulfated steroids to vomeronasal sensory coding.

From the size of the V1R family, one might naïvely expect that this fraction of cells would express between 50–100 different receptor types. Previously, we showed by multielectrode array recording [80] that VSN responses can be grouped into "processing streams," but the number of streams that could be distinguished was largely limited by the number of neurons sampled. Volumetric calcium imaging did identify new classes of response (e.g., 2 of the 3 pregnanolone-responsive types here were not detected in those previous recordings), but the most striking and unexpected outcome from calcium imaging is the extreme stereotypy of VSN responses to these 12 sulfated steroids. Even though these represent a small fraction of all possible sulfated steroid structures, in principle 12 compounds should be sufficient to distinguish hundreds or thousands of types even using all-or-none classification of responses ($2^{12} = 4096$). That so many of the potential response types were not observed suggests that individual receptors have a limited receptive range; that the few observed types accounted for so many cells indicates their disproportionate abundance in the neuroepithelium.

It is worth noting that the processing streams do not typically correspond to cells responding to a single ligand; instead, they are defined only by the pattern of responses across ligands. For example, clusters 2, 3, and 4 contained cells that all responded to E1050; these clusters are distinguished by their responses to the other two E-family compounds. Examples of cells in these clusters can be seen in Fig. 7.2E&F; the distinct processing streams can be recognized visually from the fact that particular color combinations appear repeatedly while others do not appear at all.

What might account for the unexpected degree of order revealed by these large-scale population recordings? One possibility is that each processing stream represents a collection of multiple receptor types with overlapping or redundant functional properties. This possibility is consistent with the observation that, among the families of mammalian and insect odorant receptors, vomeronasal receptors are unusual in possessing a number of distinct sub-families tightly clustered by amino acid sequence [106]. Alternatively, it seems possible that these processing streams correspond to single receptor types, but these types are expressed by a large percentage of neurons. Indeed, in certain regions of the mouse main olfactory epithelium, just one receptor type, MOR28, is expressed by approximately 10% of all olfactory sensory neurons [107], and among the V1R receptors, approximately half of the total expression is attributable to the V1Rc and V1Rd subfamilies [108]. This possibility appears to be consistent with recent results identifying individual vomeronasal receptors expressed by cells showing immediate-early gene expression in mice exposed to sulfated steroids [109]. While making a precise correspondence is not possible due to differences in stimuli and methodology, our cluster 1 may correspond to V1re2 and V1re6, cluster 2 with V1rf3, and cluster 4 with V1rj2. Because the receptor identification may not have been exhaustive, it is possible that other receptor types with similar response profiles also contribute to these clusters.

The strong apical bias (Fig. 7.7) suggests that the vast majority of steroid-responsive neurons express members of the V1R family. However, one particular processing stream was found almost exclusively in the basal VNO (Fig. 7.7). These neurons may express members of the V2R family of receptors, indicating that sulfated steroids are detected by members of both major families of vomeronasal receptors. Alternatively, because the location of the V1R/V2R boundary is slightly variable [68, 110], these neurons may represent a population of deep V1R-expressing neurons.

7.4.4 Conclusions

OCPI microscopy's comprehensive sampling revealed unexpected stereotypy and spatial organization in the sensory representations of the vomeronasal organ. In neuronal circuits, functional diversity is the rule rather than the exception. It seems likely that the ability to record on a large scale will yield further new insights about the organization of the nervous system.

Chapter 8

Perspectives on accessory olfactory system

8.1 Calcium imaging with OCPI microscopy to study VNO

A major limitation in the field of AOS (and olfaction in general) has been the lack of techniques available to measure activities of large populations of neurons; OCPI microscopy with calcium imaging is poised to fill that void. It will allow for experiments which reveal new insights into the functioning of the AOS. In Chapter#7 I described one of the first applications of the method. Possible extensions to the work are given below.

8.1.1 Sex differences in sulfated steroid responsive VSNs

Currently the data in literature is conflicting on the possibility of sexual dimorphism in VSN expression pattern. Previous electrophysiological studies [67, 85] show lack of evidence for sexual dimorphism in the expression of sulfated steroid responsive VSNs; but the small number of neurons studied in the experiments do not allow for measuring possible small but significant differences. Fos-immunochemistry studies suggests sexual dimorphism in the V2R family [111–113].

One of the main reason for such ambiguity is the lack of experimental techniques to measure possible small differences in receptor types in the VNO. Calcium imaging with OCPI microscopy allows for measuring such putative small differences. Performing sexual dimorphism studies is relatively straight forward; the experimental and analysis architecture developed in the previous chapter can be readily applied. Ideally, calcium imaging should be performed on the male and female mice from the same litter — this will allow for a simple control for age and environmental factors. Care must be taken to control for the estrous state of the females[1]. Performing calcium imaging with OCPI microscopy on the VNOs of the male and female mice, one will be obtain functional clustering of the VSNs; any differences in the number of VSNs in each of the clusters will demonstrate sexual dimorphism in the sulfated steroid responsive VSNs.

8.1.2 Receptor affinities of sulfated steroid responsive VSNs

In the VNO, a VSN is activated when a ligand binds to its receptor. The concentration at which the ligand activates the neuron depends on the tuning properties of the ligand-receptor pair[2]. Preliminary data show the existence of high and low affinity receptors for some of the sulfated steroids [67]. Such a dichotomy of receptor affinities suggests that different concentration ranges of a ligand leads to different VSN activation patterns; different concentration ranges might then ultimately lead to different behavioral outcomes.

Calcium imaging with OCPI microscopy allows for performing such tuning studies

---

[1] Any changes in VSN expression pattern dependent on the estrous state of the female will, on its own, be an interesting finding.

[2] The ligand-receptor tuning concentration range is thought to correlate with the behaviorally relevant concentration range. Thus the study of tuning properties of VSNs will allow for a better characterization of the behaviorally relevant concentration ranges.

efficiently. The benefit of the imaging study is that one will be able to measure activities of thousands of neurons, and from them identify the tens or even hundreds of neurons which are activated by the given steroid. Calculating the tuning properties of neurons from such large populations of responsive VSNs, one should be able to identify (if any) the presence of receptors of different affinities to the same ligand.

8.1.3 Sex/strain selectivity of VSNs to mouse urine

Mouse urine activates VSNs selectively — based on sex and strain of the urine [85–87]. Previous studies have been constrained by the number of neurons that can be measured in a single experiment. Using OCPI microscopy and calcium imaging, one can apply mouse urine of different sexes/strains and obtain the tuning properties of each VSN to the given stimuli (see Fig. 8.1 for preliminary data). We can thus obtain a comprehensive population level picture of the sex/strain selectivity of VSNs.

The sex/strain information from the VNO is thought to undergo transformation in the AOB to produce characteristic behavioral outputs; the prevailing wisdom suggests for the role of lateral inhibition in sex/strain identification in the AOB [78, 79]. A comprehensive sex/strain study of VNO will allow for robust comparison between the VSN activity profiles and the activities of the mitral cells; such a large scale comparison will help in elucidating the role of the AOB in sex/strain identification.

8.1.4 Systematic verification of other ligands

In addition to the sulfated steroids, the identified ligands to the VNO include exocrine secreting peptides (ESPs) [65, 90, 91], major histocompatibility compounds (MHC peptides) [64, 92], major urinary proteins (MUPs) [66, 93], formylated peptides [74] and small volatile compounds (ex. 2-heptanone) [94]. The exact number, location and tuning properties of the VSNs responding to these ligands have not been studied at the population scale. More importantly, some of the ligands do not produce neuronal

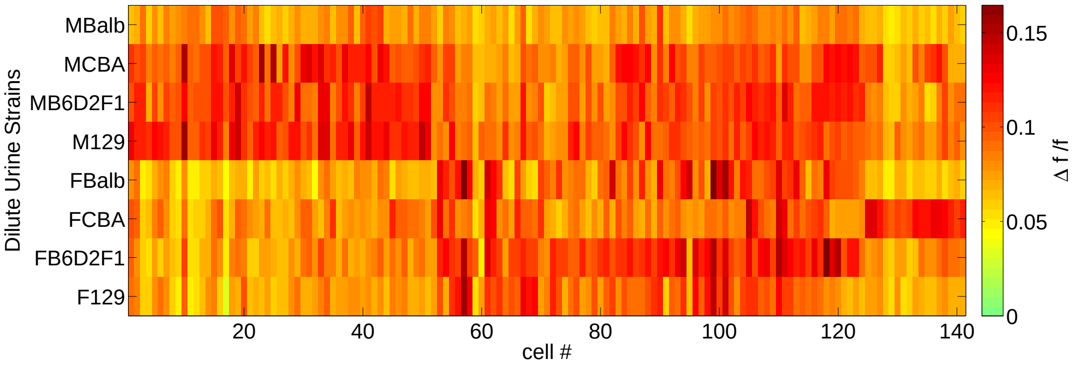

Figure 8.1: Neuronal responses of VNO to mouse urine of different sexes and strains: OCPI imaging on GCaMP2 labeled VSNs was performed using a similar experimental paradigm as described in the previous chapter. A preliminary analysis of ∼200 identified neurons show distinct patterns in VSN activities. Further analysis with larger number of VSNs will allow for better understanding of the sex and strain selectivity of VSNs. The colormap shows the ratio of change in fluorescence, $\Delta f/f$. Figure provided by Illya Tolokh.

activity as measured using MEA recording [67][3]. Using OCPI microscopy and calcium imaging one can re-evaluate the functionality of the ligands. For example, preliminary results of a functional assay for 2-heptanone [94] is shown in Fig. 8.2. In the identified ∼1000 VSNs, I couldn't find any VSNs selective for 2-heptanone. Such experiments have to repeated to prove the lack of VSNs responsive to the given ligand.

---

[3] Lack of responses using MEA recording may not rule out the functionality of the ligands due to possible biases present in the recording technique.

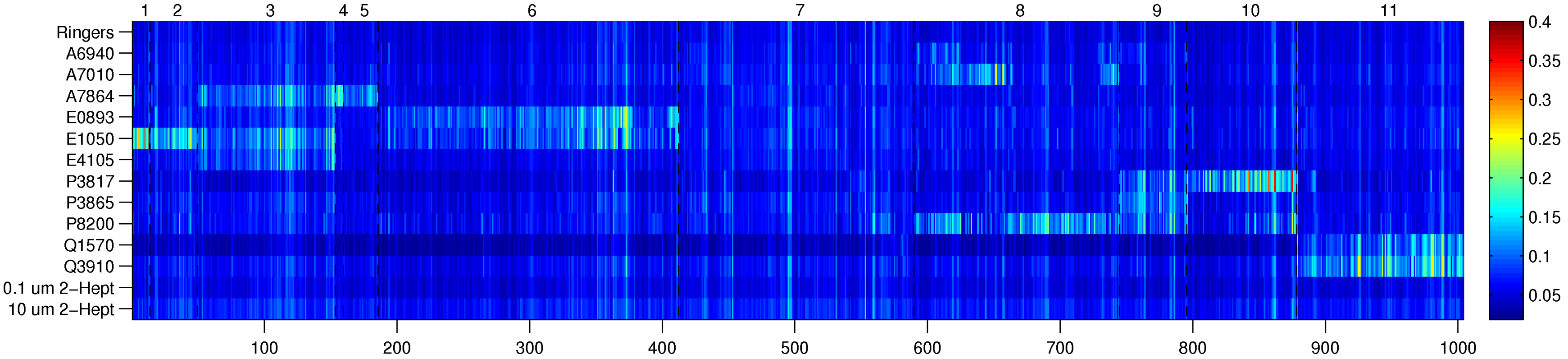

Figure 8.2: Neuronal responses of VNO to sulfated steroids and 2-Heptanone: OCPI imaging with GCaMP2 labeled VNO was performed using a similar experimental paradigm as described in the previous chapter. In addition to the 11 sulfated steroids, two concentrations of 2-Heptanone were used in the stimulus set. We did not find any neurons which were selective only for 2-Heptanone at these concentrations (0.1μM and 10μM, higher than the concentration used in [94]). The colormap shows the ratio of change in fluorescence, $\Delta f/f$.

8.1.5 Next step in AOS processing – accessory olfactory bulb

Mice with GCaMP2 labeled VNO also allow for functional imaging of the AOB; the axon terminals of the VSNs have sufficient labeling to allow for imaging the glomeruli they innervate. Using OCPI imaging on a hemi-head VNO-AOB preparation [114], we have been able to measure reproducible activities from specific glomeruli in response to specific sulfated steroids (Fig. 8.3). In the main olfactory system, it is known that each of the olfactory sensory neuron type converges on to the same set of glomeruli across animals [115]. Such a study has not been performed in the AOS due experimental constraints[4]. The hemi-head preparation with OCPI microscopy allows for asking similar question in the AOS: Do VSNs which respond to the same ligand activate the same glomeruli in the AOB? And if so, are they located at the same positions across animals?

8.2 Conclusion

OCPI imaging with calcium imaging will prove to be major advancement in the study of VNO. The high throughput nature of the methodology allows for ligand screens, ligand characterization, and study of neural processing of the ligand information. The results obtained will further elucidate the mechanism behind effects of individual ligands on murine behavior.

---

[4] AOB is located in a position which is not easily accessible for imaging using OCPI microscopy. The hemi-head preparation circumvents the steric issues and allows for imaging the AOB at high spatial and temporal resolution.

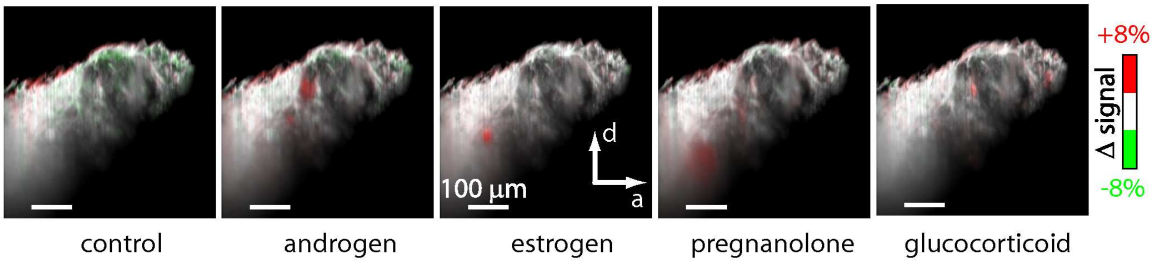

Figure 8.3: AOB glomerular responses to sulfated steroids: OCPI imaging with GCaMP2 labeled VNO was performed, but this time imaging the axon terminals in the AOB using a hemi-head preparation [114]. One can clearly see activation of specific glomeruli upon stimulation with specific sulfated steroids. Figure provided by Julian Meeks.

Appendix A

Appendix

A.1 Abbreviations

2D: two-dimenstional

3D: three-dimensional

AO: adaptive optics

AOB: accessory olfactory bulb

AOS: accessory olfactory system

cort21S: Corticosterone 21-sulfate

DM: deformable mirror

FOV: field of view

GCaMP: genetically encoded calcium sensitive protein

GFP: green fluorescent protein

LSFM: light sheet fluorescence microscope

LSM: laser scanning microscope

MEA: multielectrode array

MOS: main olfactory system

MRI: magnetic resonance imaging

NA: numerical aperture

OCPI: objective coupled planar illumination

OSN: olfactory sensory neuron

PD: phase diversity

PDI: phase diverse imaging

PDMS: polydimethylsiloxane

PSF: point spread function

ROI: region of interest

SNR: signal-to-noise ratio

VNO: vomeronasal organ

VSN: vomeronasal sensory neuron (primary sensory neuron of the AOS)

Bibliography

[1] Churchland PS, Sejnowski TJ (1988) Perspectives on cognitive neuroscience. Science 242:741–745.

[2] Hubel D, Wiesel T (1962) Receptive fields, binocular interaction and functional architecture in the cat's visual cortex. J Physiol (Lond) 160:106–154.

[3] Buzsaki G (2004) Large-scale recording of neuronal ensembles. Nat Neurosci 7:446–451.

[4] Shlens J, Field GD, Gauthier JL, Greschner M, Sher A, et al. (2009) The structure of large-scale synchronized firing in primate retina. J Neurosci 29:5022–5031.

[5] Raichle M (2003) Functional brain imaging and human brain function. J Neurosci 23:3959–3962.

[6] Tyszka J, Fraser S, Jacobs R (2005) Magnetic resonance microscopy: recent advances and applications. Curr Opin Biotechnol 16:93–99.

[7] Kerr J, Denk W (2008) Imaging in vivo: watching the brain in action. Nat Rev Neurosci 9:195–205.

[8] Scanziani M, Hausser M (2009) Electrophysiology in the age of light. Nature 461:930–939.

[9] Buzsaki G, Kaila K, Raichle M (2007) Inhibition and brain work. Neuron 56:771–783.

[10] Conchello J, Lichtman J (2005) Optical sectioning microscopy. Nat Methods 2:920–931.

[11] Ntziachristos V (2010) Going deeper than microscopy: the optical imaging frontier in biology. Nat Methods 7:603–614.

[12] Denk W, Strickler J, Webb W (1990) Two-photon laser scanning fluorescence microscopy. Science 248:73–76.

[13] Helmchen F, Denk W (2005) Deep tissue two-photon microscopy. Nat Methods 2:932–940.

[14] Saggau P (2006) New methods and uses for fast optical scanning. Curr Opin Neurobiol 16:543–550.

[15] Tsien RY (1980) New calcium indicators and buffers with high selectivity against magnesium and protons: design, synthesis, and properties of prototype structures. Biochemistry 19:2396–2404.

[16] Tallini YN, Ohkura M, Choi BR, Ji G, Imoto K, et al. (2006) Imaging cellular signals in the heart in vivo: Cardiac expression of the high-signal Ca2+ indicator GCaMP2. Proc Natl Acad Sci USA 103:4753–4758.

[17] Tian L, Hires SA, Mao T, Huber D, Chiappe ME, et al. (2009) Imaging neural activity in worms, flies and mice with improved GCaMP calcium indicators. Nat Methods 6:875–881.

[18] Wang Q, Shui B, Kotlikoff MI, Sondermann H (2008) Structural basis for calcium sensing by GCaMP2. Structure 16:1817–1827.

[19] Pawley J (2006) Handbook of Biological Confocal Microscopy. Springer.

[20] Holekamp T, Turaga D, Holy T (2008) Fast three-dimensional fluorescence imaging of activity in neural populations by objective-coupled planar illumination microscopy. Neuron 57:661–672.

[21] Ohki K, Chung S, Ch'ng Y, Kara P, Reid R (2005) Functional imaging with cellular resolution reveals precise micro-architecture in visual cortex. Nature 433:597–603.

[22] Yaksi E, Friedrich R (2006) Reconstruction of firing rate changes across neuronal populations by temporally deconvolved Ca2+ imaging. Nat Methods 3:377–383.

[23] Vucinic D, Sejnowski TJ (2007) A compact multiphoton 3D imaging system for recording fast neuronal activity. PLoS ONE 2:e699.

[24] Duemani Reddy G, Kelleher K, Fink R, Saggau P (2008) Three-dimensional random access multiphoton microscopy for functional imaging of neuronal activity. Nat Neurosci 11:713–720.

[25] Grewe BF, Langer D, Kasper H, Kampa BM, Helmchen F (2010) High-speed in vivo calcium imaging reveals neuronal network activity with near-millisecond precision. Nat Methods 7:399–405.

[26] Bewersdorf J, Pick R, Hell SW (1998) Multifocal multiphoton microscopy. Opt Lett 23:655–657.

[27] Ji N, Magee JC, Betzig E (2008) High-speed, low-photodamage nonlinear imaging using passive pulse splitters. Nat Methods 5:197–202.

[28] Nikolenko V, Watson BO, Araya R, Woodruff A, Peterka DS, et al. (2008) SLM Microscopy: Scanless Two-Photon Imaging and Photostimulation with Spatial Light Modulators. Front Neural Circuits 2:5.

[29] Watson BO, Nikolenko V, Yuste R (2009) Two-photon imaging with diffractive optical elements. Front Neural Circuits 3:6.

[30] Siedentopf H, Zsigmondy R (1903) Ueber Sichtbarmachung ultramikroskopischer Teilchen, mit besonderer Anwendung auf Goldrubinglser. J Phys Theor Appl 2:692702.

[31] Voie AH, Burns DH, Spelman FA (1993) Orthogonal-plane fluorescence optical sectioning: three-dimensional imaging of macroscopic biological specimens. J Microsc 170:229–236.

[32] Fuchs E, Jaffe J, Long R, Adam F (2002) Thin laser light sheet microscope for microbial oceanography. Optics Express 10:145.

[33] Huisken J, Swoger J, Del Bene F, Wittbrodt J, Stelzer E (2004) Optical sectioning deep inside live embryos by selective plane illumination microscopy. Science 305:1007–1009.

[34] Dodt H, Leischner U, Schierloh A, Jhrling N, Mauch C, et al. (2007) Ultramicroscopy: three-dimensional visualization of neuronal networks in the whole mouse brain. Nat Methods 4:331–336.

[35] Buytaert JA, Dirckx JJ (2007) Design and quantitative resolution measurements of an optical virtual sectioning three-dimensional imaging technique for biomedical specimens, featuring two-micrometer slicing resolution. J Biomed Opt 12:014039.

[36] Huisken J, Stainier DY (2009) Selective plane illumination microscopy techniques in developmental biology. Development 136:1963–1975.

[37] Engelbrecht CJ, Stelzer EH (2006) Resolution enhancement in a light-sheet-based microscope (SPIM). Opt Lett 31:1477–1479.

[38] Keller PJ, Schmidt AD, Wittbrodt J, Stelzer EH (2008) Reconstruction of zebrafish early embryonic development by scanned light sheet microscopy. Science 322:1065–1069.

[39] Keller PJ, Schmidt AD, Santella A, Khairy K, Bao Z, et al. (2010) Fast, high-contrast imaging of animal development with scanned light sheet-based structured-illumination microscopy. Nat Methods .

[40] Jung JC, Mehta AD, Aksay E, Stepnoski R, Schnitzer MJ (2004) In vivo mammalian brain imaging using one- and two-photon fluorescence microendoscopy. J Neurophysiol 92:3121–3133.

[41] Dirckx J, Kuypers L, Decraemer W (2005) Refractive index of tissue measured with confocal microscopy. J Biomed Opt 10:44014.

[42] Lopez-Bendito G, Sturgess K, Erdolyi F, Szabo G, Molner Z, et al. (2004) Preferential origin and layer destination of GAD65-GFP cortical interneurons. Cereb Cortex 14:1122–1133.

[43] Booth MJ (2007) Adaptive optics in microscopy. Philos Transact A Math Phys Eng Sci 365:2829–2843.

[44] Turaga D, Holy TE (2008) Miniaturization and defocus correction for objective-coupled planar illumination microscopy. Opt Lett 33:2302–2304.

[45] Tyson R (2000) Introduction to Adaptive Optics. Bellingham, Washington: SPIE Press Book.

[46] Porter J, Queener H, Lin J (2006) Adaptive optics for vision science: principles,practices, design and applications. Newark, NJ: Wiley.

[47] Feierabend M, Ruckel M, Denk W (2004) Coherence-gated wave-front sensing in strongly scattering samples. Opt Lett 29:2255–2257.

[48] Hermann B, Fernandez EJ, Unterhuber A, Sattmann H, Fercher AF, et al. (2004) Adaptive-optics ultrahigh-resolution optical coherence tomography. Opt Lett 29:2142–2144.

[49] Booth MJ, Neil MA, Juskaitis R, Wilson T (2002) Adaptive aberration correction in a confocal microscope. Proc Natl Acad Sci USA 99:5788–5792.

[50] Debarre D, Botcherby EJ, Watanabe T, Srinivas S, Booth MJ, et al. (2009) Image-based adaptive optics for two-photon microscopy. Opt Lett 34:2495–2497.

[51] Hanser BM, Gustafsson MG, Agard DA, Sedat JW (2004) Phase-retrieved pupil functions in wide-field fluorescence microscopy. J Microsc 216:32–48.

[52] Gonsalves RA (1982) Phase retrieval and diversity in adaptive optics. Optical Engineering 21:829–832.

[53] Paxman R, Schulz T, Fienup J (1992) Joint estimation of object and aberrations by using phase diversity. J Opt Soc Am A 9:1072.

[54] Born M, Wolf E (1999) Principles of optics: electromagnetic theory of propagation, interference and diffraction of light; 7th ed. Cambridge: Cambridge Univ. Press.

[55] Booth M, Wilson T, Sun HB, Ota T, Kawata S (2005) Methods for the characterization of deformable membrane mirrors. Appl Opt 44:5131–5139.

[56] Melnikov Y (2004) Influence functions of a point force for Kirchoff plates with rigid inclusions. J Mechanics 20:249.

[57] Lofdahl MG, Scharmer GB, Wei W (2000) Calibration of a deformable mirror and Strehl ratio measurements by use of phase diversity. Appl Opt 39:94–103.

[58] Fernandez EJ, Vabre L, Hermann B, Unterhuber A, Povazay B, et al. (2006) Adaptive optics with a magnetic deformable mirror: applications in the human eye. Opt Express 14:8900–8917.

[59] Buck L (2000) The molecular architecture of odor and pheromone sensing in mammals. Cell 100:611–618.

[60] Shipley M, Ennis M (1996) Functional organization of olfactory system. J Neurobiol 30:123–176.

[61] Kandel ER (2000) Principles of Neural Science. McGraw-Hill Education.

[62] Dulac C, Torello A (2003) Molecular detection of pheromone signals in mammals: from genes to behaviour. Nat Rev Neurosci 4:551–562.

[63] Stowers L, Holy T, Meister M, Dulac C, Koentges G (2002) Loss of sex discrimination and male-male aggression in mice deficient for TRP2. Science 295:1493–1500.

[64] Leinders-Zufall T, Brennan P, Widmayer P, S P, Maul-Pavicic A, et al. (2004) MHC class I peptides as chemosensory signals in the vomeronasal organ. Science 306:1033–1037.

[65] Kimoto H, Haga S, Sato K, Touhara K (2005) Sex-specific peptides from exocrine glands stimulate mouse vomeronasal sensory neurons. Nature 437:898–901.

[66] Chamero P, Marton T, Logan D, Flanagan K, Cruz J, et al. (2007) Identification of protein pheromones that promote aggressive behaviour. Nature 450:899–902.

[67] Nodari F, Hsu FF, Fu X, Holekamp T, Turk J, et al. (2008) Sulfated steroids as natural ligands for mouse pheromone-sensing neurons. J Neurosci 00:000.

[68] Herrada G, Dulac C (1997) A novel family of putative pheromone receptors in mammals with a topographically organized and sexually dimorphic distribution. Cell 90:763–773.

[69] Liman E, Corey D (1996) Electrophysiological characterization of chemosensory neurons from the mouse vomeronasal organ. J Neurosci 16:4625–4637.

[70] Dulac C, Axel R (1995) A novel family of genes encoding putative pheromone receptors in mammals. Cell 83:195–206.

[71] Matsunami H, Buck L (1997) A multigene family encoding a diverse array of putative pheromone receptors in mammals. Cell 90:775–784.

[72] Ryba N, Tirindelli R (1997) A new multigene family of putative pheromone receptors. Neuron 19:371–379.

[73] Pantages E, Dulac C (2000) A novel family of candidate pheromone receptors in mammals. Neuron 28:835–845.

[74] Riviere S, Challet L, Fluegge D, Spehr M, Rodriguez I (2009) Formyl peptide receptor-like proteins are a novel family of vomeronasal chemosensors. Nature 459:574–577.

[75] Liberles SD, Horowitz LF, Kuang D, Contos JJ, Wilson KL, et al. (2009) Formyl peptide receptors are candidate chemosensory receptors in the vomeronasal organ. Proc Natl Acad Sci USA 106:9842–9847.

[76] Touhara K, Vosshall LB (2009) Sensing odorants and pheromones with chemosensory receptors. Annu Rev Physiol 71:307–332.

[77] Shi P, Zhang J (2007) Comparative genomic analysis identifies an evolutionary shift of vomeronasal receptor gene repertoires in the vertebrate transition from water to land. Genome Res 17:166–174.

[78] Hendrickson RC, Krauthamer S, Essenberg JM, Holy TE (2008) Inhibition shapes sex selectivity in the mouse accessory olfactory bulb. J Neurosci 28:12523–12534.

[79] Ben-Shaul Y, Katz LC, Mooney R, Dulac C (2010) In vivo vomeronasal stimulation reveals sensory encoding of conspecific and allospecific cues by the mouse accessory olfactory bulb. Proc Natl Acad Sci USA 107:5172–5177.

[80] Meeks JP, Arnson HA, Holy TE (2010) Representation and transformation of sensory information in the mouse accessory olfactory system. Nat Neurosci 13:723–730.

[81] Larriva-Sahd J (2008) The accessory olfactory bulb in the adult rat: a cytological study of its cell types, neuropil, neuronal modules, and interactions with the main olfactory system. J Comp Neurol 510:309–350.

[82] Meisami E, Bhatnagar KP (1998) Structure and diversity in mammalian accessory olfactory bulb. Microsc Res Tech 43:476–499.

[83] Holy TE, Guo Z (2005) Ultrasonic songs of male mice. PLoS Biol 3:e386.

[84] Bruce HM (1959) An exteroreceptive block to pregnancy in the mouse. Nature 84:105.

[85] Holy T, Dulac C, Meister M (2000) Responses of vomeronasal neurons to natural stimuli. Science 289:1569–1572.

[86] He J, Ma L, Kim S, Nakai J, Yu C (2008) Encoding gender and individual information in the mouse vomeronasal organ. Science 320:535–538.

[87] He J, Ma L, Kim S, Schwartz J, Santilli M, et al. (2010) Distinct signals conveyed by pheromone concentrations to the mouse vomeronasal organ. J Neurosci 30:7473–7483.

[88] Zahavi A (1975) Mate selection-a selection for a handicap. J Theor Biol 53:205–214.

[89] Guilford T (1995) Animal signals: all honesty and light? Trends in Ecology and Evolution 10:100 – 101. doi:DOI:10.1016/S0169-5347(00)89001-1.

[90] Kimoto H, Sato K, Nodari F, Haga S, Holy TE, et al. (2007) Sex- and strain-specific expression and vomeronasal activity of mouse ESP family peptides. Curr Biol 17:1879–1884.

[91] Haga S, Hattori T, Sato T, Sato K, Matsuda S, et al. (2010) The male mouse pheromone ESP1 enhances female sexual receptive behaviour through a specific vomeronasal receptor. Nature 466:118–122.

[92] Leinders-Zufall T, Ishii T, Mombaerts P, Zufall F, Boehm T (2009) Structural requirements for the activation of vomeronasal sensory neurons by MHC peptides. Nat Neurosci 12:1551–1558.

[93] Papes F, Logan DW, Stowers L (2010) The vomeronasal organ mediates interspecies defensive behaviors through detection of protein pheromone homologs. Cell 141:692–703.

[94] Leinders-Zufall T, Lane A, Puche A, Ma W, Novotny M, et al. (2000) Ultrasensitive pheromone detection by mammalian vomeronasal neurons. Nature 405:792–796.

[95] Boschat C, Pelofi C, Randin O, Roppolo D, Luscher C, et al. (2002) Pheromone detection mediated by a V1r vomeronasal receptor. Nat Neurosci 5:1261–1262.

[96] Buck L, Axel R (1991) A novel multigene family may encode odorant receptors: a molecular basis for odor recognition. Cell 65:175–187.

[97] Wilt BA, Burns LD, Wei Ho ET, Ghosh KK, Mukamel EA, et al. (2009) Advances in light microscopy for neuroscience. Annu Rev Neurosci 32:435–506.

[98] Hsu FF, Nodari F, Kao LF, Fu X, Holekamp TF, et al. (2008) Structural characterization of sulfated steroids that activate mouse pheromone-sensing neurons. Biochemistry 47:14009–14019.

[99] Yu CR, Power J, Barnea G, O'Donnell S, Brown HE, et al. (2004) Spontaneous neural activity is required for the establishment and maintenance of the olfactory sensory map. Neuron 42:553–566.

[100] Arnson HA, Holy TE (2011) Chemosensory burst coding by mouse vomeronasal sensory neurons. J Neurophysiol 106:409–420.

[101] Luo M, Fee MS, Katz LC (2003) Encoding pheromonal signals in the accessory olfactory bulb of behaving mice. Science 299:1196–1201.

[102] Mao T, O'Connor DH, Scheuss V, Nakai J, Svoboda K (2008) Characterization and subcellular targeting of GCaMP-type genetically-encoded calcium indicators. PLoS ONE 3:e1796.

[103] Levai O, Feistel T, Breer H, Strotmann J (2006) Cells in the vomeronasal organ express odorant receptors but project to the accessory olfactory bulb. J Comp Neurol 498:476–490.

[104] Spehr M, Kelliher KR, Li XH, Boehm T, Leinders-Zufall T, et al. (2006) Essential role of the main olfactory system in social recognition of major histocompatibility complex peptide ligands. J Neurosci 26:1961–1970.

[105] Young JM, Massa HF, Hsu L, Trask BJ (2010) Extreme variability among mammalian V1R gene families. Genome Res 20:10–18.

[106] Rodriguez I, Del Punta K, Rothman A, Ishii T, Mombaerts P (2002) Multiple new and isolated families within the mouse superfamily of V1r vomeronasal receptors. Nat Neurosci 5:134–140.

[107] Tsuboi A, Yoshihara S, Yamazaki N, Kasai H, Asai-Tsuboi H, et al. (1999) Olfactory neurons expressing closely linked and homologous odorant receptor genes tend to project their axons to neighboring glomeruli on the olfactory bulb. J Neurosci 19:8409–8418.

[108] Roppolo D, Vollery S, Kan CD, Luscher C, Broillet MC, et al. (2007) Gene cluster lock after pheromone receptor gene choice. EMBO J 26:3423–3430.

[109] Isogai Y, Si S, Pont-Lezica L, Tan T, Kapoor V, et al. (2011) Molecular organization of vomeronasal chemoreception. Nature 478:241–245.

[110] Ishii T, Mombaerts P (2008) Expression of nonclassical class I major histocompatibility genes defines a tripartite organization of the mouse vomeronasal system. J Neurosci 28:2332–2341.

[111] Alekseyenko OV, Baum MJ, Cherry JA (2006) Sex and gonadal steroid modulation of pheromone receptor gene expression in the mouse vomeronasal organ. Neuroscience 140:1349–1357.

[112] Halem HA, Cherry JA, Baum MJ (1999) Vomeronasal neuroepithelium and forebrain Fos responses to male pheromones in male and female mice. J Neurobiol 39:249–263.

[113] Halem HA, Baum MJ, Cherry JA (2001) Sex difference and steroid modulation of pheromone-induced immediate early genes in the two zones of the mouse accessory olfactory system. J Neurosci 21:2474–2480.

[114] Meeks JP, Holy TE (2009) An ex vivo preparation of the intact mouse vomeronasal organ and accessory olfactory bulb. J Neurosci Methods 177:440–447.

[115] Mombaerts P (2006) Axonal wiring in the mouse olfactory system. Annu Rev Cell Dev Biol 22:713–737.